AN INVESTIGATION OF BULK NANOCRYSTALLINE COPPER FABRICATED VIA SEVERE PLASTIC DEFORMATION AND NANOPARTICLE CONSOLIDATION

A Dissertation

by

MOHAMMED HAOUAOUI

Submitted to the Office of Graduate Studies of
Texas A&M University
in partial fulfillment of the requirements for the degree of

DOCTOR OF PHILOSOPHY

December 2005

Major Subject: Mechanical Engineering

AN INVESTIGATION OF BULK NANOCRYSTALLINE COPPER FABRICATED VIA SEVERE PLASTIC DEFORMATION AND NANOPARTICLE CONSOLIDATION

A Dissertation

by

MOHAMMED HAOUAOUI

Submitted to the Office of Graduate Studies of
Texas A&M University
in partial fulfillment of the requirements for the degree of

DOCTOR OF PHILOSOPHY

Approved by:

Chair of Committee,	Ibrahim Karaman
Committee Members,	K. Ted Hartwig
	Richard Griffin
	Eyad Masad
Head of Department	Dennis L. O'Neal

December 2005

Major subject: Mechanical Engineering

ABSTRACT

An Investigation of Bulk Nanocrystalline Copper Fabricated via Severe Plastic Deformation and Nanoparticle Consolidation. (December 2005)

Mohammed Haouaoui, B.S., Ecole des Mines de Saint Etienne (France);

M.S., Texas A&M University

Chair of Advisory Committee: Dr. Ibrahim Karaman

Ultrafine grained (UFG) and nanocrystalline materials have attracted considerable interest because of their unique mechanical properties as compared with coarse grained conventional materials. The fabrication of relatively large amounts of these materials still remains a challenge, and a thorough understanding of the relationship between microstructure and mechanical properties is lacking. The objective of this study was to investigate the mechanical properties of UFG and nanocrystalline copper obtained respectively by a top down approach of severe plastic deformation of wrought copper and a bottom up approach of consolidation of copper nanoparticles using equal channel angular extrusion (ECAE). A critical assessment and correlation of the mechanical behavior of ECAE processed materials to the microstructure was established through the determination of the effect of strain level and strain path on the evolution of strength, ductility and yield anisotropy in UFG oxygen free high conductivity copper in correlation with grain size, grain morphology and texture.

ECAE was shown to be a viable method to fabricate relatively large nanocrystalline consolidates with excellent mechanical properties. Tensile strengths as high as 790 MPa and fracture strain of 7 % were achieved for consolidated 130nm copper

powder. The effects of extrusion route, number of passes and extrusion rate on consolidation performance were evaluated. The relatively large strain observed was attributed to the bimodal grain size distribution and accommodation by large grains. The formation of bimodal grain size distribution also explains the simultaneous increase in strength and ductility of ECAE processed wrought Cu with number of passes. Texture alone cannot explain the mechanical anisotropy in UFG wrought copper but we showed that grain morphology has a strong impact and competes with texture and grain refinement in controlling the resulting yield strength. Tension-compression asymmetry was observed in UFG wrought copper. This asymmetry is not always in favor of compression as reported in literature, and is also influenced by grain morphology through the interaction of dislocations with grain boundaries. Different prestrains in tension and compression should be experimented to have a better understanding of the encountered anisotropy in Bauschinger parameter in relation with the observed tension-compression asymmetry.

Dedicated

To my parents, Farida and Ahmed for their endless love.

To my wife, Chehrazade for her unconditional support.

To my children, Layan and Adam for the happiness they bring to my life.

ACKNOWLEDGEMENTS

My doctorate dissertation was a fundamental experience, not just for the amount of scientific knowledge I gained, but also for the many things I learned about myself and life in general. Many people have helped me through this long journey, and to them goes all my gratitude. It is too tough to acknowledge everyone who contributed in this challenging endeavor, nevertheless I will mention some here and I apologize to the many I have surely omitted.

First of all I would like to thank Dr. Karaman who provided me with every possible opportunity to advance my scientific understanding and career. I was driven and motivated during these four years by his exuberant enthusiasm and I will always feel proud that I have been a first PhD student of a very promising figure in the field. I thank Professor Maier for his very valuable contribution in this study through his rigorous TEM work and the fruitful discussion he affably benefited me with. For introducing me to the field of severe plastic deformation, and for serving as a member of my committee, I am indebted to Dr. Hartwig who influenced this work with his insightful observations. I also would like to thank my committee members Dr. Griffin and Dr. Masad for their effort in reviewing this work. I am also grateful to Mr. Barber for his technical support and much appreciated help in the processing of materials.

This work would not have been accomplished without the unconditional support of my family. To my parents, Farida and Ahmed, for all the sacrifices you endured to provide me with the best education and for your moral support and prayers. My wife Chehrazade, thank you for your unconditional support, for your patience and strong will

which inspired me throughout this study. I would like to also thank my mother in law Khadija for her priceless support in filling the arduous task of taking care of our children.

Finally, I would like to thank the students in Dr Karaman's research group Benat Kockar, Ersin Karaca, Guven Yapici, Burak Basaran, Yang Cao, Ajay Kulkarni, Anish Simon and Steve Sutter for creating a peaceful, and a motivational environment for a good completion of this study. I thank also Suveen Mathaudhu for his friendship and affable company.

This research was supported by a grant of National Science Foundation, contract CMS 01-34554, Solid Mechanics and Materials Engineering Program, Directorate of Engineering, Arlington.

TABLE OF CONTENTS

CHAPTER Page

Page

LIST OF FIGURES

Page

Page

Page

Page

Page

LIST OF TABLES

Page

CHAPTER I
INTRODUCTION

1.1. Motivation and significance

Materials with ultra-fine grains (UFG) and nanocrystals (NC), defined with a grain size below ~ 1μm and ~ 100 nm respectively, have attracted considerable interest because of their unique properties as compared with larger grained conventional materials. This interest is largely due to a promising combination of enhanced mechanical characteristics (yield strength and hardness with fairly large ductility), superior wear resistance, and the promise of enhanced superplastic-like behavior at relatively low temperatures and faster strain rates compared to their microcrystalline (MC) counterparts.

The application of ultra high strains which is accompanied by continuous grain refinement has motivated the development of new processes allowing the introduction of unlimited strains such us equal channel angular extrusion (ECAE), and high pressure torsion (HPT) [1-4]. Although many studies were performed on microstructural evolution in UFG materials, mostly TEM and characterization of grain misorientation distribution, the description of microstructure formation in ECAE processed Cu is not as clear and thorough as in rolled materials where Hansen and co-workers have produced an immense amount of information and enriched the current knowledge [5-9]. The effect of strain path on the resulting microstructures and its relation to mechanical properties has not been studied extensively and some conflicting results have been presented. A more systematic approach is needed to relate the multitude of ECAE routes, to the mechanical properties in consideration with the microstructure.

This dissertation follows the style of Acta Materialia.

To the best knowledge of the author, no systematic results have been reported to correlate the mechanical behavior of ECAE processed material to geometrical factors, such as the aspect ratio and the grain inclination angle, yielded by different ECAE routes and number of passes. However, it has been assumed [10] that the effect of strain path on tensile results is not significant despite the differences in their UFG microstructures. The literature is also lacking studies relating the UFG microstructures produced by severe plastic deformation to mechanical anisotropy. Therefore, anisotropy in ECAE processed Cu was investigated in this study through a series of tension and compression tests conducted on specimens cut along three perpendicular directions for different ECAE routes and number of passes. The yield strengths were compared and related to the morphological features of each case. Motivated by the same concern of interrelation between microstructure and mechanical properties, Bauschinger experiments were performed and related to different cases through the Bauschinger parameter defined subsequently.

In the other hand, the difficulty of fabricating bulk NC materials has been a major issue for the utility of these materials since Gleiter performed the first consolidation of nanopowders in 1981 [11]. Equal channel angular extrusion (ECAE) and high pressure torsion (HPT) of coarse grained materials and consolidation of micro powders [12-21], HPT consolidation of nanopowders [18], conventional area reduction extrusion [22-23], sintering of nanopowders produced either by evaporation-condensation techniques or mechanical alloying [24-28], crystallization from amorphous phases [29], and electrodeposition [2,30-32] are among the main processing methods available to obtain bulk NC materials.

Because NC materials fabricated by the previous methods involving consolidation or electrodeposition are produced in very small quantities, most of the mechanical characterization studies on NC materials have been limited in the past to indentation techniques [33], or to very few stress-strain tests which have been performed under compression [32]. More tensile results pertaining to NC materials are reported currently in the literature [34-36], but the most prominent results correspond to miniature or thin specimens rich in twins obtained by in situ consolidation of mechanically milled Cu powders at cryogenic temperatures [34-35] or electrodeposition [36]. These specimens yielded extraordinary strengths and strains at fracture (about σ_{UTS}=1100 MPa and ε_f 15% for both methods), but one should consider these results carefully as the small sizes of the tested gage area in tension specimens (2.5×1.5×0.5 mm^3 for [35] and 2×4×0.025 mm^3 for the electrodeposited foil [36]) reduces favorably any effect of possible processing flaw, and also the size effect is important in the case of miniature specimens. The scarcity of uniaxial stress-strain data of NC metals has hindered the development of a fundamental understanding of their mechanical behavior.

The need to develop an understanding of mechanical behavior of NC materials as a function of stress-state, strain level and length scales together with a thorough microstructural understanding has stimulated research in improving processing techniques for NC materials. The ECAE process was shown to be successful in achieving good consolidation of different microcrystalline (Al 6061, WC-Co) and amorphous materials (Cu and Zr based metallic glasses) [37-39]. The severe shear associated with ECAE (strain of 1.16 for a 90º extrusion) should enable consolidation of NC powders at temperatures lower than those required for HIP consolidation and hot compaction, and

thus should help to prevent unwanted grain growth. ECAE powder consolidation offers some benefits as compared to conventional extrusion powder consolidation since multiple passes are possible in ECAE without changing the cross-section which should lead to a better consolidation. ECAE also permits a variety of deformation configurations by changing the orientation of the billet with respect to the extrusion axis and shear plane after each pass. For details on the nomenclature used in ECAE processing, see [16,37-38,40-41].

The purpose of this study is the fabrication of bulk UFG and NC copper by severe plastic deformation of pure Cu and consolidation of Cu micro and nano particles, and the investigation of the resulting mechanical properties. We propose to use ECAE as a processing technique because it is a novel technique which permits the application of high uniform strains without considerable change in the shape of the processed material. This study will permit the investigation of the microstructure-property relationship in the bulk UFG and NC Cu by conducting optical microscopy, scanning and transmission electron microscopies, X-ray diffraction to track texture evolution, microhardness, tensile and compression experiments. It is important to study the different competing deformation mechanisms (i.e., dislocation slip, deformation twinning and grain boundary sliding) in these materials as there is ongoing controversy in the literature about the main deformation mechanisms intervening at the grain size range of UFG and NC materials as will be discussed later in Chapter II.

1.2. Objectives

The specific objectives of the present study are stated below:

1- Investigate the effect of strain path during ECAE processing on the mechanical properties of UFG Cu. More precisely, evaluate the evolution of strength and ductility in connection with the microstructural parameters and evolution formed during different processing schedules of ECAE.

2- Investigate the effect of strain path in relation with yield anisotropy in UFG Cu considering grain morphology and texture evolved in each route. The mechanical behavior through tension and compression experiments will be correlated with the size, morphology and spatial orientation of grains after each combination of route and the number of passes.

3- Experimentally examine the tension compression asymmetry in flow stress of UFG Cu and determine if the trend of the asymmetry is an inherent characteristic of UFG and NC materials and/or if it is affected by the processing history.

4- Experimentally explore the role of compressive prestrain on the deformation of UFG Cu under tensile loading through Bauschinger experiments and investigate the effect of strain path on the Bauschinger effect in ECAE processed bulk Cu.

5- Fabricate full density bulk NC materials using severe plastic deformation of bulk Cu and consolidation of micro and NC Cu powders.

6- Explore different methods to simultaneously enhance the ultimate tensile strength and strain at fracture of consolidated Cu powders, determine factors hindering a

good consolidation and propose solutions to improve the consolidation of Cu powders with the ECAE process.

7- Shed some light onto the governing deformation mechanisms of consolidated Cu powders through observed microstructural evolutions and variations in mechanical properties.

With these objectives, the outline of this dissertation is as follows:

Chapter II: A literature review of different processing methods involved in the formation of UFG and NC materials, mechanical properties, deformation mechanisms and a brief survey of ECAE related research.

Chapter III: The experimental methods and instruments used in this study.

Chapter IV: Investigation of the mechanical behavior of ECAE processed Cu through the study of the evolution of strength and ductility as a function of the deformation schedule, analysis of the yield anisotropy and its relation to the microstructural morphology, texture and the Bauschinger effect in ECAE processed Cu.

Chapter V: Examine different schemes for obtaining full density consolidate in nano and micro Cu powders using the ECAE process. Study the microstructural evolution and mechanical behavior of copper obtained by consolidation of micro and nano powders and relate these to different deformation mechanisms involved in NC materials.

Chapter VI: Main conclusions.

CHAPTER II
LITERATURE REVIEW

2.1. Properties and applications of pure copper

The choice of copper in this study is primarily motivated by its mechanical properties. Copper has very good ductility and is very suitable for research involving severe deformation. Furthermore, copper is selected because of the absence of phase transformation during annealing or processing. Extensive results are also available in literature for this material.

Copper is commonly used in pure form for its electrical or thermal properties. This metal possesses excellent characteristics for commercial applications because of reasonable cost. Chemistry is one of the most important variables that affects electrical conductivity. Solute elements significantly decrease electrical conductivity but their effect on conductivity can be decreased by formation of precipitates or oxides. The addition of solute can also retard the recrystallization temperature.

The oxygen content has an important role in improving the conductivity of copper by reacting with most of the impurities by forming insoluble oxides. However an excess of oxygen induces an adverse effect upon formability. Copper oxides can be either dissolved or precipitated from the matrix by altering the thermal history.

2.2. Equal Channel Angular Extrusion (ECAE)

Equal channel angular extrusion is a process which permits one to apply a large amount of strain without a reduction in work piece cross section. The process consists of

introducing a bar of metal through a channel of constant cross section that contains a sharp corner. The passage of the billet produces simple shear in the bar (Figure 2.1).

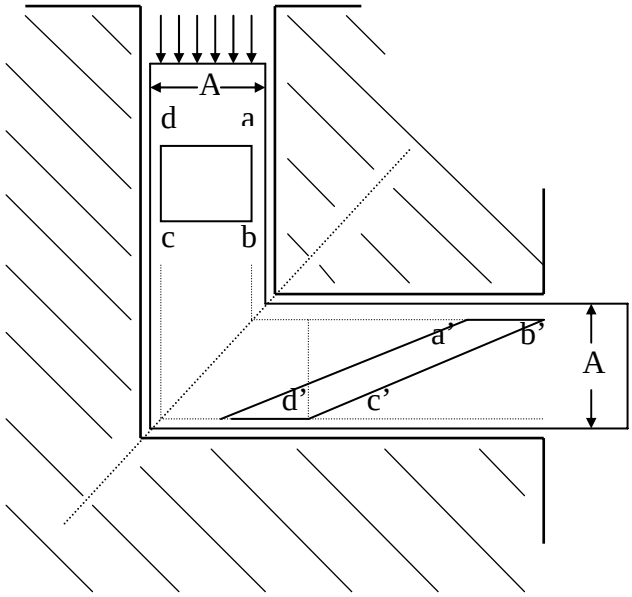

Figure 2.1 Schematic of the ECAE process. A square element is shown after its passage through the right angle of the die.

This process offers the possibility of inducing different types of microstructure by following different multipass routes. In route A extrusion, the billet orientation is kept the same for each pass. The billet is rotated +90° then -90° after each pass for route B and the rotation is 180° between passes for route C. Previous studies show that equal channel angular extrusion produces intense and uniform deformation throughout the billet, excluding end regions. Ferrasse et al [2] show that for route A and B, shear bands form in a first stage then are broken down to subgrains when the level of strain is increased. For route C, after each even number of passes, shear bands disappeared and more fine and equiaxed grains are formed. The same study shows that saturation of hardness and strength as well as grain refinement is reached after multiple passes when the strain

intensity reaches approximately $\varepsilon_I \sim 4$ to 5. The stability of the microstructure obtained after extrusion was emphasized by the work of Prangnell and Humphreys and their co-workers [42-43]. Humphreys exploits the high resolution of electron backscattering diffraction to quantify the level of high angle boundaries. He analyzed the sub-micron cellular deformation structure and determined the distribution of high and low angle boundaries as a function of the processing conditions. It was concluded that the severely deformed microstructures can not be simply described as “sub-micron grained”, the material can still contain proportions of low angle boundaries. Prangnell shows that the deformation structure is inhomogeneous and large stable grains can persist to high strains. The deformed state is very sensitive to the strain path used and redundant deformation appears to be an inefficient way to refine grains. An inhomogeneous distribution of high angle boundaries in the deformed condition can result in a bimodal grain size distribution during the early stages of annealing. The same work demonstrated the effects of starting grain size on the deformation structure at very high strains. It was shown that the final microstructure is the same for the two starting grain sizes, at strains greater than 6. This process of producing fine homogenous grains occurs for lower strains in the fine grained material.

Humphreys *et al* show that the main criterion for the formation of a sub-micron grain structure is the generation of high-angle grain boundaries during the deformation process. Factors which promote this condition are a small initial grain size, a large strain, and a deformation process with a complex deformation path that prevents formation of planar boundary arrays.

The affect of stacking fault energy on microstructural development in ECAE was investigated [44]. It was shown that the low stacking fault energy of copper and the consequent low rate of recovery lead to a very slow evolution of the microstructure during ECAE deformation. The microstructure obtained for copper is not fully homogeneous even after a total strain of ~10, but this microstrucrure has the merit to be stable up to 400 °K. It was concluded that low stacking fault energy leads to exceptionally stable fine grains through the use of ECAE.

The knowledge of the texture yielded by the ECAE process is important because of its effect of the mechanical properties and especially yield strength. ECAE produces texture, which can be described by simple shear [45-46]. The texture evolution can be simulated as a series of simple shear deformations using existing polycrystal plasticity codes. For Cu, It has been reported [46] that texture after multipass processing via route A is similar to a rolling texture. An intermediate rotation of ± 90° during processing (route B) is found to produce a partial fiber texture. Route C processing leads to the formation of a sheet texture which is not eliminated when a reversal strain is applied. These results are similar to those reported previously in the work of Gibbs [47] who shows a shear texture in ECAE processed bulk iron after a single extrusion. An even number of passes following route C results in a texture that shows characteristics of both shear and the original texture. The same study shows that conventional sheet and fiber textures can be developed using multipass ECAE processing: route A results in texture similar to that obtained after cold rolling iron [48] with {001} parallel to the rolling plane and <110> parallel to the rolling direction. On the other hand, iron processed via route B exhibits a fiber texture, with <110> aligned parallel to the wire axis or the extrusion axis

for ECAE processed material, similar to that seen in drawn bcc metals [49]. The texture intensities for ECAE processed bcc material via different routes were found to be significantly lower than those resulting from conventional processes [50]. That was attributed to lower deformation symmetry and rigid body rotations associated with simple shear deformation. Gibbs shows in the same study that a recrystallization heat treatment between extrusion passes for iron-3% silicon produces components of the cube texture, (001)[100]. A rotation of about 15° was observed in simple shear textures produced by ECAE compared to theoretically modeled simple shear textures. This rotation was explained by the same author by the radical path change which occurs with multiple extrusion passes while for simple shear conventional processes, this path remains constant.

On the other hand, the description of structure formation in ECAE processed Cu is not as clear and thorough as in rolled materials where Hansen and co-workers produced an immense number of investigations [5-9]. Also, the effect of strain path on the resulting microstructures and its relation with the mechanical properties was not studied extensively and some conflicting results are found. A more systematic approach is then needed to relate the multitude of ECAE routes, to the mechanical properties through the formed microstructure.

Besides the refinement of the microstructure, the strength of ECAE process resides in its versatility and its ability to reproduce by changing the strain path, different microstructures and textures yielded by numerous conventional processing methods such as rolling and drawing. Therefore, by analogy, the established knowledge of microstructure formation during rolling can be used in ECAE. As a representative of fcc

materials with medium stacking fault energy, copper was extensively studied to better understand the interrelation between deformation conditions and microstructural evolution [5-9]. It is well known that medium to high SFE metals experience grain subdivision during plastic deformation. In these metals, the three dimensional mobility of dislocations due to cross slip contributes in the formation of the final microstructure: for low to medium strains, a cell block structure extended along slip planes is formed in cold rolled materials. This structure evolves towards a macroscopic direction almost parallel to the rolling direction for larger strains for which grain misorientation angles increase and cause grain subdivision. Grain morphology can be significantly altered when the strain path is changed, for example, from a lamellar structure to a more equiaxed structure when the material is cross-rolled [6]. The macroscopic subdivision of the grain is directly related then to the applied stress [7-9]. Similarly, ECAE process yields a lamellar microstructure when the orientation of the billet is not changed after each pass. It was also found that the development of hybrid routes involving orthogonal deformation paths contribute in obtaining smaller grains and more equiaxed microstructure as more slip systems are thought to accommodate the deformation and a continuous rearrangement of subgrain boundaries occurs by increasing the misorientation angles[51-52].

A combination of high strength and ductility was observed in UFG materials processed by severe plastic deformation. While the increase in strength can be explained by the reduction in the average grain size, the simultaneous increase of ductility was attributed to the coexistence of fine and coarse grain sizes, where the upper limit of this distribution provides the possibility of additional hardening. Dynamic recovery due to the stored strain energy when the material is subjected to additional passes creates this

bimodal distribution [53]. Furthermore, a certain tension/compression (T/C) asymmetry was noticed in UFG materials. Carsley et al [54] who were the first to report this asymmetry in UFG Fe, noticed a 30% difference in compressive and tensile yield strengths. The T/C asymmetry was explained by the effect of hydrostatic pressure on yield strength. Similar to glasses, Carsley et al explained the asymmetry by the pressure sensitivity of the yield criterion. A pressure-modified yield criterion accounted for both the asymmetry and shear bands observed in deformed UFG Fe specimens. Hayes et al [55] observed the same asymmetry in cryomilled Al alloy in the range of hundreds of nanometers. They considered the T/C asymmetry as an intrinsic property of the NC and UFG regimes as it was not observed when the final microstructure ranges from 500nm to about 1-2 μm [55]. Tabashnikova et al [56] reported a similar effect in nanostructured Ti (100-300 nm grin size) processed via ECAE. In a recent study Cheng et al [57] developed a model for the pressure dependence of the yield criterion in UFG materials based on the bow out mechanism of dislocations from grain boundary sources. The hydrostatic pressure dependency of the yield strength was accounted for by considering the pressure dependence of the dislocation self energy. This simple model correctly captures the experimental and asymmetry observations. However, the present study will show that the T/C asymmetry is not always in favor of compression and that it is affected by the ECAE route and the direction of testing.

2.3. Processing of UFG and NC materials

Different processing methods are used for the fabrication of UFG and NC materials. Equal channel angular extrusion (ECAE) and high pressure torsion (HPT) of

coarse grained materials and consolidation of micro powders (Figure 2.2) [12-21], HPT consolidation of nanopowders [18], conventional area reduction extrusion [22,23], sintering of nanopowders produced either by evaporation-condensation techniques or mechanical alloying [24-28], crystallization from amorphous phases [29], and electrodeposition [12,30-32] are among the main processing methods available to obtain bulk NC materials.

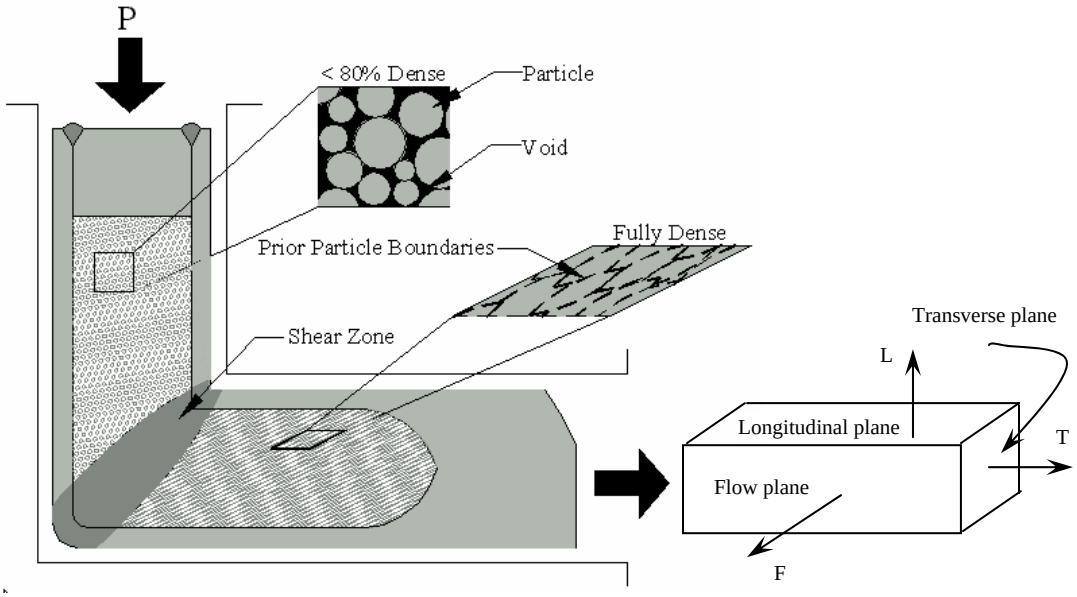

Figure 2.2 Schematic of the ECAE powder consolidation process.

Each processing method of NC materials has its own advantages and disadvantages. Table 2.1 summarizes these different processing methods. For instance, it is difficult to obtain grain sizes less than about 100 nm using ECAE when starting from bulk coarse grained materials. Moreover, the microstructure at the front and back ends of an ECAE billet is usually not uniform, the size of these regions can be as large as the

billet diameter depending on the processing route. The sample sizes that can be obtained by HPT and consolidation of nanopowders fabricated using evaporation and condensation techniques are very small. Contamination and residual porosity are the main problems in consolidation of mechanically alloyed nanopowders. Bulk amorphous materials are still difficult to make, and thus, crystallization of amorphous metals may not be the eventual solution for fabricating bulk NC materials. Moreover, chemical gradients and heterogeneous crystallization of intermetallic phases are other disadvantages present in fabricating bulk samples by crystallization of amorphous metals.

Table 2.1 Processing methods for the fabrication of UFG and NC materials.

Processing	Advantages	Disadvantages
Cryomilling	- Produce ultrafine grained materials in reasonable quantities. - Thermal stability due to the presence of fine oxides and nitrides from the milling process.	- Difficult to control the material purity. - Difficult to achieve full density.
Severe plastic deformation	- Material purity is the same as the starting material. - Cheap. - Full density in the case of SPD of bulk materials.	- Grain sizes of SPD bulk materials remain in the 150-300nm range. - Limited ductility of the initial material.
Gas phase condenstion	- Grain size in the 5-50 nm regime. - Texture free microstructure.	- Limited specimen volume. - Purity issues in the vicinity of particle boundaries. - Difficulties to retain fine grain size (grain growth). - Small bulk
Electrodeposition	- Grain size can be controlled and is in the range of 20-40nm. - Narrow grain size distribution.	- Produce thin sheets (~2mm). - Hydrogen, carbon, and sulfur levels in the deposits can be substantial. - Possible strong texture. - Small bulk

Finally, samples produced via electrodeposition are often contaminated by hydrogen, carbon and sulfur. The resulting columnar grain structure and possible strong texture developed may influence the resulting properties and create significant differences in mechanical behavior as compared to materials fabricated using other techniques. Clearly, comparison between the various nanomaterials fabricated using different processing routes is not straight forward, since there can be significant differences in local microstructural homogeneity, chemistry, impurities, porosity, and sample size between the various materials. It is unfortunate that today there is not a complete set of property variation data over a wide range of grain sizes on any material that is manufactured by the same processing method.

2.4. Mechanical properties and deformation mechanisms of UFG and NC materials

In the beginning, a brief and non critical presentation of the relationship between grain size and flow stress is addressed and different deformation mechanisms are suggested. For many MC and UFG metals and alloys with a grain size of 100 nm or larger, the strengthening accompanying grain refinement has been usually rationalized by the so called Hall[58]-Petch[59] mechanism. This relation relating the grain size d to flow stress σ has been under continuous investigation. Most of the research was motivated by attaining high strength when the grain size approaches the nanometer size. The Hall- Petch relationship is expressed as follows:

$$\sigma = \sigma_i + K_{H-P} d^{-1/2}$$

where σ_i is the lattice friction stress and K_{H-P} the so called H-P constant. The H-P relation is observed up to approximately 100 nm grain size (Figure 2.3). Grain size

hardening occurring in this regime of grain size was physically rationalized by the pile-up of dislocations at a grain boundary (Figure 2.4.a), giving a stress concentration which activates dislocation generation and/or motion in the adjacent grain from the so called Frank Read dislocation source (Figure 2.4.b). With further grain refinement down to 100 nm, the increasing flow stress departs markedly from its original slope causing a reduced increase rate of flow stress. In this regime of grain size, other mechanisms are suspected to operate as the grain size is reduced to the point that Frank Read sources cease to operate.

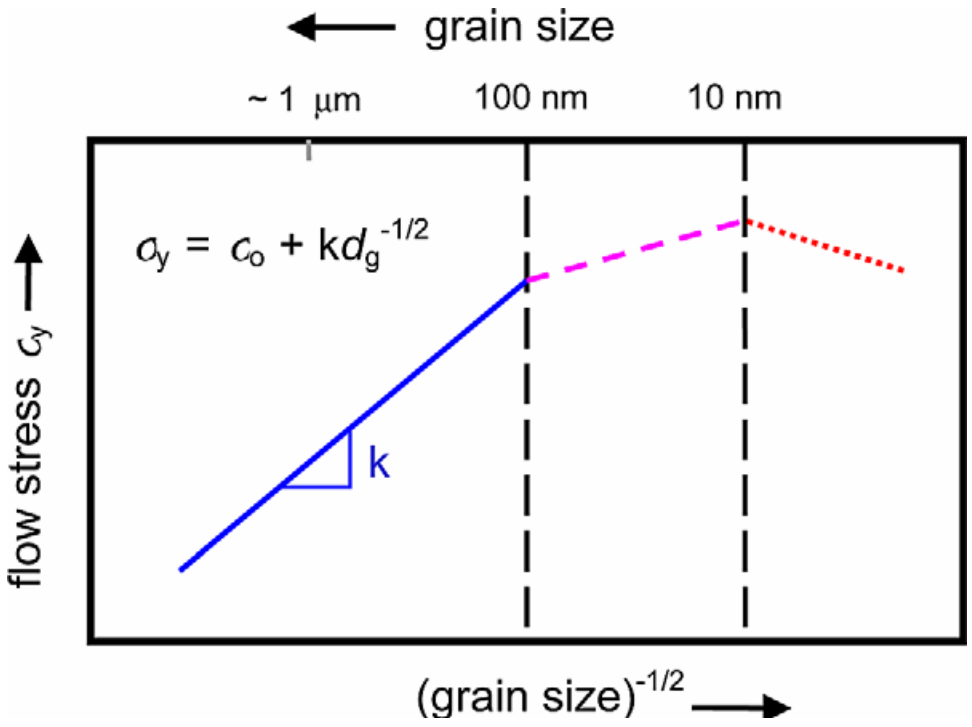

Figure 2.3 Schematic of the variation of flow stress as a function of grain size in MC, UFG, and NC metals and alloys [60].

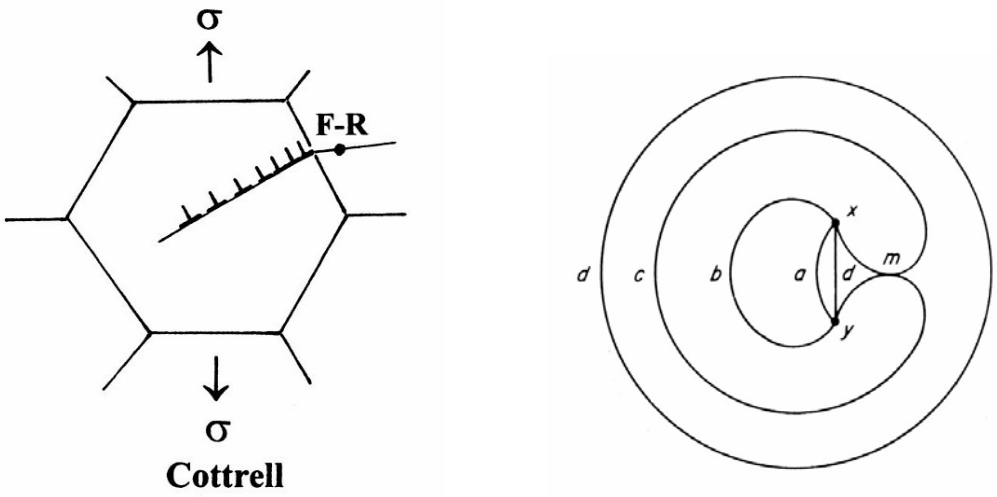

(a) (b)

Figure 2.4 (a) Pile-up of dislocations at grain boundary and (b) Frank Read dislocations source.

In this regime, any dislocation activity is believed to originate and terminate at grain boundaries. The grain boundaries are acting simultaneously as source and sinks for dislocations. Other mechanisms are thought to start contributing in the deformation. Because of the increase in grain boundaries density, coble creep and grain rotation are advanced as possible mechanisms to accommodate deformation. Coble creep (Figure 2.5.a) is a grain boundary diffusion mechanism taking place during the deformation of MC metals at high temperatures. The flow of atoms is initiated from grain boundaries subject to compressive stress to those under a tensile stress and occurs along the grain boundaries. Twinning was also observed in electrodeposited NC Ni [31] (Figure 2.5.b), and was suggested as an alternate deformation mode at this range of grain size.

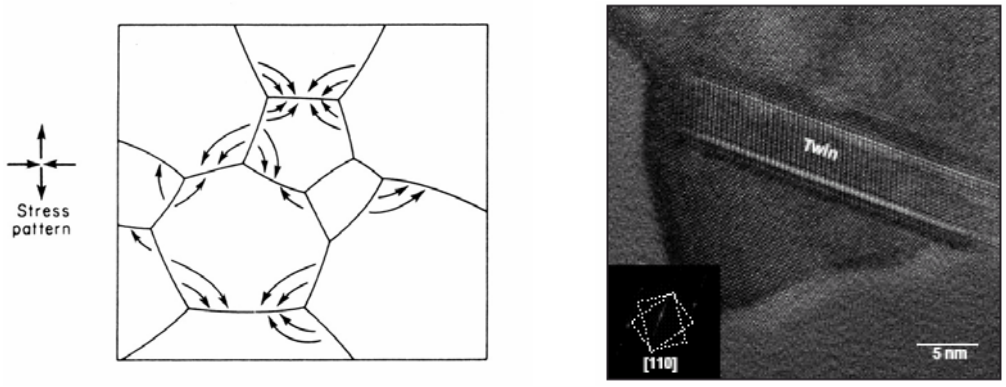

(a) (b)

Figure 2.5 (a) Coble creep and (b) twinning believed to accommodate deformation for grain sizes lower than 100 nm.

With further grain refinement, the flow stress reaches a maximum for a certain grain size in the range of 10-50 nm depending on the material. Further decrease in the grain size can cause weakening of the metal. The decrease of flow stress is attributed to the approach to the amorphous state because of the increase of grain boundary density and/or the activation of plastic instability in triple points which lead eventually to fracture. This decrease is also considered to be caused by the introduction of processing defects in NC materials.

Despite the extensive work on synthesis of NC materials, there are few reported data on room temperature monotonic stress-strain response of bulk NC materials [14-17,22-27,30,32,61-64] mostly because of the difficulty of obtaining large enough specimens with full density. Compression experiments conducted by Youngdahl *et al* [64] showed a strong correlation between the strength and the porosity content in compacted NC Cu and Pd. The use of miniature specimens for mechanical testing [65] demonstrated that specimens with very few processing flaws have very high yield

strength levels and reasonable ductility as compared to large specimens, indicating the importance of processing flaws on resulting properties. The same study [65] suggested that the grain boundary sliding mechanism does not contribute significantly to the room temperature deformation of 25-50 nm grain size Cu. It has also been reported [24] that deformation mechanisms in NC copper (25-55 nm grain size) are dominated by dislocation activity because work hardening was observed during compression. The dominance of dislocation activity over grain boundary moderated mechanisms during deformation has been clearly illustrated by a recent excellent review and in-situ TEM experiments by Kumar *et al.* [31] in Ni down to grain sizes of 20-30 nm. Moreover, an in-situ tensile experiment of NC copper specimens (grain size 20 – 500 nm) produced by inert gas condensation [66] confirmed the presence of parallel dislocation arrays in larger grains (~100 nm) and that deformation is governed by dislocation activity down to a grain size of 30 nm. On the other hand, molecular dynamic simulations of NC Cu showed that large plastic deformation can be accommodated by grain boundary sliding in samples with grain sizes less than 20 nm [67-68], but no experimental data has yet been obtained to confirm this theory. In summary, the above discussion shows the necessity of a systematic and thorough study to clarify some of the controversies related to the deformation mechanisms and microstructural evolution in NC materials.

Earlier works on deformation mechanisms in NC materials [12,14-18,69-70] argued that dislocation and grain boundary mechanisms such as grain boundary sliding and Coble creep can simultaneously interplay or the latter is the governing mechanism below a certain grain size, such as 70 nm in Cu. However, more recently, convincing experimental evidence [26,31,71] demonstrated that down to about 20 nm grain size,

dislocations are still operative. Although some studies [12,15-16] have attributed certain findings such as high strain rate sensitivity to grain boundary sliding, it appears that there is not any direct experimental evidence showing grain boundary moderated mechanisms in NC materials.

In the present study, Cu powders with different initial sizes (325 mesh (powders sieved through a 45 μm sieve), 130 nm and 100 nm) were consolidated using equal channel angular extrusion (ECAE) (Figure 2.2). ECAE is a severe plastic deformation technique in which load is applied from the top of the vertical channel and the billet is deformed in the shear zone and extruded from the horizontal channel as shown in Figure 2.2. ECAE was chosen as it offers several advantages over the competing processes: in comparison with conventional bulk extrusion, the same amount of equivalent strain can be achieved with lower extrusion loads in ECAE using a novel tool design incorporating moving die walls [72-74], the formation of uniform microstructures, likelihood of reduced production cost and control over the development of grain morphology [75]. Moreover, ECAE offers some control of texture as shown in recent studies on pure tantalum, iron and copper with initial coarse grain sizes [46-47,76].

CHAPTER III

EXPERIMENTAL PROCEDURES

3.1. Materials

The present investigation was conducted using Copper 101 provided by Hitachi Cable, Ltd. The chemical analysis as reported by Hitachi Cable, Ltd, is shown in Table 3.1. The materials were received as extruded rods.

Table 3.1 Chemical content of the CDA 101 copper used in the present investigation (in ppm by weight)

Elements	Measured Value
Cu	99.99
Pb	1
Zn	0.3
Bi	0.2
Cd	0.2
O	2
P	2
S	8
Se	2
Te	0.5
Sb	1
As	1
Fe	4
Mn	0.3
Ni	1
Ag	1
Sn	1

High purity copper powders with three different sizes (325 mesh, 100 and 130 nm) were used in this study. DOE Ames Laboratory provided 325 mesh Cu powder. The 100 and 130 nm Cu powders were acquired from Argonide Corporation, Sanford, Florida and were fabricated using the electro-explosion of wire process (EEW). In this

process, wire is fed into an argon-filled reactor, and it is subjected to a high-current, high-voltage microsecond pulse to cause it to explode. The oxygen content was estimated to be less than 0.6% in weight in NC particles by the manufacturer using the method of pulse reduction melting in helium gas.

3.2. ECAE procedures

3.2.1 Extrusion of Cu billets

The ECAE billets were prepared from one inch square extruded (Cu 101) rod. After cutting, 12 billets possessing square cross-sections with the nominal dimensions of 1"×1"×6" were ready to be extruded. Table 3.2 shows the different parameters of the ECAE deformation. Prior to extrusion, the extrusion tool components and billets were lubricated in order to minimize friction during extrusion. The copper billets were easily extruded at room temperature, because of the excellent ductility of Cu 101 using one-inch tooling [72] with a punch speed of 5mm/sec.

Table 3.2 Conditions of ECAE extrusion

Lubricant	Anti-seize lubricant (Pergamex Co.)
Ram Speed V	5 mm/sec
Extrusion Temperature	Room temperature (23 ± 2° C)

The extrusion operation caused flashing along the edges of the billet. The flash was removed using a band saw. The heat induced during cutting was reduced by a steady flow of water over the specimen. Care was taken to keep the specimen cool

during cutting because the microstructure of the specimen can be drastically changed if the temperature is raised due to the relatively low temperature of recrystallization of copper (around 160°C). Rolling and machining were done when needed after each extrusion pass were done to enable the billet to fit into the die.

The ECAE processing schedule is summarized in Table 3.3. The effects of one, two, four, eight and sixteen passes and five different routes were investigated in this study. Figure 3.1 [77] illustrates the reorientation of the billet after each pass for different routes. In route A, the billet orientation is kept the same for each extrusion pass. The billet is rotated plus and minus 90° between successive passes with respect to the extrusion direction for route B. 180° rotation is applied in route C and 90° rotation in route C' (also known as Bc) in the same direction after each pass. Route E is a hybrid route similar to 2C*2C where the cross refers to an intermediate 90° rotation of the billet with respect to the extrusion direction. This variety of ECAE schedules permits to control the desired microstructure by yielding different microstructures (grain morphology, grain size and texture). Table 3.3 summarizes the expected microstructures and the analogy to the conventional deformation processes of different ECAE schedules. The temperature rise in the billet due to the deformation heat was measured to be about 50°C.

Table 3.3 Schedule of ECAE processing

ECAE route		A	B	C	C'	E
Number of passes		1, 2, 4, 8	2, 4	2, 4	4	4, 8, 16
Rotation before	Odd passes	0º	+90º	+180º	+90º	+180º
	Even passes	0º	-90º	+180º	+90º	+90º
Microstructures		Lamellar	Filamentary	Equiaxed	Equiaxed	Equiaxed
Deformation analogy		Rolling	Drawing	Shear	Shear	Shear

3.2.2 Consolidation of Cu powders

The consolidation of Cu powders can be divided into three different major stages depending on the nature of Cu powders and filling procedure: manual tapping, hand pressing or prior cold isostatic pressing (CIP) of the powders before filling the can. Figure 3.2 shows the processing methodology detailing the major steps involved in the preparation and investigation of Cu powders.

First pass (N=1) Second pass (N=2)

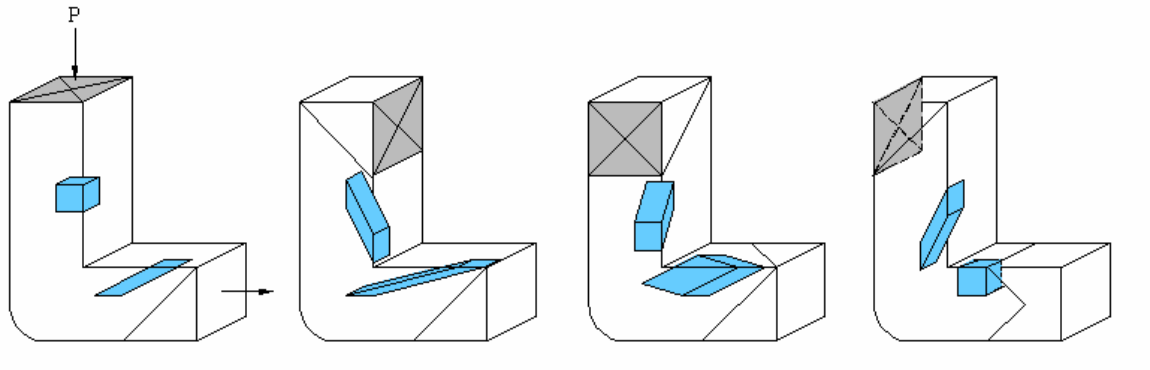

(a) (b) (c) (d)

Figure 3.1 Shape of the initial cubic element after (a) the first pass, (b) 2A, (c) 2B and 2C', and (d) 2C and 2E [77].

For stage 1 where filling was accomplished by manual tapping, 25 mm square 1018 steel, nickel and copper cans with a 20 mm diameter cross section inner chamber (Figure 3.3) were filled with these powders as summarized in Table 3.4. The filling was conducted in an open environment for the 100 nm Cu powder which was loaded into nickel or steel cans. For other particle sizes, the powders were degassed in vacuum for 8 hours prior to the filling. The 325 mesh powder was degassed at 150 °C and 130 nm powder was degassed at room temperature. Copper cans were used for the 325 mesh Cu

powder because of its lower flow strength. Nickel cans were used for the consolidation of 130 nm powder for which the schedule was decided after the extrusion runs with the 100 nm Cu powder to eliminate routes yielding poor consolidation. As a rule of thumb, the flow strength of the can material should be comparable to the flow strength of powder consolidates. The cans were electron beam welded in vacuum after filling and processed with different ECAE routes under an extrusion speed of 2.5 mm/sec.

Table 3.4 summarizes the experimental conditions for each can. Routes A was not processed beyond two passes because the length of consolidate diameter with uniform deformation that can be obtained with this route is limited as compared to the ones obtained with Routes B, C and E. The reason for this can be better understood if the consolidate geometry after successive shearing on the same plane is considered (Figure 3.4).

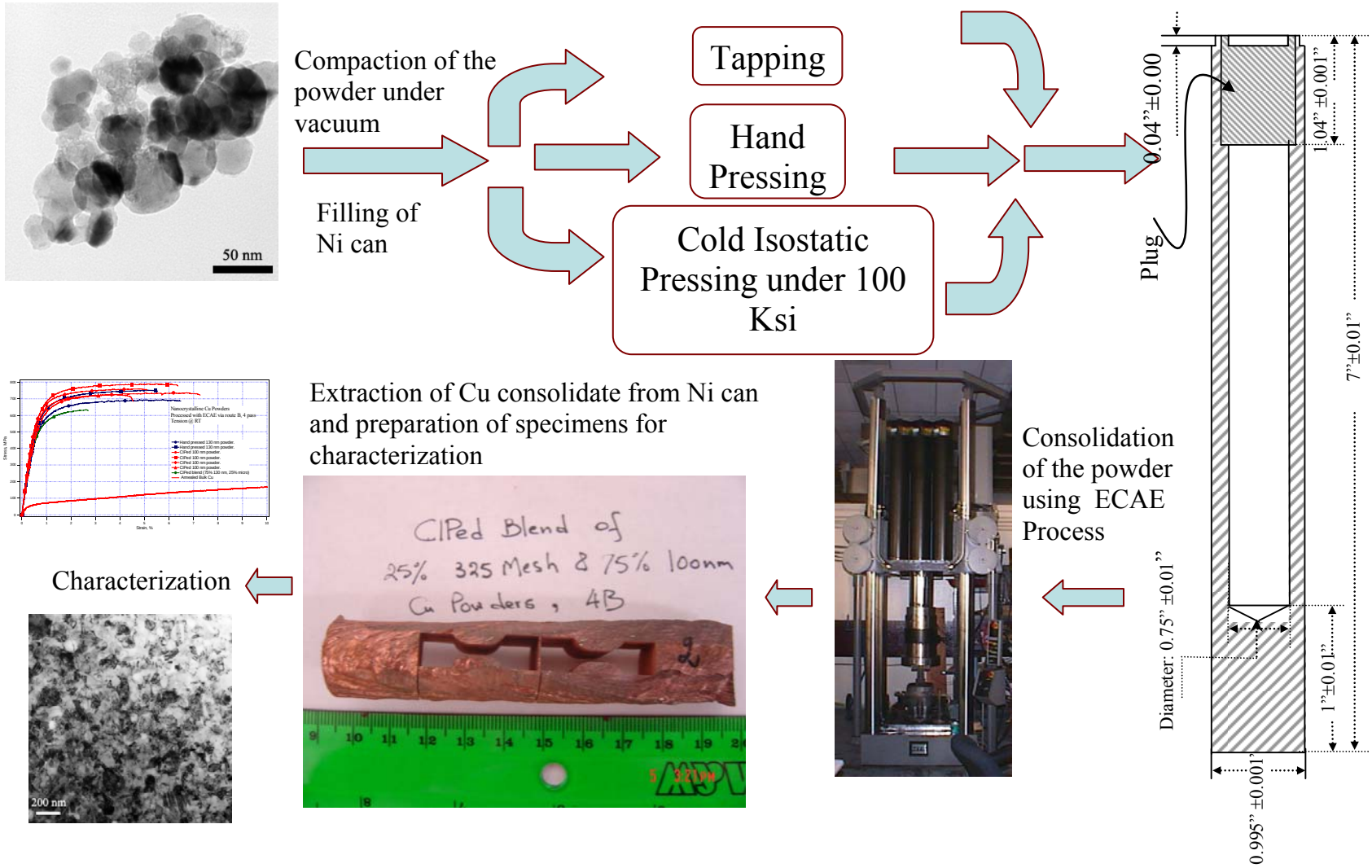

Figure 3.2 The processing methodology detailing the major steps involved in the preparation and investigation of Cu nanoparticles.

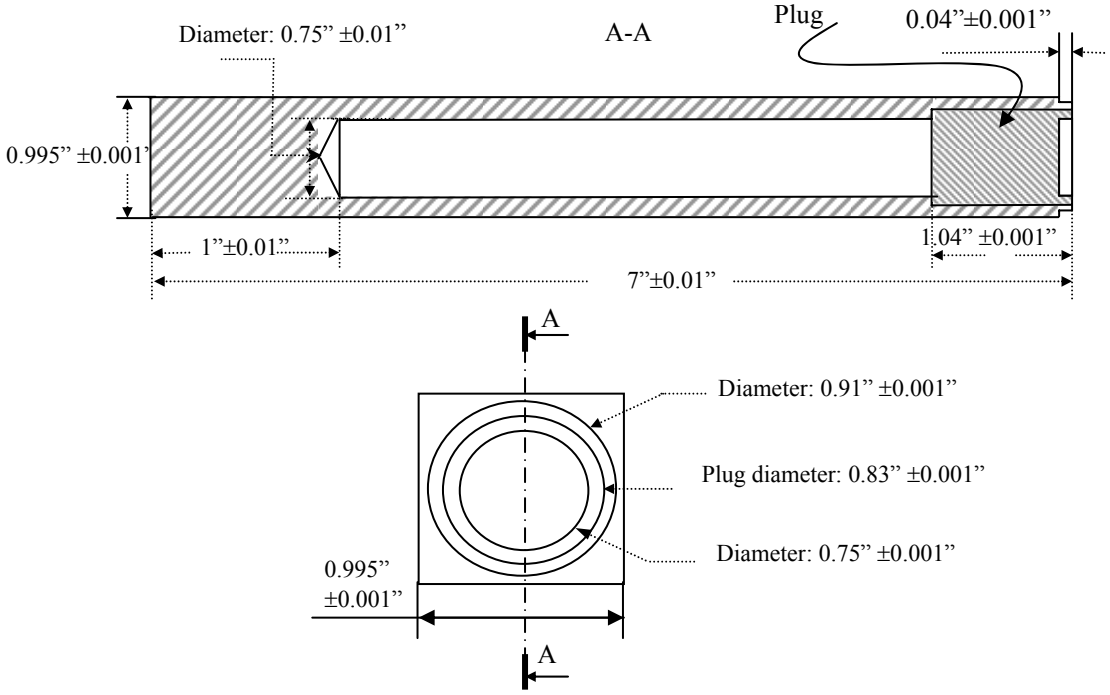

Figure 3.3 Schematic of cans used for the consolidation of Cu powders.

A hand press was used to fill the cans in stage 2 of the study in order to assure a better compaction of the powder prior to extrusion and a higher yield of material after consolidation. The hand pressing was achieved in a glove box in an argon environment followed by an operation of baking of the can before sealing to guarantee the evaporation of eventual entrapped moisture in the powder. The baking temperature was 130°C for 3h for nanocrystalline Cu powders and 150°C for 325 Mesh Cu powder.

Table 3.4 Summary of the experimental conditions used for the consolidation of micron and nanometer size copper particles. E, F and S are extrusion, flow, and shear directions as shown in Figures 2.2 and 3.7.

Stage	Case #	Route	Can specifications (material/length of powder space)	Filling environment	Powder Size	Mechanical testing
Stage 1: Manual tapping	1	1A	Nickel/ 5cm	Air	100nm	No testing was done
	2	2C	Nickel/ 5cm	Air		
	3	1A	Steel 1018/ 10cm	Air		
	4	2A	Steel 1018/ 10cm	Air		
	5	2C	Steel 1018/ 10cm	Air		
	6	1A	Steel 1018/ 10cm	Air		
	7	2A	Nickel/ 10cm	Air		
	8	2C	Nickel/10cm	Air		
	9	1A	Copper/ 7.6cm	vacuum	-325 mesh	Hardness, Tension (E) Compression(F)
	10	2A	Copper/ 7.6cm	vacuum		
	11	2B	Copper/ 7.6cm	vacuum		
	12	2C	Copper/ 7.6cm	vacuum		
	13	4C	Copper/ 7.6cm	vacuum		
	14	2B	Nickel/ 7.6cm	vacuum	130 nm	T(E) & C(E)
	15	2C	Nickel/ 7.6cm	vacuum		No test
	16	4E	Nickel/ 7.6cm	vacuum		T(E) & C(E)
	17	6E	Nickel/10cm	vacuum		Tension (E)
	18	4C’	Nickel/10cm	vacuum		Tension (E)
Stage 2: Hand pressing	19	2B	Nickel/10cm	Vac+130C,3h	50nm	No testing
	20	4B	Nickel/10cm	Vac+130C,3h		
	21	4C’	Nickel/10cm	Vac+130C,3h		
	22	2A	Nickel/10cm	Vac+130C,3h	150nm	No testing
	23	2B	Nickel/10cm	Vac+130C,3h		Tension (E)
	24	4B	Nickel/10cm	Vac+130C,3h		Tension (E)
	25	4C’	Nickel/10cm	Vac+130C,3h		Tension (E)
	26	4B	Nickel/10cm	Vac+150C,3h	-325 mesh	Tension (E)
	27	4C’	Nickel/13cm	Vac+150C,3h		Tension (E)
	28	4C’	Nickel/13cm	Air		Tension (E)
Stage 3: Cold Isostatic Pressing	29	4B	Nickel/13cm	Vac+130C,3h	100nm	Tension (S)
	30	4B	Nickel/13cm	Vac+130C,3h	75% of 100nm & 25% of -325 mesh	Tension (S)

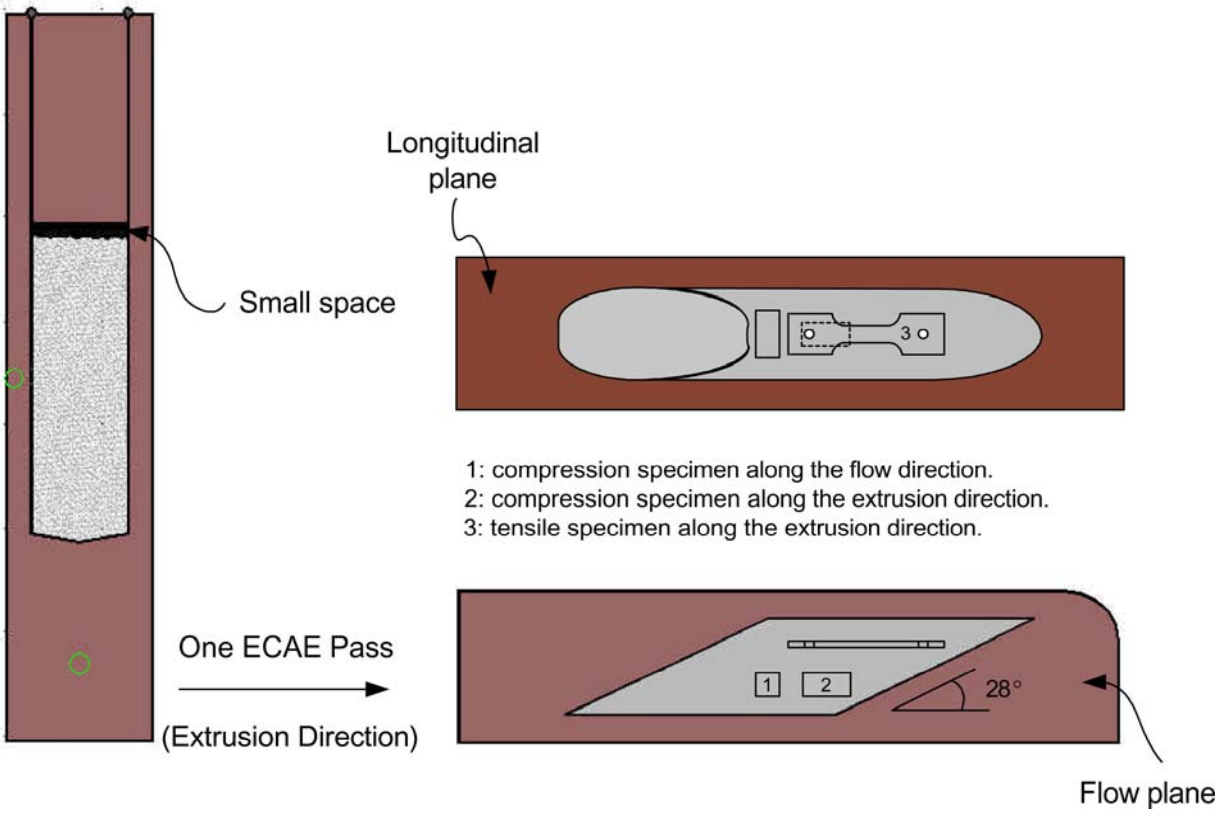

Figure 3.4 Schematic of the can, consolidated powder after 1A extrusion and the location of the tension and compression samples that were cut from the powder consolidate. The numbers 1 and 2 in the schematic demonstrate compression samples with different loading axes.

This difference in baking temperature was deliberately imposed to circumvent any possible grain growth in nanocrystalline powders. The cans were eventually electron beam welded under vacuum. The use of a hand press created compact layers at each step of manual compaction with well defined boundaries where shear can occur preferentially during extrusion leading to a non uniform consolidation. This problem motivated the use of high hydrostatic pressures through cold isostatic pressing (CIP) to assure not only a uniform compaction of the powder but also a better initial break down of the agglomerates (This point will be elaborated in more details in chapter V).

3.3. Microstructure analysis

3.3.1. Metallography and optical microscopy

The issue which prompted optical microscopy investigation is to determine the evolution and disintegration of Cu powder agglomerates for different ECAE routes as it was revealed (Chapter V) using Scanning Electron Microscopy (SEM) that Cu powders at the nanoscale tend to cluster together to form micron size agglomerates. To reveal the consolidate microstructure, the specimens were prepared using sectioning, mounting, polishing, and etching as described below.

Specimen cutting from the billet is an important step which was conducted carefully. A successful sectioning will not affect the surface properties for a succeeding hardness measurement or metallographic examination. A deficient sectioning will introduce a consequent mechanical hardening of the surface or will heat the surface causing annealing. The hardening of the surface will be difficult to remove with grinding and polishing. Another factor which was taken into account is the orientation of the samples and straight cutting. A traditional cutting, even carefully conducted, will cause an inclination of the specimen with respect to the desired orientation. This factor is critical when the specimen is used for texture measurements. Thus, the samples for microscopy and microhardness were cut with an Isomet 1000 diamond saw using an oil-water lubricant. The cooling enabled cutting without a significant rise in temperature and thus no heating.

To ensure an accurate orientation for metallographic and texture examination of the selected planes, all billets and consolidates were cut via wire electrodischarge machining (EDM). For optical microscopy observations, specimens were mounted in

epoxy. Mounting in bakelite was avoided because the necessary heat (250°C) to set this thermoset polymer will alter the microstructure of heavily worked copper. The mounting in epoxy can be considered safe even if the temperature rise during curing reaches 150°C. The curing time at 150°C was recorded to be 15 min. The investigation of the specimens extruded at room temperature revealed that the microstructure of heavily worked material was not altered appreciably by the epoxy heating.

Specimens were sucessively hand-ground with silicon carbide papers of 320, 600, 800 and 1200 Grit. Each grinding sequence was performed until uniform grinding lines were obtained (2 to 3 minutes). The task of grinding is most effective when the direction of grinding is rotated 90° between each grit-size. Because of the softness of copper, a moderate pressure was applied on a specimen while being ground to avoid the creation of deep scratches which are then difficult to remove. The specimens were rinsed after each grinding step to avoid any cross contamination with abrasive particles, which would reduce the efficiency of grinding.

All specimens were also mechanically polished using 3μm and 1μm diamond paste on a billard cloth for 3 min at each step. The resulting surface was often sufficient for optical investigations, but the addition of a final polishing step using colloidal silica (mix 1 part of colloidal silica with 5-6 parts of distilled water) improved the results in some cases.

Cleanliness is also an important requirement during polishing. It is necessary to clean the specimen with distilled water several times within one operation sequence. Ultrasonic cleaning can be useful if persistent dirt residues are released from fine cracks which form between the specimen and epoxy. To dry the specimen, it is more effective

to rinse the specimen with alcohol because it dries quickly and does not stain when using a hot air dryer.

Prior to etching, the final polished specimen surface was examined under a microscope to distinguish features such as pits, pores, inclusions and so forth. Such features may be caused by grinding and polishing and should be spotted before etching.

The final polished copper surface will not exhibit the microstructure because the incident light is uniformly reflected. To produce image contrast between grains or to reveal grain boundaries by local attack, chemical etching is used. The chosen etchant for this research reveals grains by differential surface etching. The method is effective because different grain orientations are attacked at different rates and develop different surface finishes. Etching was accomplished by swabbing for 20 to 40 seconds at room temperature with a solution composed of:

- 10 g of ammonium persulfate.
- 100 ml of distilled water.

3.3.2. Scanning electron microscopy (SEM)

A scanning electron microscope, JEOL JSM-6400, was used to examine the fracture surfaces of tensile specimens of ECAE processed bulk Cu to relate the fracture features to the microstructure and mechanical properties especially the ductility. SEM was also used to study the nature of fracture in consolidated Cu powders. Cu powders morphology and size were determined using SEM.

To observe the grain size and morphology, back scattered electron (BSE) micrographs were captured using a high resolution Zeiss 1530VP FESEM at a voltage

of 15 kV. The BSE investigation was preferred to optical microscopy for ECAE processed bulk Cu because pure copper is heavily deformed and the morphology of grains cannot be distinguished easily with optical microscopy. The specimens were ground and polished to 1μm finish and then final polished using a diluted solution of colloidal silica and hydrogen peroxide in the final polishing step. BSE was also used to investigate eventual presence of remnant porosity in consolidated Cu powders.

3.3.3. Transmission electron microscopy (TEM)

TEM is important in determining the microstructural features in ultrafine grained materials produced by severe plastic deformation. The developed features in as processed material are hardly resolvable with optical microscopy and it is necessary to use TEM to observe the dislocation substructures after ECAE processing. For TEM analysis, specimens were prepared by mechanical grinding and twin jet electropolishing. Relatively large electron transparent areas were obtained with a solution consisting of 250 ml phosphoric acid, 500 ml distilled water, 250 ml ethanol, 50 ml propanol and 5 g urea at a temperature of –16 °C and a voltage of 15 V. The resulting thin foils were examined in a PHILIPS CM 200 electron microscope operated at 200 kV. TEM was also used to investigate the shape of the nanocrystalline powder agglomerates. PHILIPS is a trademark of Philips Electronic Instruments Corp., Mahwah, NJ.

3.3.4. Texture analysis

For texture measurements, the samples were mounted in epoxy and polished. Mainly the flow plane was investigated because it makes it possible to use symmetry options by the software used, i.e. “preferred orientation package- Los Alamos”

(POPLA) [78]. Pole figures on the two other longitudinal and transverse planes can be achieved by rotating and/or tilting the flow plane texture using POPLA software.

The pole figures are based on X-ray diffraction measurements. A single crystal will produce a reflection only when its orientation is such that a certain set of reflecting planes is inclined to the incident beam at an angle θ which satisfies the Bragg law for that set of planes and the characteristic radiation employed. The first step of measuring a pole figure consists then of determining the angle θ of diffraction for the samples. To achieve this objective, a four-stage Scintag rotating anode goniometer was used with copper Kα radiation. Copper does not induce any noticeable fluorescence with copper anode radiation. Furthermore, the Kβ component of copper radiation is reduced by using a Ni filter.

To obtain diffraction angles, a 2θ scan was performed for each specimen. A continuous scan consists of moving the detector through a range of two theta (2θ) from 35° to 80° to determine the angular position for each of the three diffracting planes in the fcc crystal system, {111}, {200} and {220}. The continuous 2θ scan was performed with increments of 0.02° for each step at a rate of 2°/minute. For all specimens, regardless of the processing route and heat treatment, diffractions occur at practically the same angles. Table 3.5 summarizes these results.

The final step involves measuring the intensity of the diffracted x-ray beam for each plane (pole). Each sample was incrementally rotated from 0° through 360° and tilted from 0° through 75°. The detector was positioned in the appropriate angular position for each pole figure. These angles were changed incrementally with 5º step.

The intensity of the diffracted beam decreases for high tilt angles because the incident beam becomes shallower. The effects of defocusing were corrected using an empirical curve measured for a sample with random orientation. The defocusing corrections depend on the alignment of the instrument, the size and shape of the collimator and receiving slit, the diffraction angle 2θ, and the wavelength of the incident beam.

Table 3.5 Diffraction angles for different crystalline planes in pure copper.

<hkl> direction	Angle of diffraction 2θ
<111>	43.3
<200>	50.4
<220>	74.1

The last correction introduced to the pole figure is the completion of the pole figure for tilt angles higher than 75°. The completion is obtained by using the harmonic method which assumes that the orientation distribution (OD) is a smooth function.

3.3.5. X-ray analysis

The grain size in consolidated Cu powders and ECAE processed bulk Cu can be directly determined using TEM micrographs. However the non-uniform grain size distribution from one area to another especially if the material exhibits a bimodal distribution of grain size requires another method for the determination of average grain size. X-ray analyses [79-80] were performed using a Bruker-AXS D8 diffractometer with Cu Kα radiation to determine the average powder and grain sizes in the initial and the as-processed material using the Warren–Averbach method. This was done by

analyzing x-ray peak broadening on both (111)-(222) and (200)-(400) diffraction peak pairs. Grains with sizes less than 0.1 μm cause the broadening of diffraction lines. The extent of broadening is given by Scherrer formula:

$$B = \frac{0.9 \times \lambda}{t \times \cos\theta} \qquad (3.1)$$

where B is the broadening of diffraction peak measured at half of its maximum, and t is the grain size. λ and θ are the wavelength of the incident beam and the diffraction angle respectively. The broadening of the diffraction peaks for very small grains is due to the fact that there are not enough crystallographic planes to assure a cancellation of interference of the beam with different atomic layers. The destructive interference for non diffracted incident beams is due to deeper planes in the crystal and is a result of the periodicity of the crystal. If the path difference between rays scattered between the two planes differs only slightly from an integral number of λ, then the atomic plane permitting the diffraction at exactly the same path difference plus a complete wave length will lie deep within the crystal. A very small grain will not permit then the cancellation to occur.

In reality, all diffraction peaks have a measurable breadth, even if the grain size exceeds 0.1μm, due to divergence and the width of the x-ray beam. The breadth B in the Scherrer formula is due only to the grain size. B is essentially zero for grain sizes higher than 0.1μm. The major challenge in determining particle size from line breadths is to differentiate B from the measured breadth B_M of the diffraction line. The Warren's method is the simplest and consists of using a standard width particle size greater than

0.1μm with a known breadth B_S and having the diffraction line near to the unknown measured grain size. The breadth will be determined by the difference:

$$B^2 = B_M^2 - B_S^2 \qquad (3.2)$$

B_M can be determined directly from the diffraction peaks, the standard breadth B_S is known, and hence the grain size t can be determined directly from the Scherrer formula.

3.4. Mechanical testing procedures

3.4.1. Hardness and density measurements

Microhardness was measured in the consolidates of the manually tapped Cu nanoparticles using the Vickers scale. Hardness measurements were used together with density measurements to determine the effect of different routes and number of passes on the consolidation of Cu powders. Vickers microhardness (HV) measurements were conducted using a Buehler Micromet II microhardness tester on the transverse, flow and the longitudinal planes as described in Figure 2.2. A load of 500 g and a dwell time of 15 s were used. These test parameters ensured a large enough indentation to obtain accurate readings. A good surface is necessary in order to delineate clearly the indentation. Different samples were ground at 600 and 800 grits, and followed by a rough polishing using a 3μm diamond paste. The recommended spacing in-between two neighboring indentations was at least three times the indentation mean diameter and ten times away from the edge of the specimen in order to avoid overlap with any stressed area induced by the application of the load.

The densities of the consolidated samples were determined using Archimedes' principle, according to ASTM specifications for density measurements for porous

materials [81]. Relative densities are based on the measured values and the theoretical density.

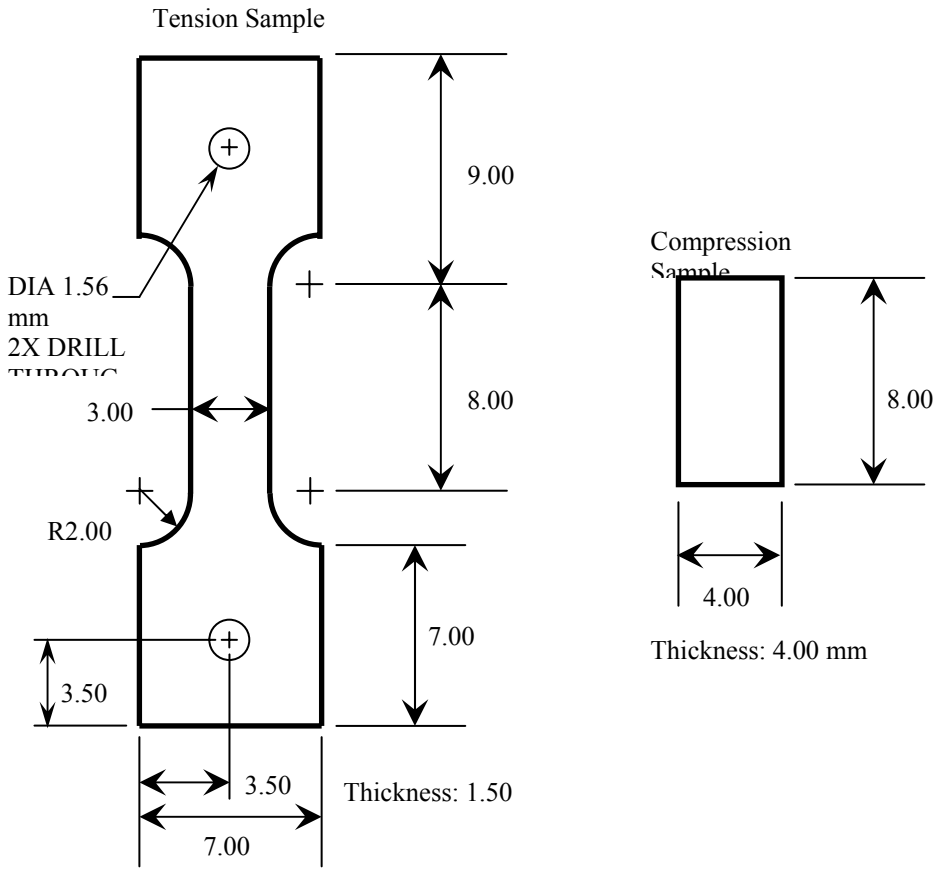

Figure 3.5 Small scale specimens designed for tension and compression testing. All dimensions are in mm.

3.4.2. Tension and compression experiments

Dog-bone-shape flat tensile specimens with nominal dimensions of 8×3×1.5 mm^3 in the gage section and compression specimens with nominal dimensions of 4×4×8 mm^3 (Figure 3.5) were cut by electrical discharge machining (EDM) from consolidates and bulk extruded samples. The surfaces were polished to remove the EDM affected layer.

To test the small specimens and to study the anisotropy in ECAE processed bulk Cu, a small scale testing apparatus was used. This was motivated by the relative small quantity of material yielded by consolidation and also to be sure that the gage section of the testing specimen corresponds to uniformly deformed region of the billet [77]. The small-scale grips used for tension are designed to clamp thin and flat specimens aligned with two pins while compressive grips simply squeeze a rectangular compression specimen (Figure 3.6). The grips are machined from a 17-4 precipitation hardening stainless steel in the annealed state and subsequently aged for 1 hour at 482º and then air cooled to establish the maximum strength and hardness. Both tension and compression grips were designed with the objective of accommodating the miniature extensometer.

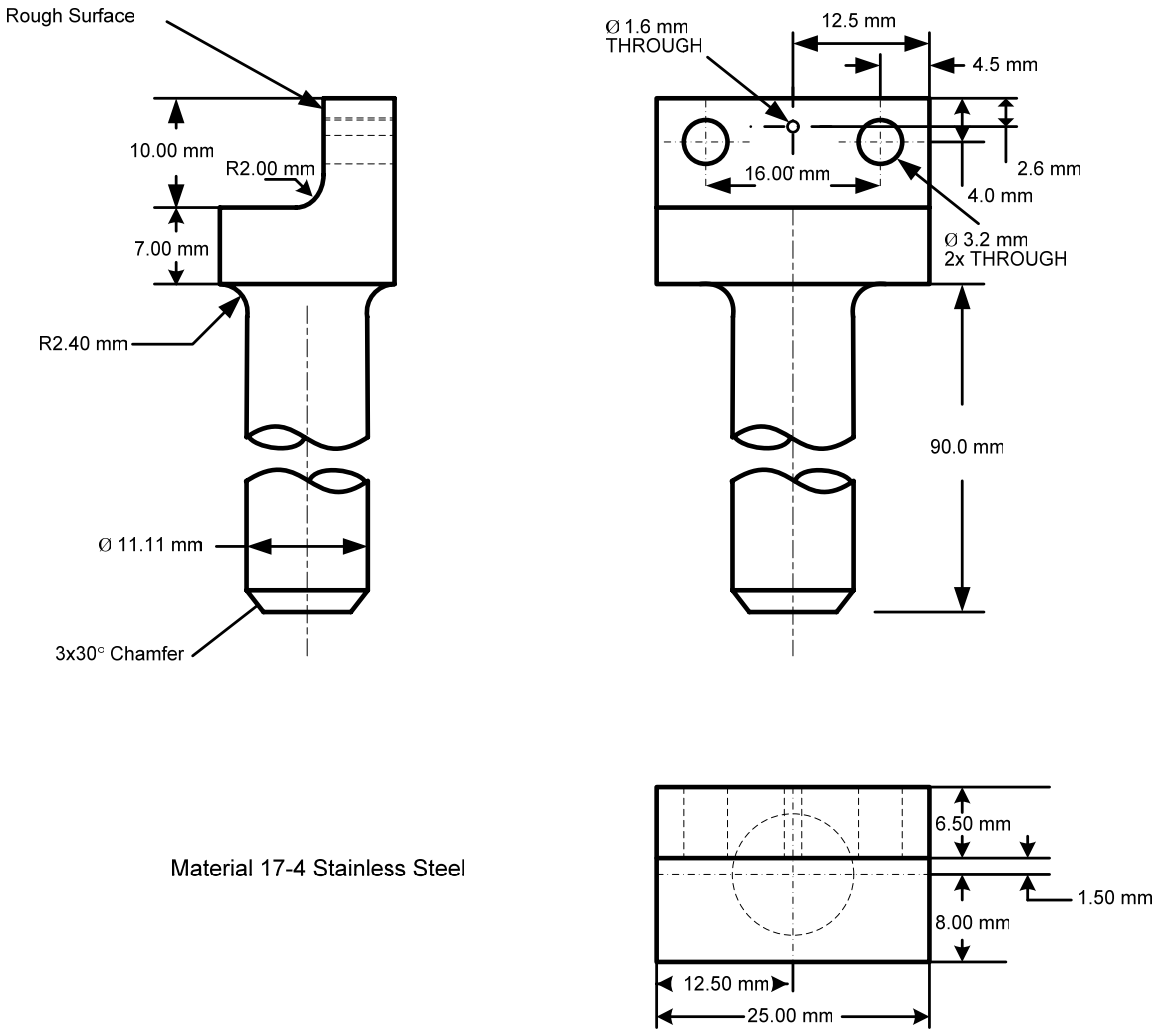

Figure 3.6 Tension (a) and compression (b) test grips designed for the specimens shown in Figure 3.5. The connection clasp is not shown.

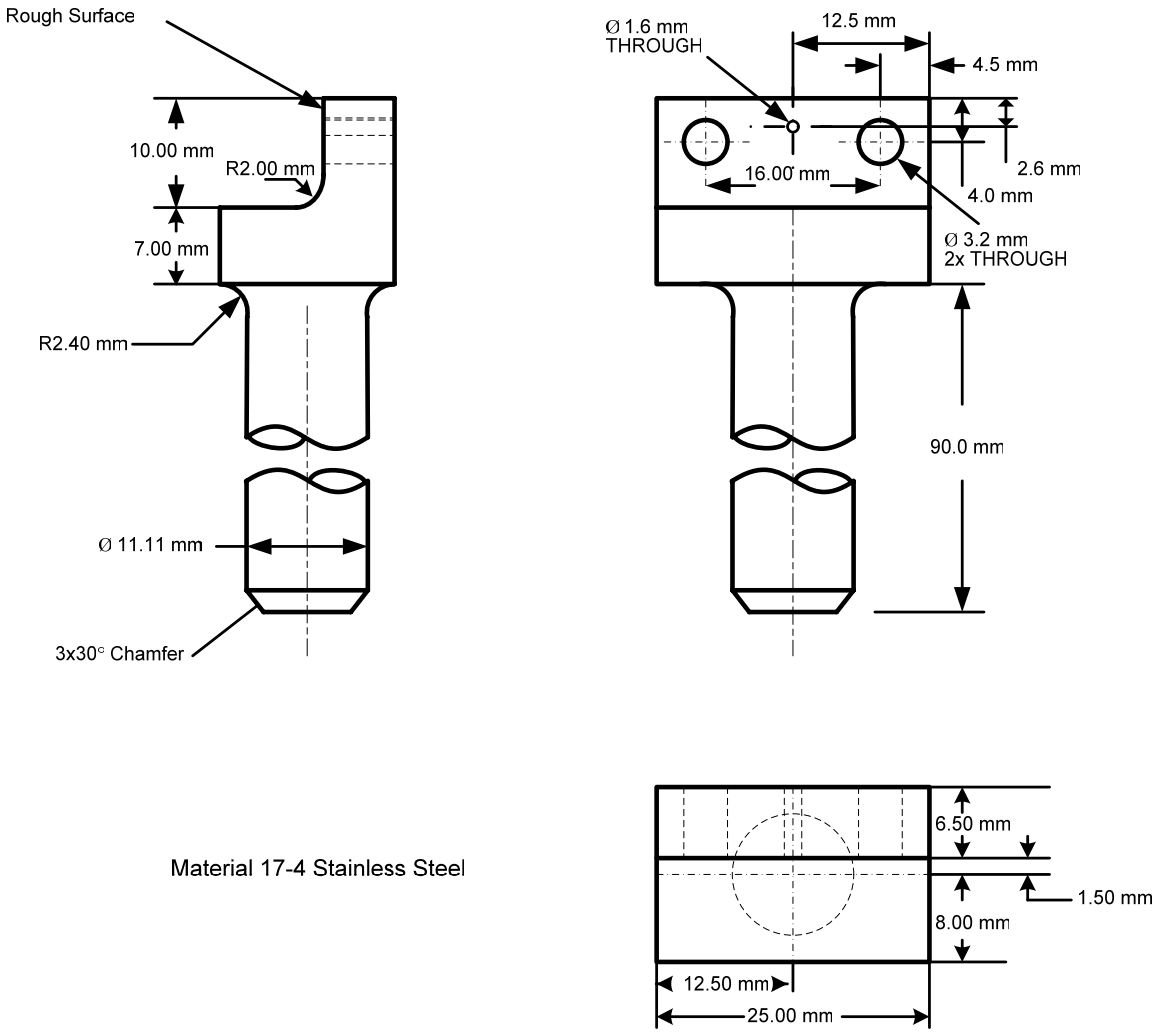

Figure 3.6 Continued.

For the consolidated Cu powders obtained in the first stage of this study where the cans were filled by manual tapping, tension specimens were cut along the extrusion direction (see Figure 2.2). The compression axis of the compression specimens were cut along the direction normal to the flow plane (FD) for the 325 mesh consolidates and normal to the extrusion direction (ED) for the 130 nm consolidates. Experiments were performed at room temperature with a servo-hydraulic MTS test frame under a strain rate of 5×10^{-4} s^{-1}. The strain was measured with a miniature extensometer (3 mm gage

length) mounted on the specimens in both tension and compression experiments. Teflon tape was used in between compression platens and the compression specimens to minimize the friction. Neither buckling nor barreling was observed on the specimens after compression. For Stages 2 and 3 of Cu powders consolidation, only tension experiments were conducted. The tensile axis of the tension specimens is summarized in Table 3.4. For the case 4B, the tension specimen was EDM cut on the final shear plane with tensile axis along the shear direction as shown in Figure 3.7 in order to reduce the effect of shear banding in the response of the specimen in tension. The shear plane is defined as the final position, after subjecting a billet to a given deformation schedule, of a plane parallel to the initial cross section. Figure 3.8 shows an example of a shear plane for 2B case.

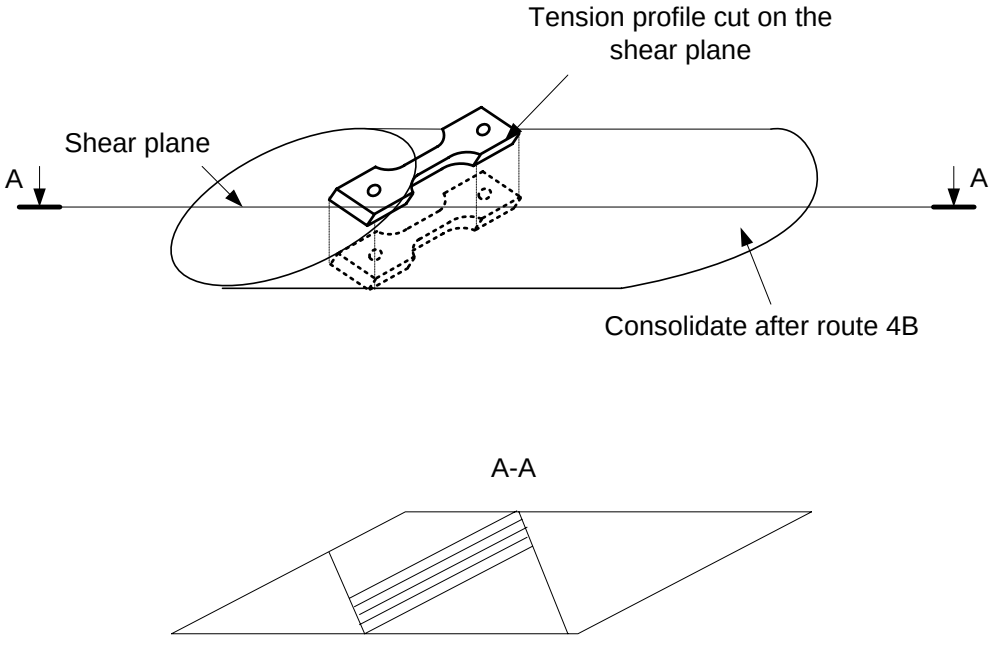

Figure 3.7 Schematic of the tension specimen profile EDM cut on the shear plane along the shear direction in the case of route 4B.

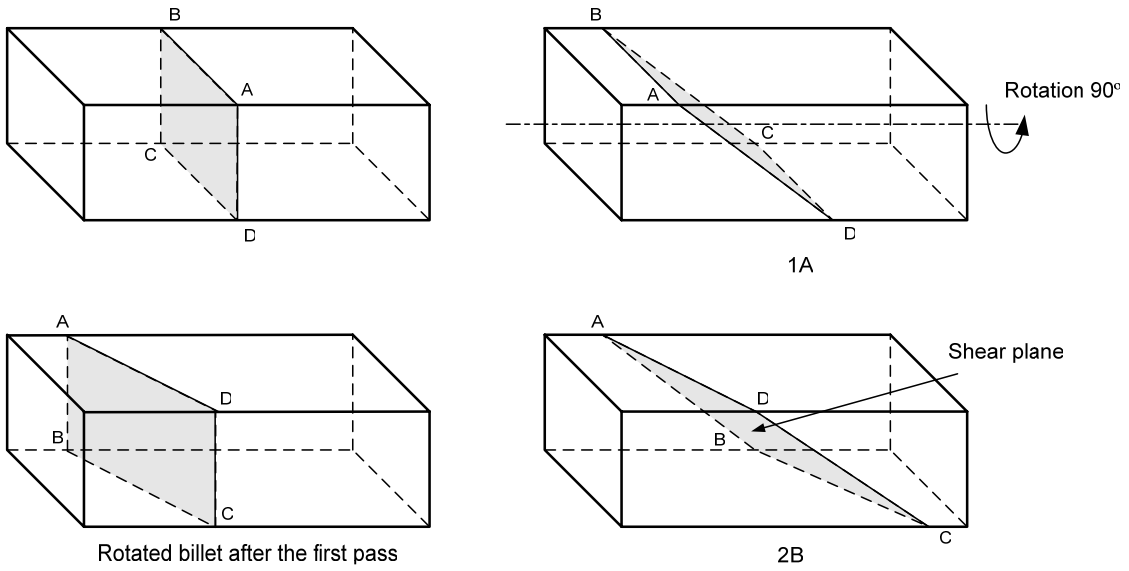

Figure 3.8 Evolution of the shear plane after one pass and two passes via route B.

To study the anisotropy in ECAE processed bulk Cu, specimens were cut along three perpendicular directions as shown in Figure 3.9, i.e. tensile axis along the extrusion direction (T), and flow direction (F) with the flat surfaces of the samples parallel to the longitudinal plane, and longitudinal direction (L) with the flat surface of the samples parallel to the flow plane. In the 4A case, specimens were also cut on the ECAE shear plane with tensile axis along the shear direction. The specimens were inspected to ensure that buckling did not occur during Bauschinger experiments (BE) where prestrained specimens up to 1% in compression were tested in tension. Two to three experiments were conducted on companion specimens to check the repeatability of the results. The thickness of tension specimens is always 1.5 mm.

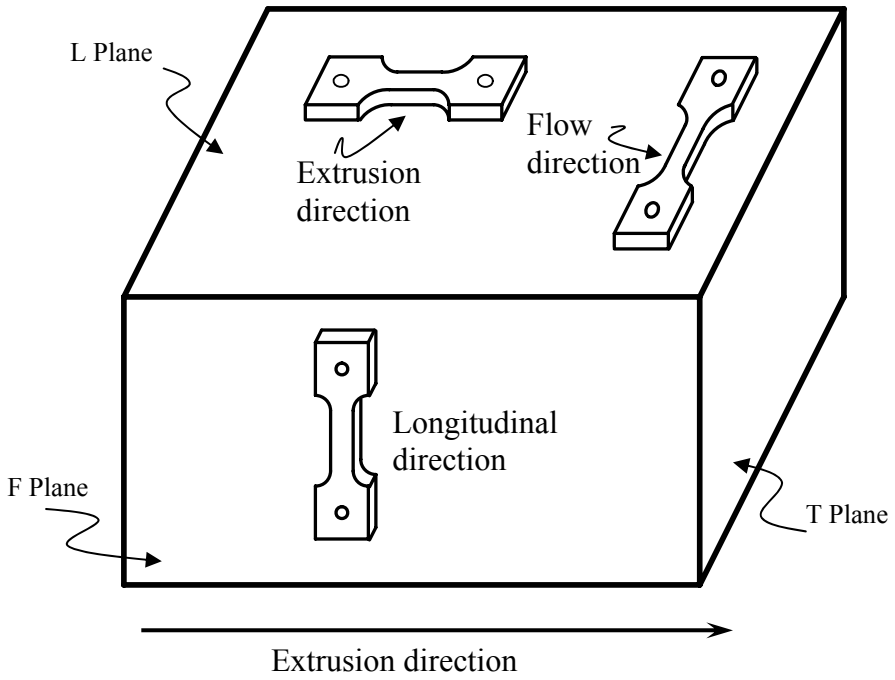

Figure 3.9 Orientation of tension samples tested along three perpendicular directions.

The engineering stress-strain does not give a correct indication of the mechanical behavior of the material because it is based on the original dimensions of the specimen tested, and dimensions change continuously during testing. True stress and true strains are then considered to account for the variation of specimen dimensions. True values are calculated from the measured engineering stress and strain values by taking into consideration the conservation of volume of the specimens during the test. True stress σ and engineering stress s can be expressed as follows:

$$\sigma = \frac{P}{A} \text{ , and } s = \frac{P}{A_0} \qquad (3.3)$$

where A and A_0 are respectively the instantaneous and initial cross sections of the tension specimens. Using the constancy of volume, we can deduce relationships

between true stress σ and engineering stress s and also between true strain ε and engineering strain e:

$$\begin{aligned} \sigma &= s(e+1) \\ \varepsilon &= \ln(e+1) \end{aligned} \qquad (3.4)$$

These relationships are valid only up to σ_{UTS} where necking occurs.

CHAPTER IV

MECHANICAL BEHAVIOR AND ANISOTROPY IN WROUGHT COPPER

The effect of strain and strain path on the mechanical properties namely the evolution of strength and ductility and yield anisotropy, in wrought ultra fine grained oxygen free high conductivity copper is investigated in terms of grain microstructural features and texture yielded by each route. The material was deformed via equal channel angular extrusion (ECAE) to different strains following routes (A, B, C, C' and E). The mechanical behavior through tension and compression tests is related to the shape, dimension and spatial orientation of the grains produced in each configuration of route and number of passes. Tension experiments show that an early plastic instability takes place leading to a continuous softening of the flow stress of bulk ECAEd copper after the first pass. Increases in both strength and ductility are evident with increasing numbers of passes in the bulk samples which appear to be inconsistent with grain boundary moderated deformation mechanisms for a microstructure with an average grain size of 300-500 nm. Instead, this increase is attributed to microstructural refinement and to the dynamic recovery and bimodal grain size distribution. It is also shown that grain morphology has a strong impact on the mechanical response for different directions and competes with texture and grain refinement in controlling the yield strength. Grain morphology can explain the anisotropy exhibited by ECAE processed Cu and induces a drop of strength with the number of passes for a specific direction. A stronger compression is found not to be systematic in UFG materials and rather the tension-

compression asymmetry is affected by grain morphology through the interaction between dislocations and grain boundaries.

4.1. Experimental results

4.1.1. Microstructural evolution

Although ECAE has been mainly considered as a way to refine grain size, the grain morphology can also be controlled by careful selection of the route and number of passes. For pure geometrical reasons, a grain is subjected to simple shear after its passage through the right angle of the die. We assume that the grain interior can deform according to the externally imposed shape change, compatibility across the grain boundaries is satisfied (5 independent deformation systems are available). If we consider furthermore that the initial grains have cubic shape as shown in Figure 4.1 demonstrates, a three dimensional view of grain morphology after being subjected to different routes and number of passes can be illustrated. Note that this is a pure geometrical consideration and grain division or subgrain formation are not taken into account. It can be assumed that the initial high angle grain boundaries can deform following the geometrical constraints but subgrain formation may occur in a different fashion. In route C, the initial cubic element recovers its initial shape for an even number of passes, while in route C', the successive rotation of the billet by 90˚ in the same direction reproduces the initial shape after four passes (Figure 4.1.a). In route A (Figures 4.1.b, c, and e), billets are not rotated in successive passes, resulting in the elongation of the primary cubic element creating a lamellar structure similar to that obtained by rolling.

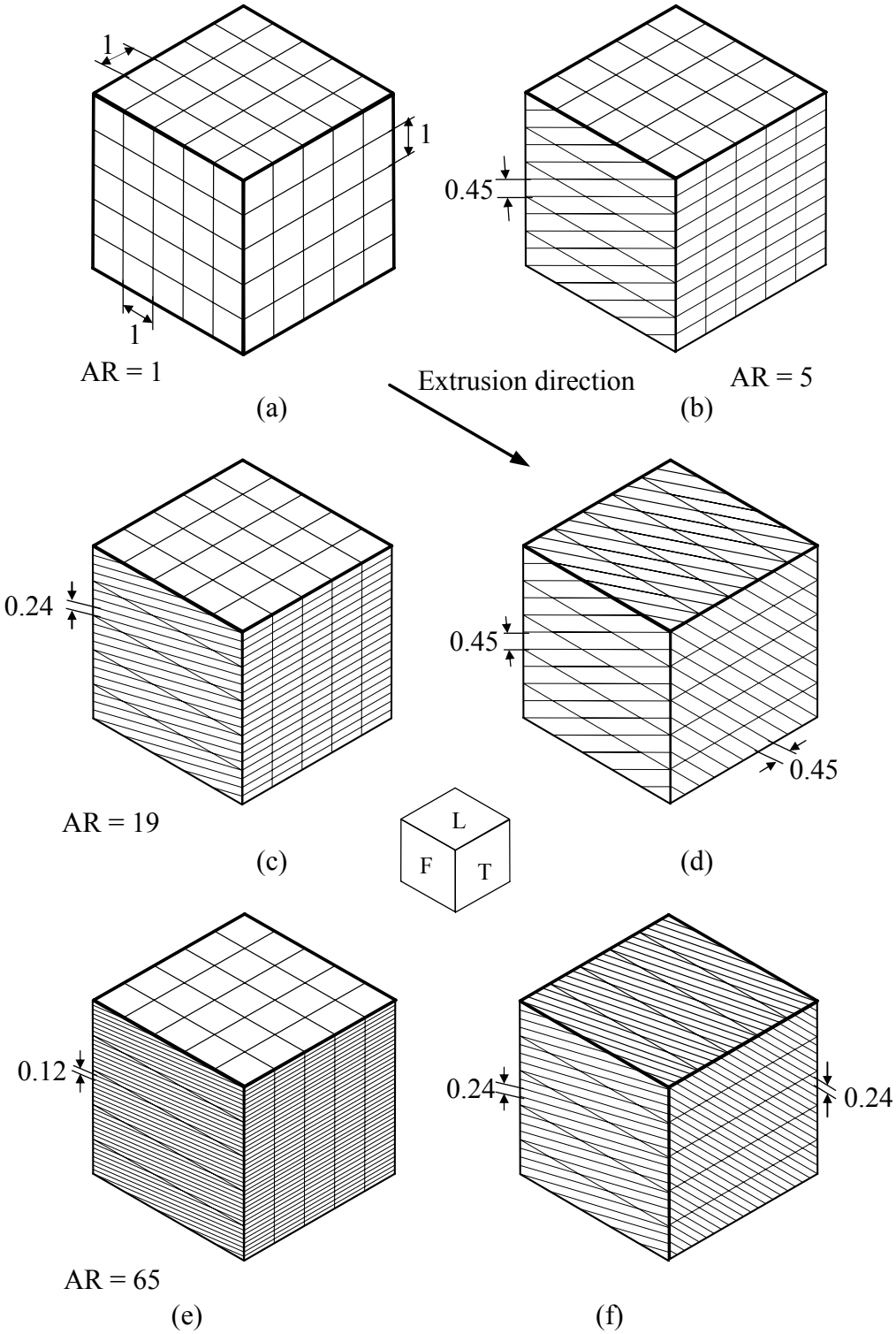

Figure 4.1: Projection of initial cubic shaped grains in three perpendicular planes after different ECAE routes and number of passes: (a) initial configuration, 2C, 4C, and 4C', (b) 1 ECAE pass, (c) 2A, (d) 2B, (e) 4A, and (f) 4B. L: longitudinal plane, T: transverse plane, F: flow plan and AR: grain aspect ratio.

The theoretical inclination angle φ_n (Figure 4.2) of the elongated grain with respect to the extrusion direction follows the equation (4.1):

$$\tan(\varphi_n) = \frac{1}{2 \times N} \qquad (4.1)$$

where N is the number of passes. As seen in Figure 4.1, there is an apparent reduction in grain thickness in the transverse plane and increase in the aspect ratio with the number of passes (the aspect ratio values for route A are reported in Figure 4.1). In route B, the ±90˚ rotation of the billet successively leads to the inclination of the grains in two perpendicular planes consequently reducing the aspect ratio of the grains. Grains are deformed in both longitudinal and flow planes instead of only the flow plane as in the case of route A. The angle φ_n for route B can be evaluated in the case of an even number of passes by the equation:

$$\tan(\varphi_n) = \frac{1}{N} \quad (4.2)$$

for both L and F planes of view. The inclination of grains in the transverse plane is 45° after even passes. The aspect ratio AR can be defined as (a and b are shown in Figure 4.2):

$$AR = \frac{a}{b}$$

$$a = \frac{1}{\sin \varphi_n} \text{ and } b = \sin \varphi_n \qquad (4.3)$$

$$\text{thus } AR = \frac{1}{\sin^2 \varphi_n} = 1 + \frac{1}{\tan^2 \varphi_n}$$

hence the aspect ratio can be related directly to the number of passes in route A by the relation:

$$AR = 1 + 4 \times N^2 \qquad (4.4)$$

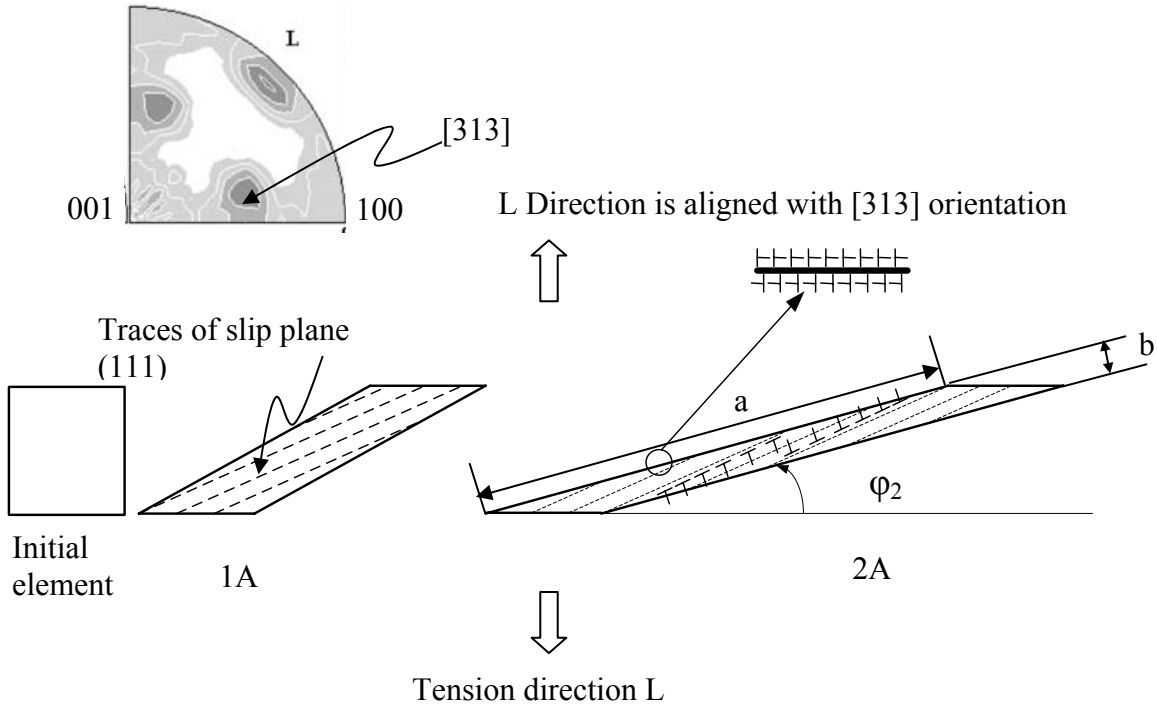

Figure 4.2: Deformation of a square initial element after 1 and 2 passes following route A. The dislocation path is increased with the number of passes. Polarization of the grain boundaries after plastic deformation.

Table 4.1 summarizes the calculated microstructural characteristics for different routes and number of passes. Figure 4.3 shows the back scattered electron micrographs of the ECAE processed Cu. These images seem to agree well with the observations made above based strictly on the geometrical evolution of a cubic mesh when sheared through a right angle corner. The inclination angles of the shear bands and alignment of the subgrains seem to match with the value predicted in equation (4.1) in both micrographs in Figures 4.3.a and 4.3.b corresponding to the flow plane in route A for 1 and 4 passes,

respectively. The thickness of the elongated grains decreases with the number of passes as predicted in Figure 4.1. However, the length of the grains along the long direction is shorter, i.e. aspect ratio is smaller indicating that a splitting grain process took place. Figure 4.3.c shows the distribution of grains in the longitudinal plane for 2A case. The microstructure is fairly equiaxed and is in agreement with the geometrical expectations in Figure 4.1.

Table 4.1 Processing routes and calculated geometrical factors from an initial cubic element of unit side.

ECAE route	Number of passes	Inclination angle (deg), φ_n	Aspect Ratio, AR	Grain thickness, b
A	1	26.6	5	0.45
	2	14.0	19	0.24
	4	7.1	65	0.12
	8	3.6	257	0.06
B	2	26.6	-	0.45
	4	14.0	-	0.24
C	2	90º	1	1
	4	90º	1	1
C’	4	90º	1	1

Figure 4.4 shows the effect of increasing the number of extrusion passes on the microstructural evolution. In the three cases 1A, 2C, and 4C investigated with transmission electron microscopy, the foils were prepared with the foil normal being perpendicular to the flow plane (see Figure 2.2). As expected, the grains are elongated as the material undergoes shearing in the abrupt corner of the die. The microstructure in the 1A sample reveals a relatively low dislocation density with the formation of subgrains. The dislocation density increases with the number of passes leading to the formation of small grains with high angle grain boundaries.

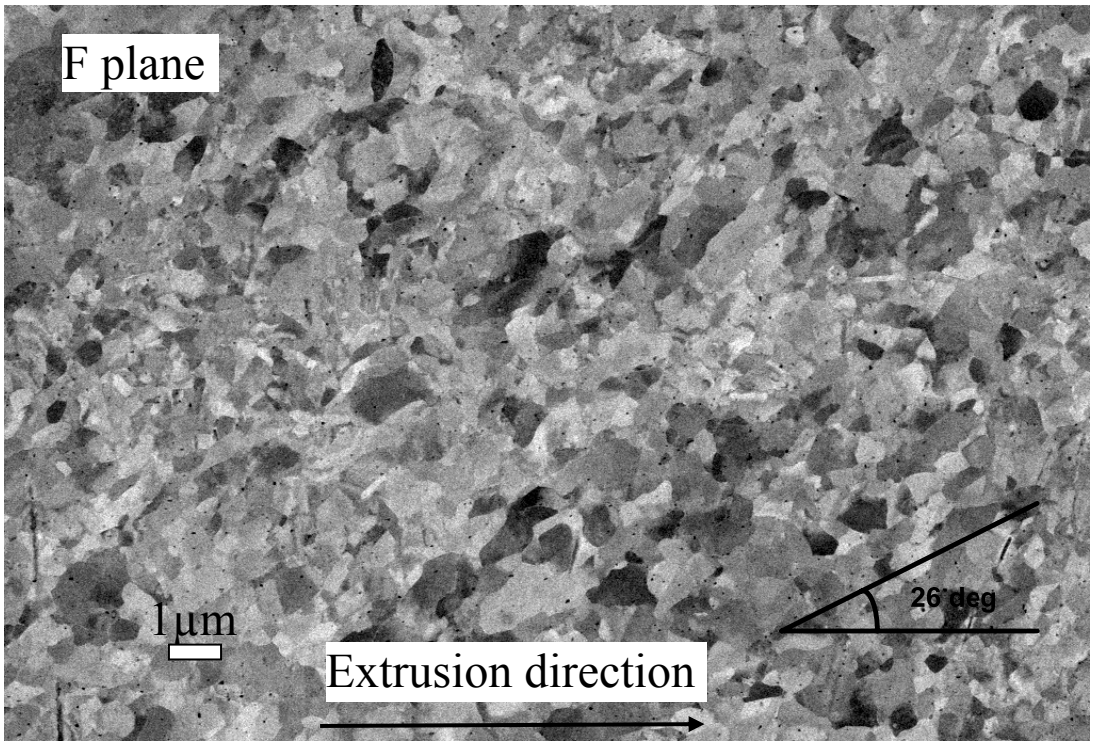

(a)

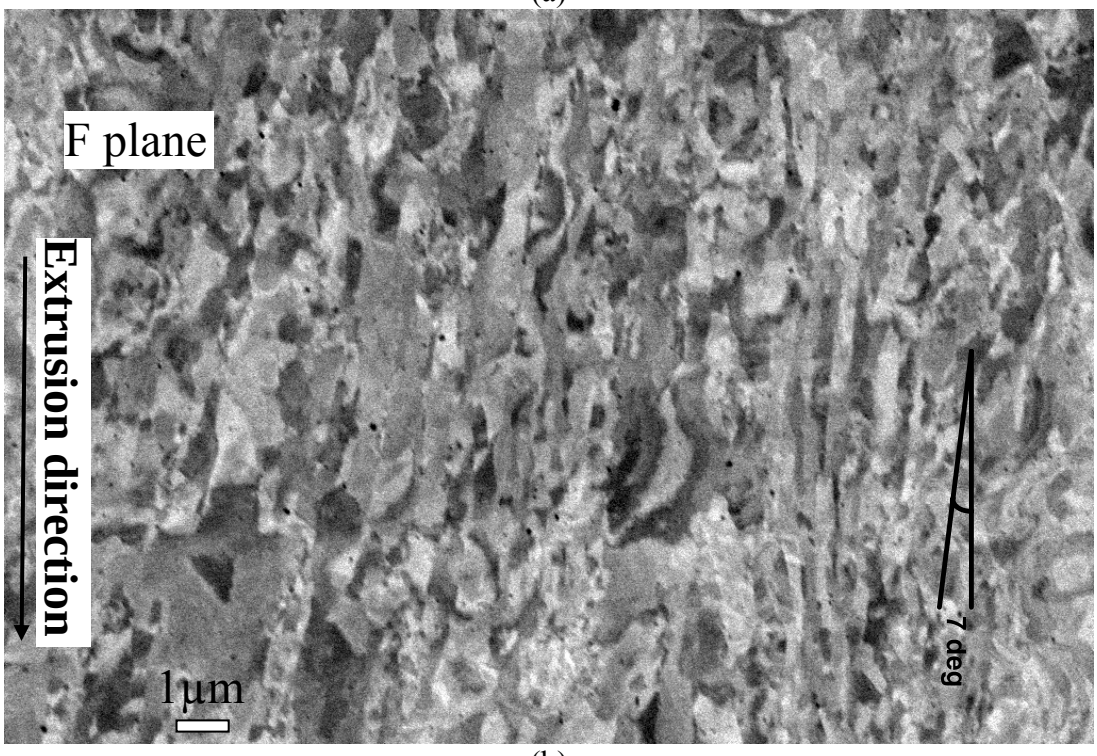

(b)

Figure 4.3: Back scattered electron micrographs of ECAE processed Cu after (a): 1A on the flow plane, (b): 4A on the flow plane, (c): 2A on the transverse plane, (d): 2B on the transverse plane.

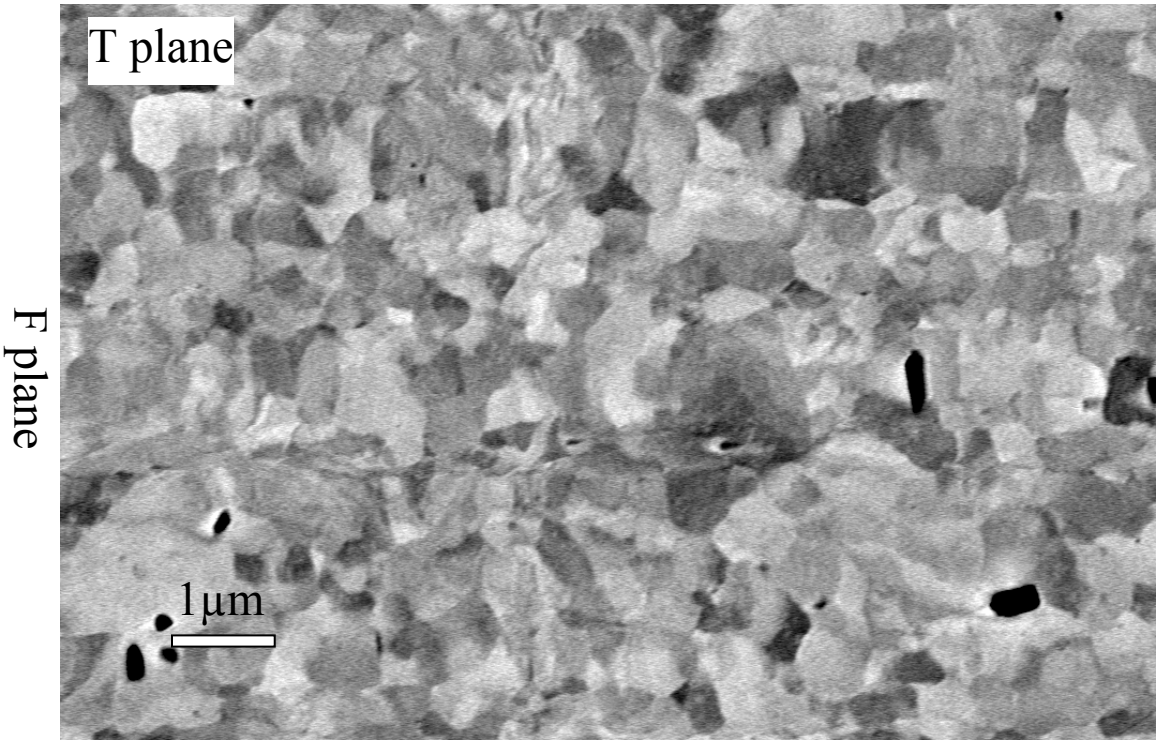

(c)

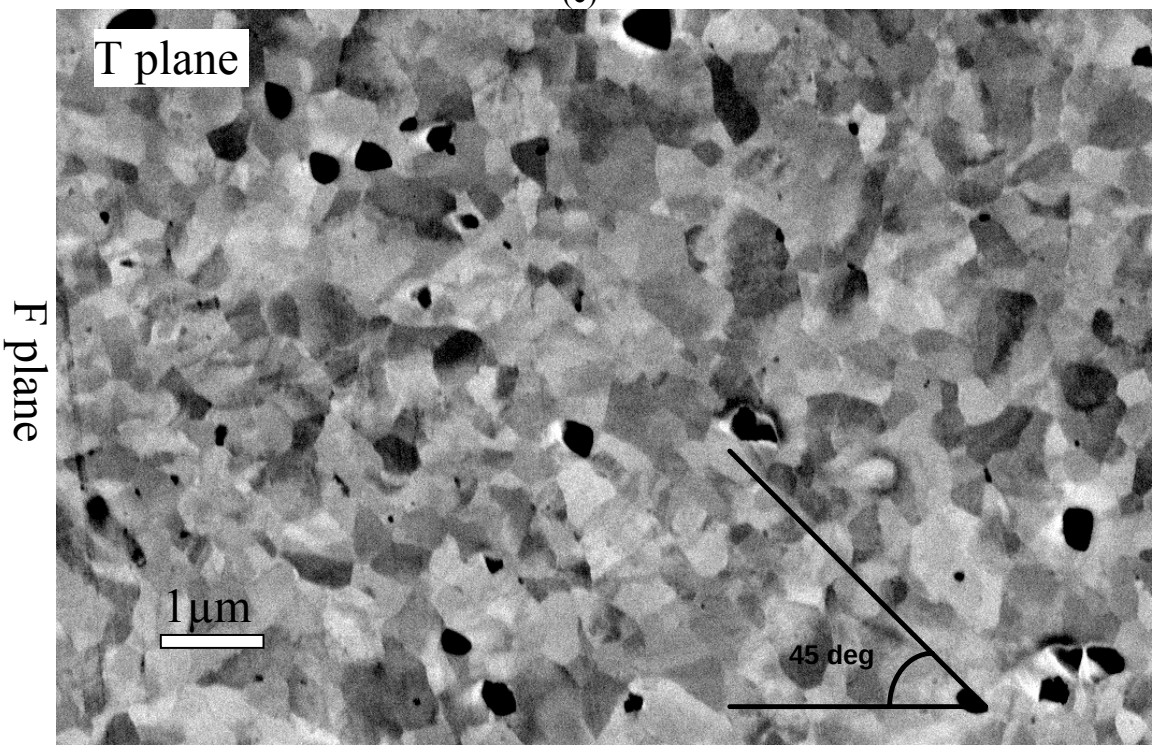

(d)

Figure 4.3 Continued

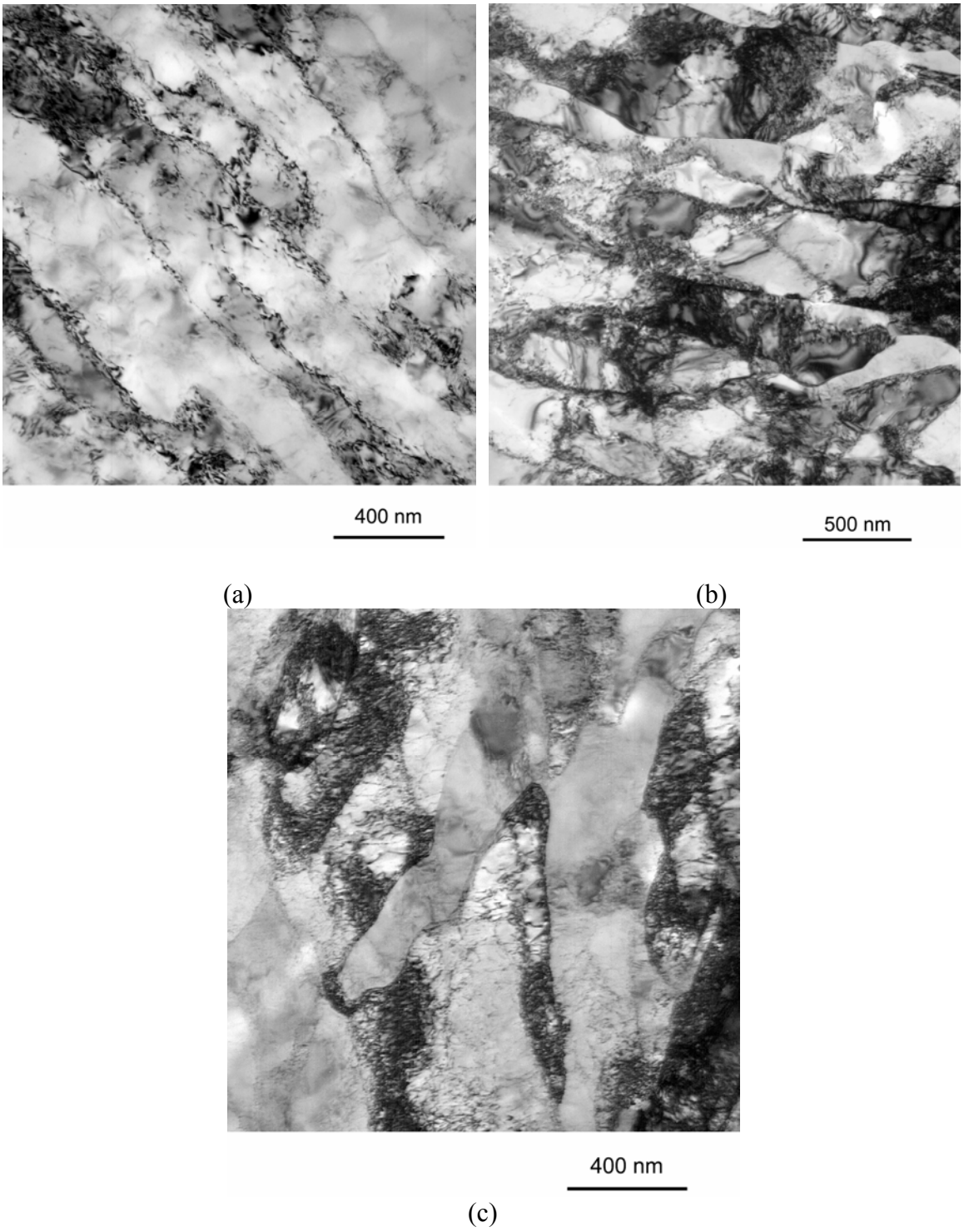

Figure 4.4: Bright field TEM micrographs of ECAE processed bulk Cu. (a) ECAE 1A, (b) ECAE 2C, and (c) ECAE 4C. The foil normal is perpendicular to the flow plane as shown in Figure 2.2.

The common microstructural evolution route for ECAE processed copper starts with the formation of low-angle cellular structures inside the initial large grains (Figure 4.4.a). With increasing strain (increasing number of passes), the misorientation across some of the low-angle subgrain boundaries increases due to trapped lattice dislocations forming high-angle grain boundaries (Figures 4.4.b and c). A further increase in strain increases the fraction of high-angle grain boundaries and provides further grain refinement. However, the grain size usually saturates at a certain size range depending on the purity of the material because of the balance between dislocation generation and recovery. Therefore, achieving grain sizes below 100 nm may not be possible with ECAE of initially coarse grained highly pure copper.

4.1.2. Room temperature tensile response

True stress and true strain were calculated from engineering stress and engineering strain using the constant volume assumption [82]. In Table 4.2, all yield strength $\sigma_{y(0.2\%)}$, ultimate strength σ_{UTS} and fracture strain ε_f values are reported. Table 4.3 summarizes these measurements by giving the average of $\sigma_{y(0.2\%)}$ and σ_{UTS} as well as the corresponding standard deviation. In the same table are reported ε_f values. In some cases there are big discrepancies in ε_f values, so the highest fracture strain measurement was considered or in the case where more than two tests were conducted the average of the highest values were taken into account. The shaded values of ε_f are those considered in the determination of the average in Table 4.3. To study the mechanical anisotropy in ECAE processed Cu, Monotonic tests under tension were conducted along the three perpendicular directions in each billet i.e. longitudinal, extrusion and flow (Figure 3.9).

Table 4.2 Summary of yield strength, ultimate strength, and strain at fracture values for different ECAE schedules and directions of testing.

Route	Direction	$\sigma_{y(0.2\%)}$ (MPa)					σ_{UTS} (MPa)			ε_f (%)		
		Spec 1	Spec 2	Spec 3	comp	Baus C-T*	Spec 1	Spec 2	Spec 3	Spec 1	Spec 2	Spec 3
1A	Long	330	295	315	354	276	358	350	358	37	13	29
	Extrusion	336	338	338	306	276	355	363	368	31	25	30
	Flow	344	363	358	429	340	390	407	403	23	30	17
2A	Long	279	294	-	370	288	389	392	-	36	29	-
	Extrusion	362	371	374	294	287	381	382	387	26	25	11
	Flow	446	455	-	481	389	465	479	-	19	12	-
2B	Long	299	285	-	398	292	406	406	-	29	37	-
	Extrusion	402	378	-			424	418	-	26	27	-
	Flow	413	407	-	445	370	444	441	-	25	19	-
2C	Long	358	349	-	320	280	405	394	-	36	30	-
	Extrusion	372	397	-	345	322	398	419	-	34	23	-
	Flow	380	368	-	466	379	451	452	-	30	15	-
4A	Long	277	276	-	343	283	398	407	-	37	37	-
	Extrusion	373	377	-	306	300	400	400	-	32	16	-
	Flow	453	438	-	494	405	481	470	-	14	26	-
	Shear	397	-	-	308	325	430	-	-	35	-	-
					306	326						
					Tens	Baus T-C						
					383	306						
					378	307						
4B	Long	285	272	-	387	310	413	403	-	32	18	-
	Extrusion	409	398	-	338	338	445	436	-	33	18	-
	Flow	380	378	-	434	360	445	446	-	25	15	-
4C	Long	300	304	-	369	310	420	425	-	40	38	-
	Extrusion	390	402	-	355	328	431	435	-	34	27	-
	Flow	435	435	-	460	367	474	479	-	29	12	-
4C’	Long	293	297	-	334	265	423	433	-	38	38	-
	Extrusion	399	414	-	332	326	451	453	-	37	25	-
	Flow	389	393	-	426	341	450	451	-	36	18	-
4E	Long	313	294	-	445	320	434	428	-	39	24	-
	Extrusion	401	392	414	352	332	440	428	445	36	38	22
	Flow	412	401	-	455	380	457	452	-	21	31	-
8A	Extrusion	380	-	-	313	322	439	-	-	36	-	-
					Tens	Baus T-C						
					374	310						
8E	Extrusion	409	402	-	354	364	437	453	-	37	21	-
16E	Extrusion	387	-	-	361	347	435	-	-	20	-	-

Table 4.3 Averages and standard variations of the strength values reported in Table 4.2.

Route	# of pass	Directions								
		Longitudinal			Extrusion			Flow		
		$\sigma_{y(0.2\%)}$ (MPa)	σ_{UTS} (MPa)	ε_f (%)	$\sigma_{y(0.2\%)}$ (MPa)	σ_{UTS} (MPa)	ε_f (%)	$\sigma_{y(0.2\%)}$ (MPa)	σ_{UTS} (MPa)	ε_f (%)
A	1	312±9	355±2	33	337±1	362±3	30	355±5	400±4	26
	2	286±5	390±1	32	369±3	383±2	25	450±3	472±5	19
	4	276±0	402±3	37	375±1	400±0	32	445±5	475±4	26
	8	-	-	-	377±2	439±2	35	-	-	-
B	2	292±5	406±0	33	390±8	421±2	26	410±2	442±1	25
	4	278±5	408±3	32	403±4	440±3	33	379±1	445±0	25
C	2	353±3	399±4	33	384±9	408±7	34	374±4	451±0	30
	4	302±1	422±2	39	396±4	433±1	34	435±0	476±2	29
C’	4	295±1	428±3	38	406±5	452±1	37	391±1	450±0	36
E	4	303±7	431±2	39	402±5	437±4	37	406±4	454±2	31
	8	-	-	-	405±2	445±0	37	-	-	-
	16	-	-	-	387	435	20	-	-	-

Figure 4.5 shows two extreme examples of anisotropy encountered in 4A and 4E cases. Additional samples with tensile axis along the shear direction (specimen cut from the shear plane inclined at 7.1º) were also tested in the 4A case. The flow direction can be singled out from this group of directions because of the high ultimate strength and the early softening. The fracture strain is also lower for the flow direction.

In order to assess the mechanical anisotropy in each route and its evolution with number of passes in more detail, the yield strength σ_y (at ~0.2 %) and the ultimate tensile strength, σ_{UTS}, values were plotted as function of the number of passes for each direction. The corresponding standard deviation values were calculated and reported in the yield and ultimate strength plots. As shown in these plots the variation in the repeated experiments is relatively small.

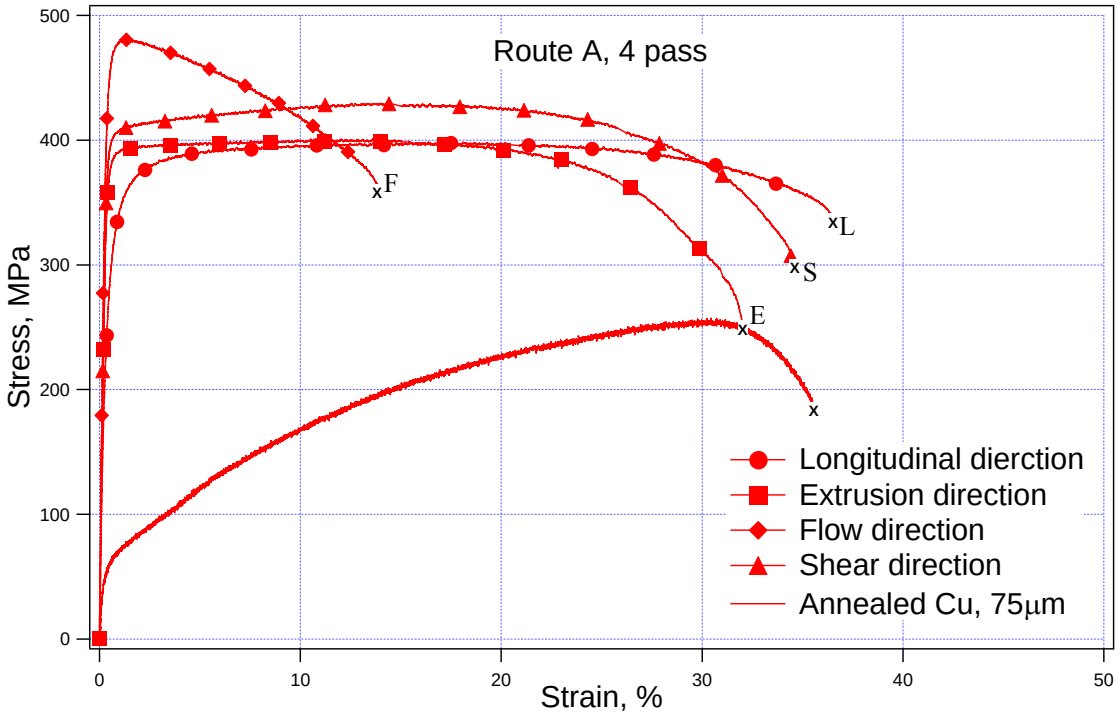

(a)

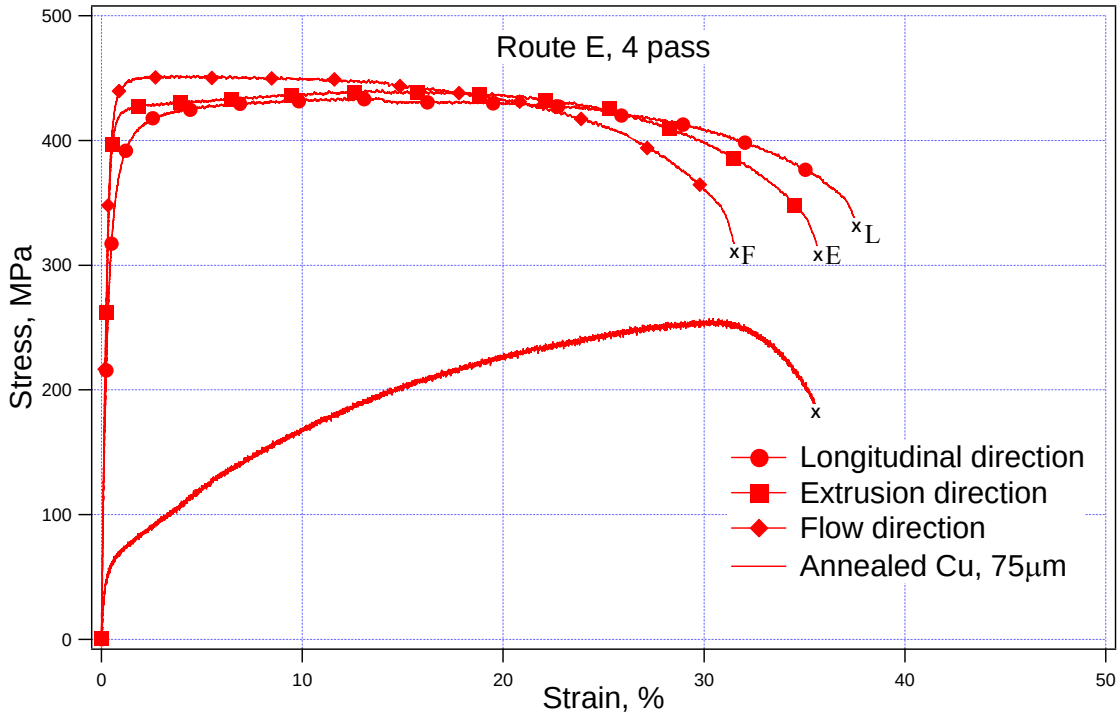

(b)

Figure 4.5: Tensile tests along, (a): four directions for 4A, and (b): three directions for 4E.

4.1.2.1. Routes A, and C

For route A (Figure 4.6.a), regardless of the number of passes, the flow direction exhibits the highest values for σ_y and σ_{UTS} while the yield strength is the lowest for the longitudinal direction. The flow stress increases with the number of passes for both extrusion and flow directions. The increase is more significant between the first and second pass. After the 4^{th} pass, the stress levels saturate and no significant increase is observed with the number of passes. However, σ_y decreases along the longitudinal direction. Interestingly, the same observations can be made for route C (Figure 4.6.b) with the exceptions that between the first and second passes, the σ_y value does not increase substantially for the flow direction and it increases for longitudinal direction as opposed to route A.

4.1.2.2. Route E

Route E is a hybrid route which involves the rotation of the billet 180º and 90º in the even and odd passes respectively. Therefore, route E shares the same strength values with route C in the first two passes. As compared to route C after 4^{th} pass, both σ_y and σ_{UTS} experience a reduction in strength increase along the flow direction resulting in yield strength equal to the one along the extrusion direction (Figure 4.6.c). More tension experiments were conducted on samples after 8 and 16^{th} passes using route E along the extrusion direction. σ_y and σ_{UTS} exhibit a slight increase in the eight pass but overall, the strength levels seem to stabilize after the 4^{th} pass.

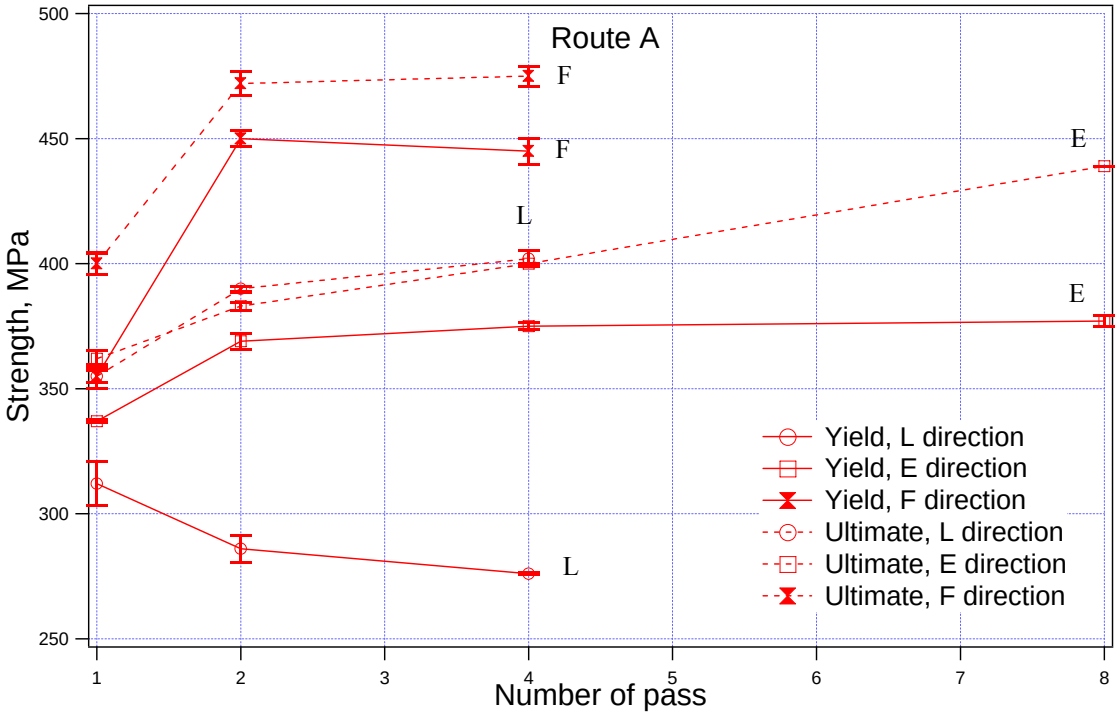

(a)

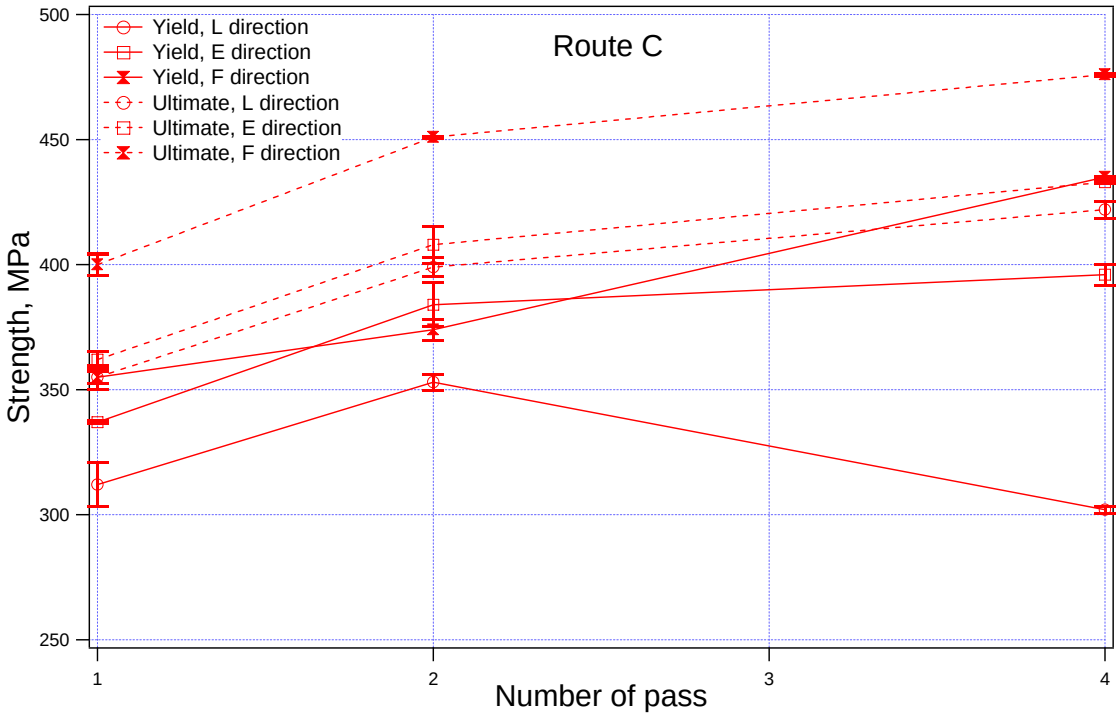

(b)

Figure 4.6: Yield and ultimate strength values for the longitudinal, flow, and extrusion direction for (a): route A, (b): route C, (c): route E, (d): route B, (e): route C'.

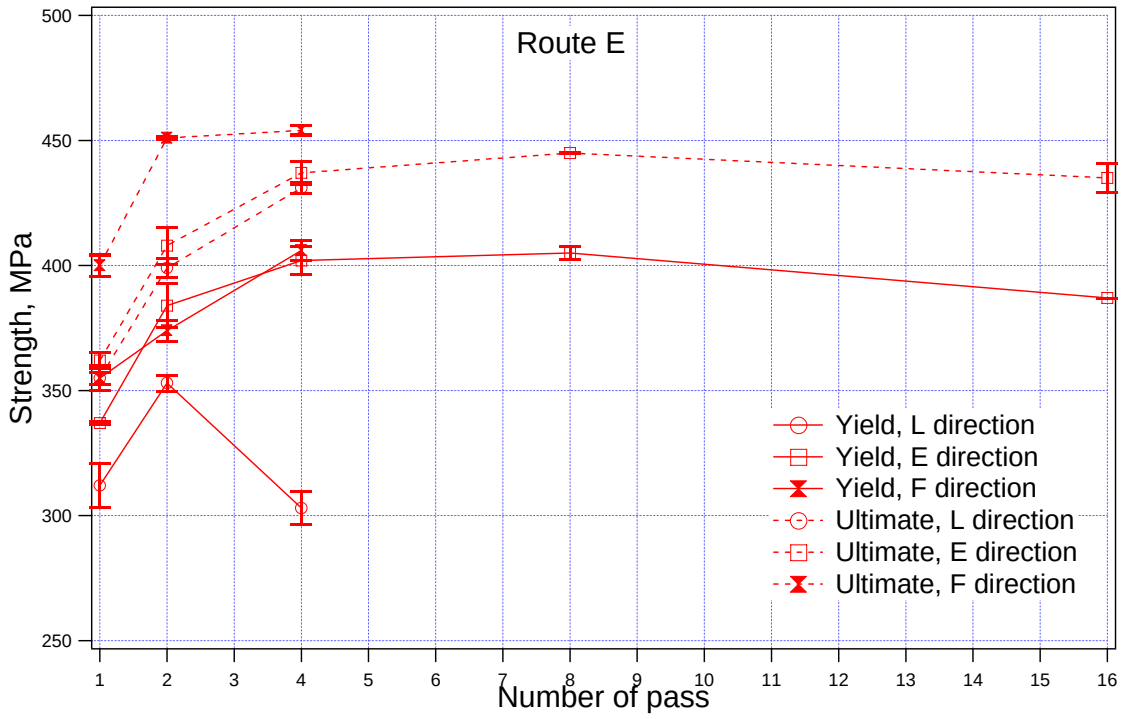

(c)

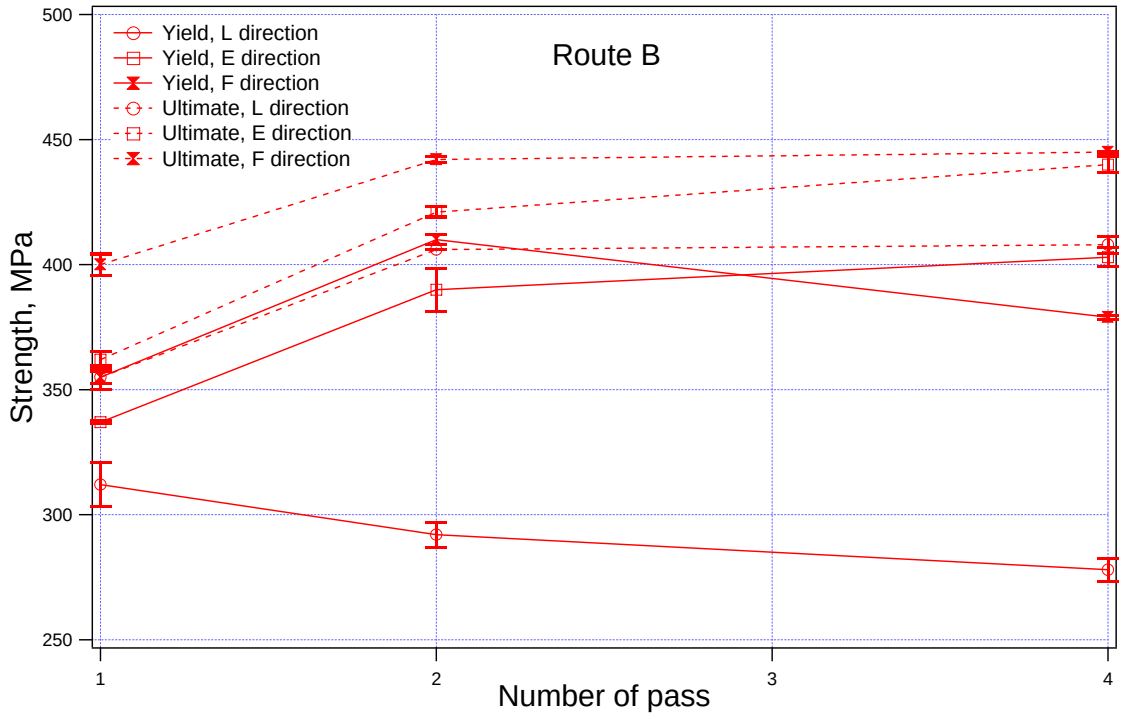

(d)

Figure 4.6 Continued.

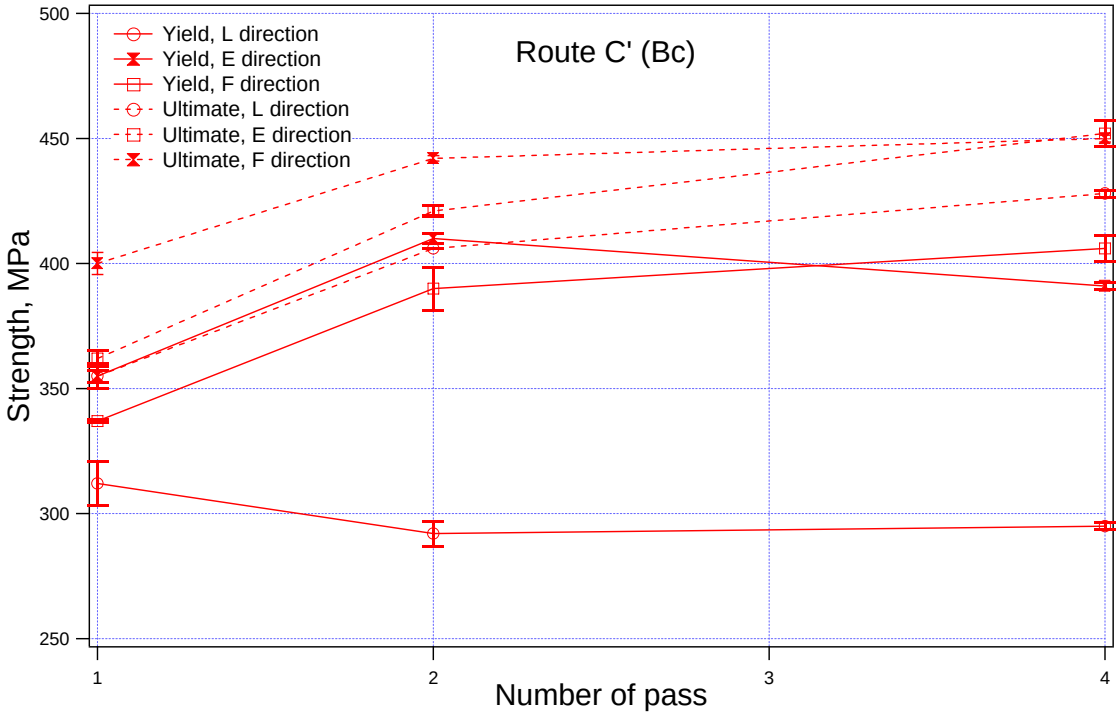

(e)

Figure 4.6 Continued.

4.1.2.3. Routes B, and C'

σ_y and σ_{UTS} for routes B and C' (Bc) (which are the same for the first and second passes), seem to stay constant after the second pass regardless of the direction. It is important to note that for both routes σ_{UTS} tend to be the same for both extrusion and flow directions in the fourth pass (Figure 4.6.d,e). With the exception that σ_y decreases between the second and the fourth pass along the flow direction, the other evolution trends remain similar to route A, i.e. increase of σ_y and σ_{UTS} along the E and F and σ_{UTS} along L directions and decrease of σ_y along L direction.

4.1.3. Tension-compression asymmetry

It is also important to study the tension-compression (T/C) asymmetry in ECAE processed copper prior to discussing the Bauschinger effect to account for any prior T/C asymmetry effect in virgin samples in the interpretation of the Bauschinger experiment results. This asymmetry of plastic deformation is known as the stress differential or SD [83] effect in polycrystalline materials. The SD effect can be quantified by the ratio:

$$\Delta = \frac{\left(\sigma_y^c - \sigma_y^t\right)}{0.5 \times \left(\sigma_y^c + \sigma_y^t\right)} \qquad (4.5)$$

where σ_y^t and σ_y^c are yield strengths in tension and compression of virgin samples not subjected to any prior prestrain. Table 4.4 summarizes the SD values for different routes and number of passes for the three directions. It is worth noting that regardless of the route and number of passes the SD ratio is always negative for the extrusion direction (the material is stronger in tension than in compression). The SD is positive for all the other cases except for the L direction for two passes via route C.

Table 4.4 Stress differential values for the three directions for different routes and number of passes.

		Stress Differential SD (%)		
Route	# of passes	L Dir	E Dir	F Dir
A	1	12.9	-13	19.3
	2	26.1	-25.7	6.9
	4	21.4	-26.6	10
		Shear direction: SD=-33.5%		
	8	-	-29.1	-
B	2	31.2	-	7.3
	4	24.3	-29.6	11
C	2	-10.1	-15.1	22.5
	4	14.7	-19.4	4.3
C' (Bc)	4	11.8	-26.2	5.7
E	4	38.4	-20.9	11.8
	8	-	-24.4	-
	16	-	-7.8	-

4.1.4 Bauschinger effect experiments

Bauschinger effect (BE) is of practical interest for processes which involve strain reversals such as fatigue cycling or plastic processing. Bauschinger experiments were conducted under compressive preloading to 1% of strain. The specimens are subsequently loaded in tension. Figure 4.7 shows the results for the one ECAE pass. For each direction three curves are plotted: forward tension (FT), forward compression (FC) and reverse tension (RT) for a specimen preloaded in compression to 1%. Besides the tension-compression asymmetry, this figure shows the effect of a compression prestrain in a subsequent reverse tension loading (FC/RT). For the remaining cases, a nondimensional Bauschinger parameter (BP) is used to compare the magnitude of the BE following the treatment in a previous study [84]:

$$BP = \frac{\sigma_b}{TotalWorkHardening} = \frac{\left(\sigma_f - \sigma_{rev}\right)}{2 \times \left(\sigma_f - \sigma_0\right)} \qquad (4.6)$$

where σ_0 is the initial yield strength of the material in FC, σ_b is the long-large back stress. One of the sources of the back stress is the dislocation pileups at the grain boundaries and substructures formed during ECAE. σ_0 is nondirectional because it opposes the flow in both forward and reverse loading. On the other hand, σ_b supports deformation in reverse loading. σ_f is the flow stress at the forward compressive strain of 1% and σ_{rev} is the onset of plastic deformation at reverse tension straining. BP was calculated for three different strain offset values: 0.05%, 0.1% and 0.2%. The evolution of BP for all these offsets was similar and thus only 0.01% is reported. Figure 4.8 presents BP as a function of the number of passes for the three directions. Each plot corresponds to a specific route. Interestingly, this figure shows the constant value of BP for the extrusion direction

regardless of the route nature and number of passes. BP steadily decreases along the two other directions for route A.

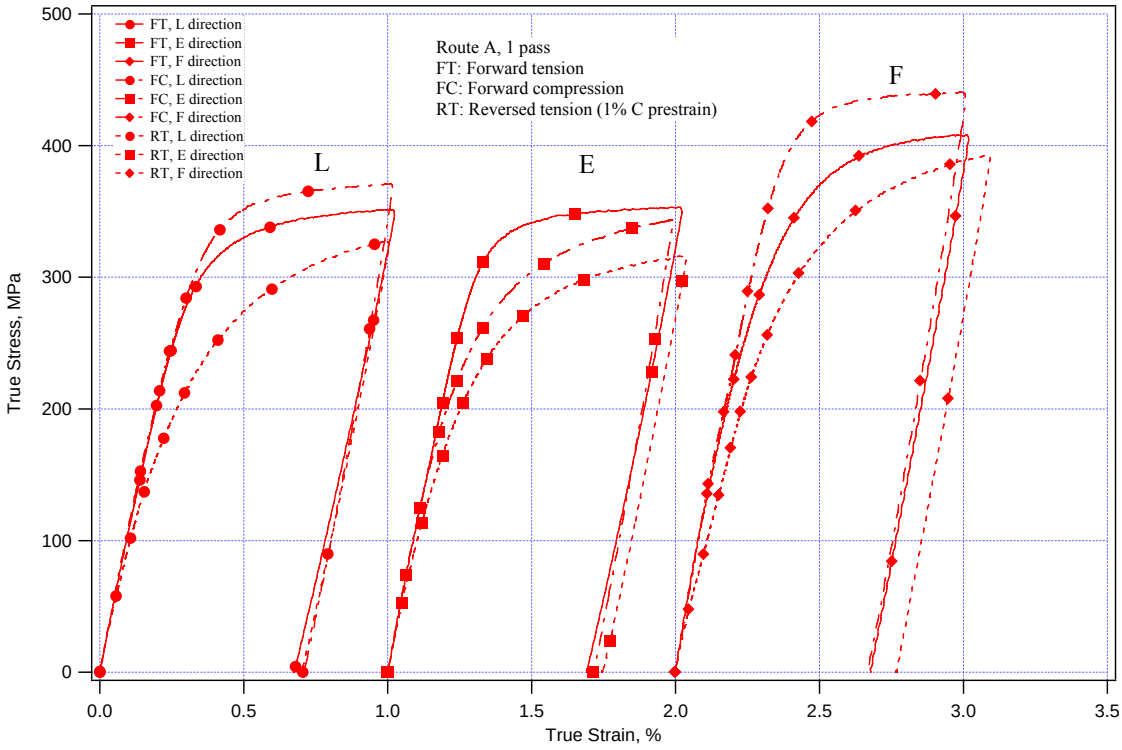

Figure 4.7: Forward tension and compression and reversed tension (1% compression prestrain) for case 1A for three directions.

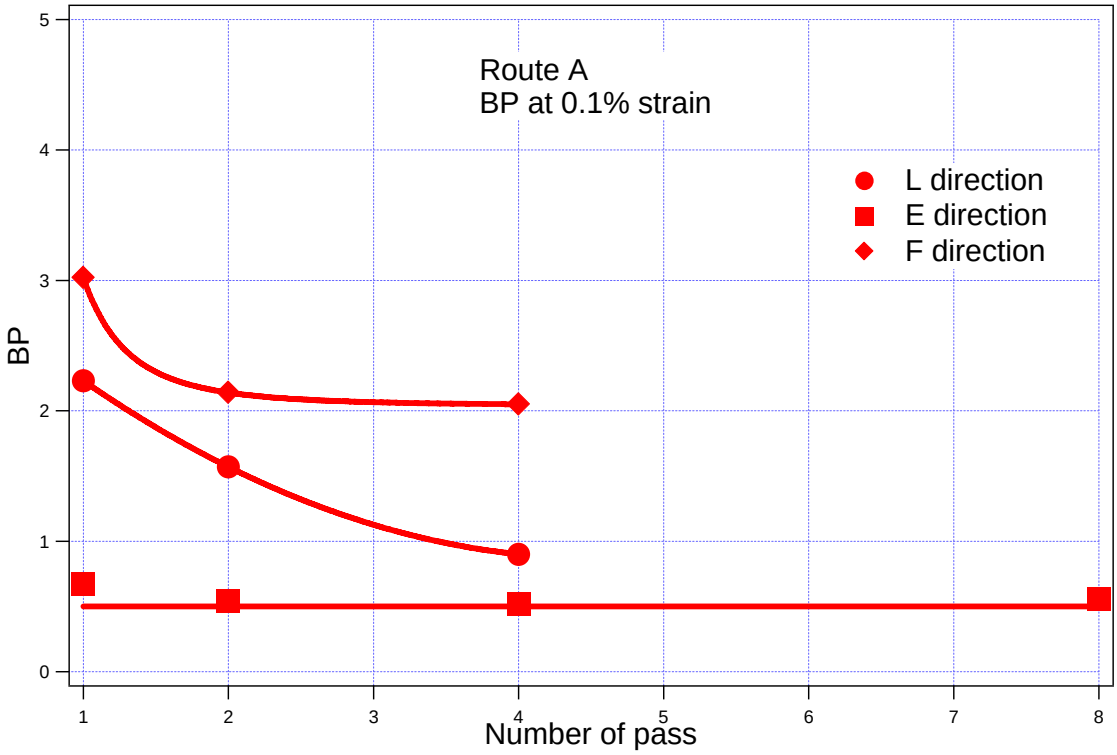

(a)

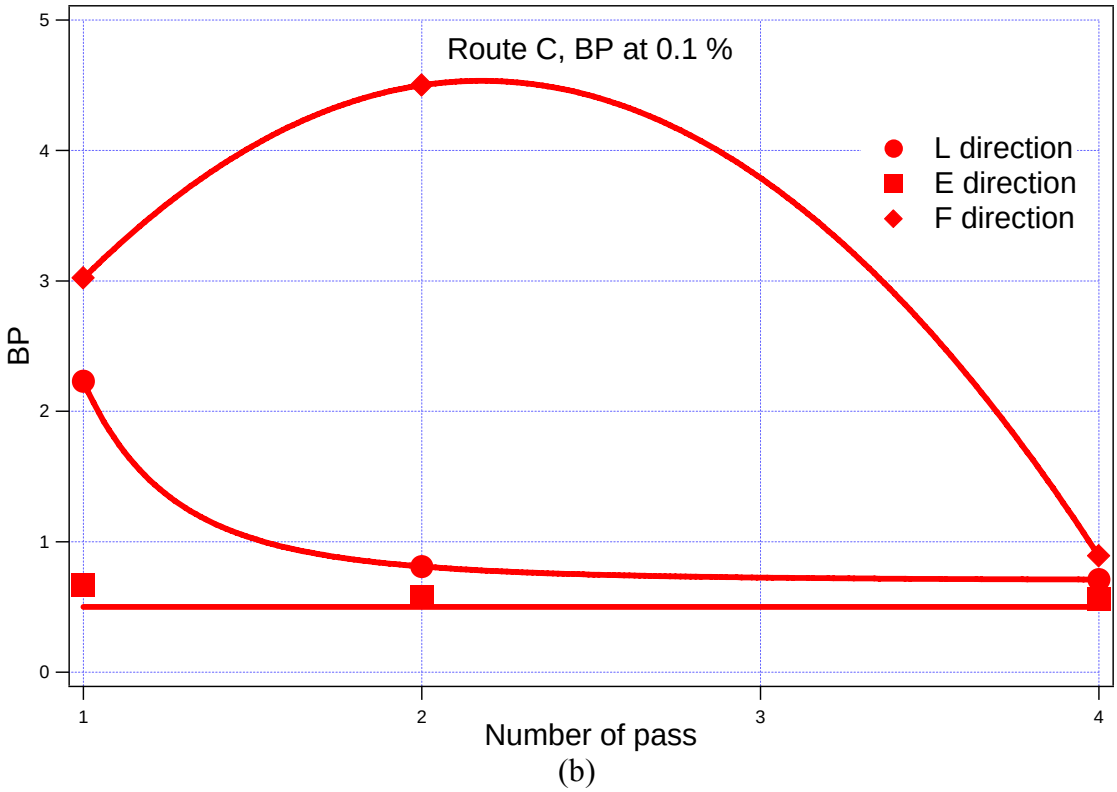

(b)

Figure 4.8: Evolution of Bauschinger effect with number of passes for (a): route A, (b): route C, (c): route E, (d): route B, and (e): route C'.

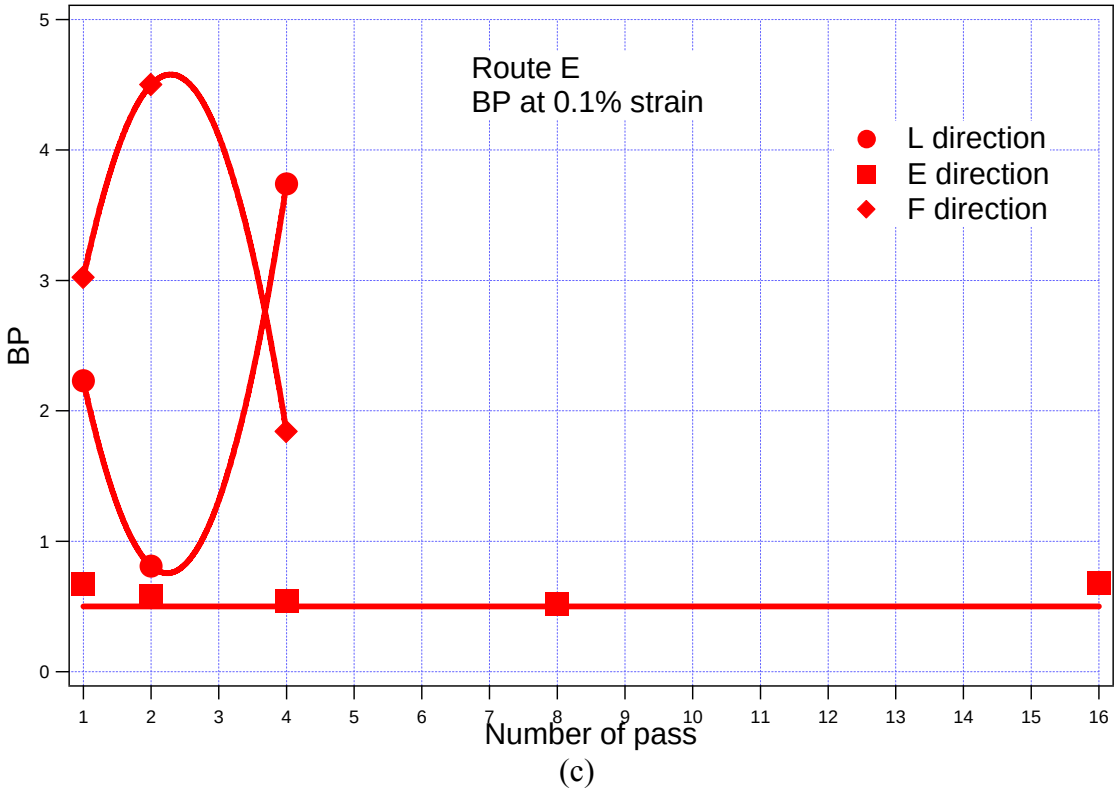

(c)

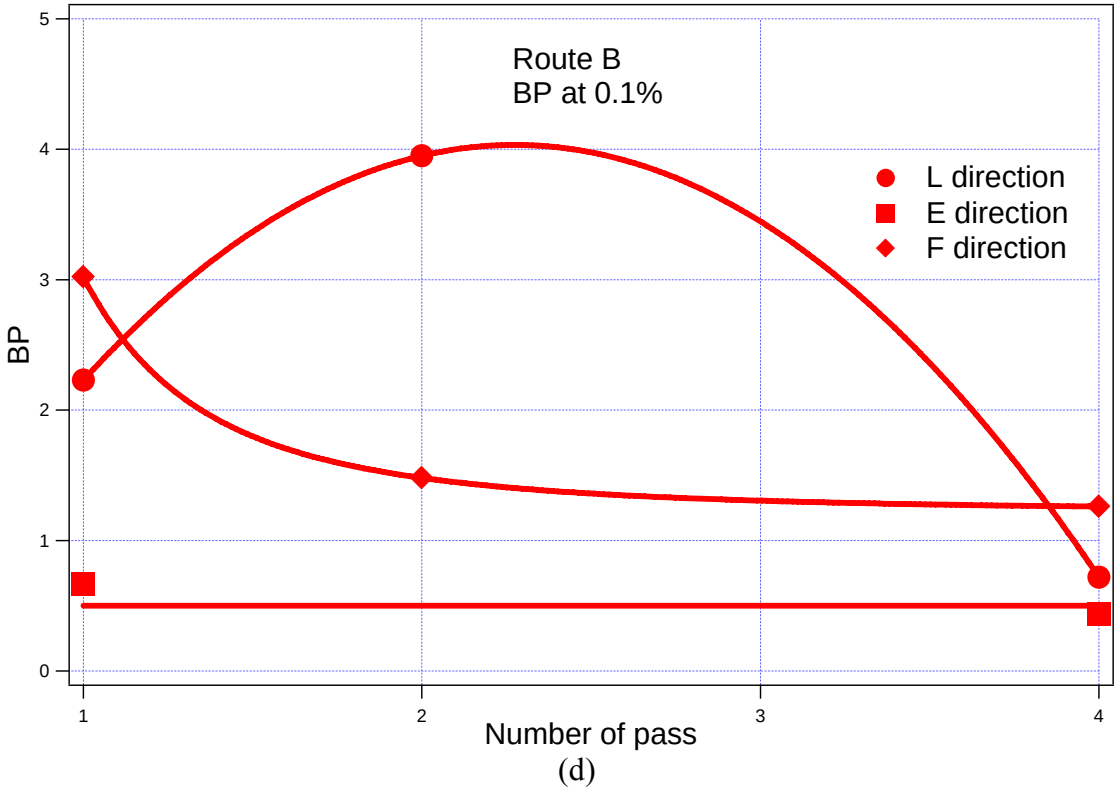

(d)

Figure 4.8 Continued.

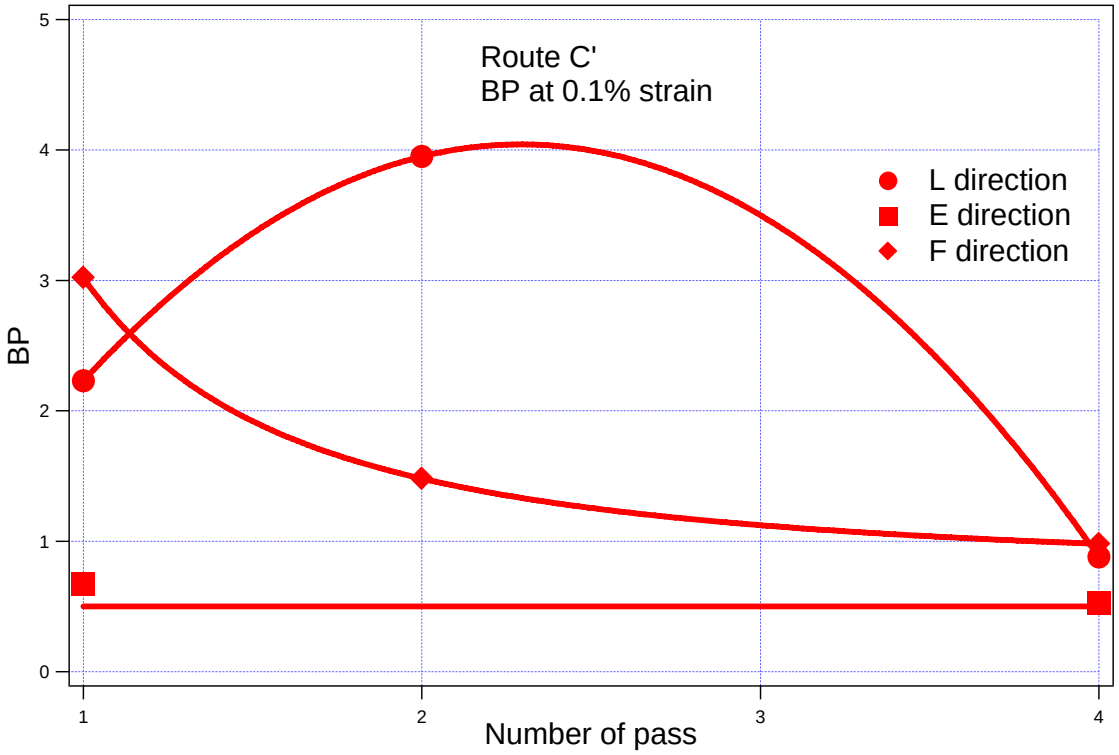

(e)

Figure 4.8 Continued.

4.2. Discussion

4.2.1. Evolution of strength and ductility

The tension results of the extruded bulk Cu yield interesting results. Severe plastic deformation of copper, unlike other mechanical processing methods such as rolling or drawing, tends to increase simultaneously the strength and the ductility with more applied strain. McFadden *et al.* [12], Valiev *et al.* [14] and Höppel and Valiev [15] attribute the increase in ductility to the refinement of the structure and to an increase in the fraction of high angle boundaries which results in the activation of boundary sliding and grain rotation deformation mechanisms. Several other researchers discussed the possibility of grain boundary moderated deformation mechanisms to rationalize the observed strength

and ductility increase in nanocrystalline materials [31,62,67]. However, Kumar *et al.*[31] critique this argument in their work on nanocrystalline nickel and argue that grain boundary sliding has not been shown with direct experimental evidence (the evidence given most of the time is the abnormal strain rate sensitivity) down to grain sizes less than 20 nm. In our TEM investigations of copper after several passes and different routes, we always observe a large scatter in the grain size. The average grain sizes are on the order of 300 to 500 nm (Figure 4.4), i.e. still significantly larger than nanometer range grain sizes. If grain boundary moderated mechanisms are the correct explanation for the ductility increase in nanocrystalline materials, then the present results are somewhat conflicting as grain boundary sliding or rotation is not expected at these relatively large grain sizes. Therefore, the rationale for the increase in both strength and ductility is the bimodal grain size distribution in bulk Cu instead of grain boundary moderated mechanisms. Figure 4.9 reports the evolution of the mechanical response in tension for specimens cut along the extrusion direction for different routes. Similar comparative figures for tension specimens tested along the two other flow and longitudinal directions are reported in the appendix. The simulataneous increase in strength and ductility is seen regardless of the considered route with a slight decrease in ductility at the first pass when compared to the annealed state. It has been well established that the strain imposed by the first ECAE passes exerts a strong effect on the fragmentation and refinement of the initial microstructure [85-86]. One can also see in Figure 4.9 that with increasing number of passes, the strain range in which strain hardening is observed increases. According to recent studies [26,61,63] this increase is due to the formation of a small amount of recrystallized grains and dislocation activity in these grains. Moreover, in the present

study, the simultaneous increase in strength and ductility is shown to exist even at the early stages of ECAE deformation with limited numbers of passes (4) as compared to the same strength and ductility levels achieved after 16 passes in the study by Höppel and Valiev [15]. It is also evident when different routes are compared that a combined effect of crystallographic texture with other metallographic features should be taken into account to expain the anisotropy of mechanical properties. The grain shape and morphology manifestly affect the mechanical properties such as yield strength as will be seen in the next paragraph and ductility at a lesser degree through strain localization, which is particularly significant in materials having a higher fraction of low angle boundaries. The fine lamellar structure with a higher fraction of high angle boundaries produced by route A results in slightly beneficial tensile ductility.

SEM investigations of the fracture surface for 2C and 4C specimens tested along the extrusion direction shows the ductile character of the material. A substancial necking occurs before the breaking of the specimens as shown in Figures 4.10.a and 4.11.a. This is corroborated by a direct view of the fracture surface at low magnification (Figures 4.10.b, and 4.11.b) which shows the reduced small section where the fracture occured after necking. A brittle fracture would have been translated by a rectangular fracture surface keeping almost the same dimension of the initial cross section. The “cup-and-cone” fracture of Figures 4.10.c and D.c is also an indication of the ductile fracture which occurs by a process of void coalescence. Coalescence occurs by elongation of the voids and elongation of the bridges of material between the voids. This leads to the deformation of elongated “dimples” and holes separated by thin walls.

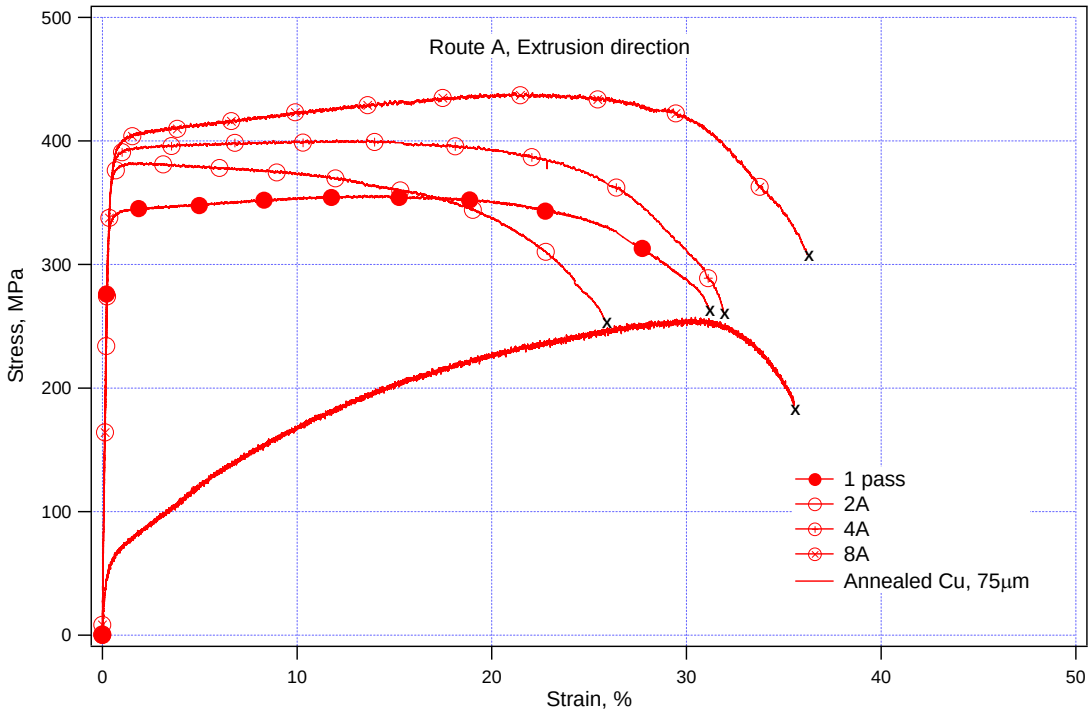

(a)

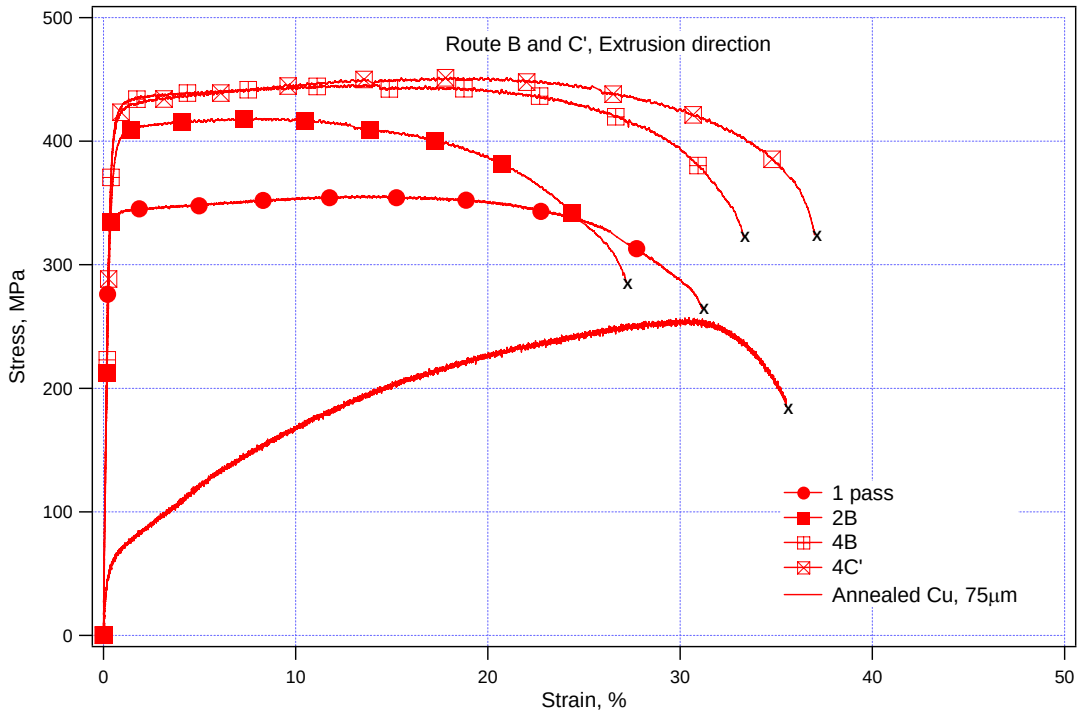

(b)

Figure 4.9: Mechanical response in tension of ECAE processed bulk Cu specimens cut along the extrusion direction for, (a): Route A, (b): Route B and C', (c): Route C, and (d): Route E.

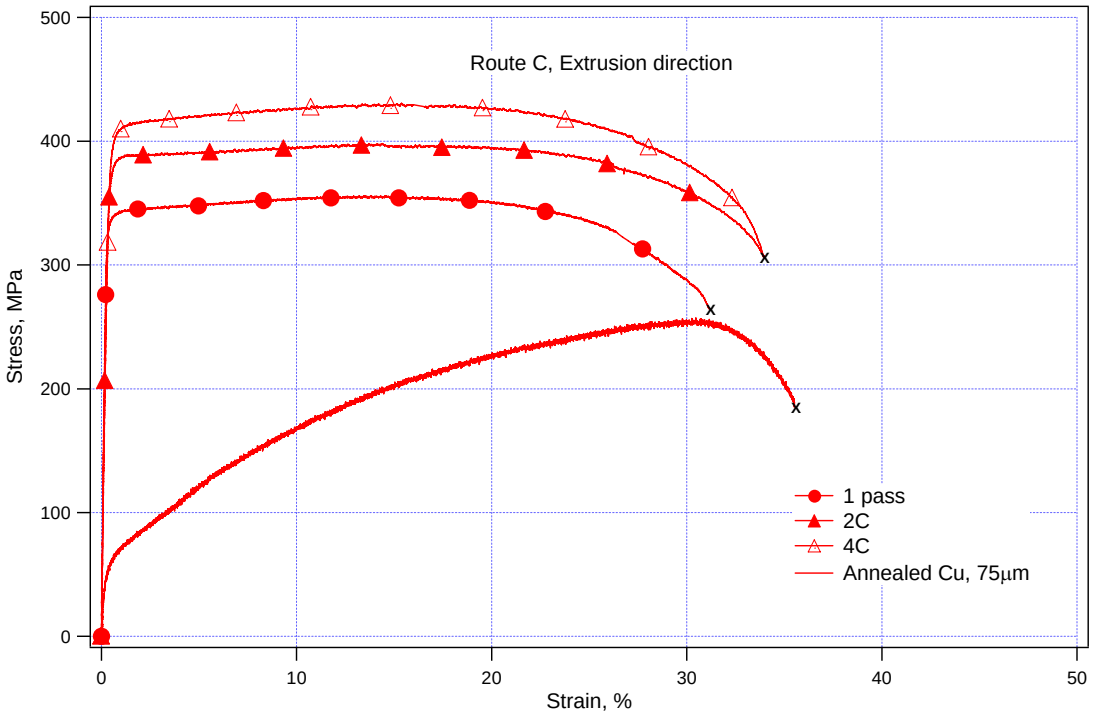

(c)

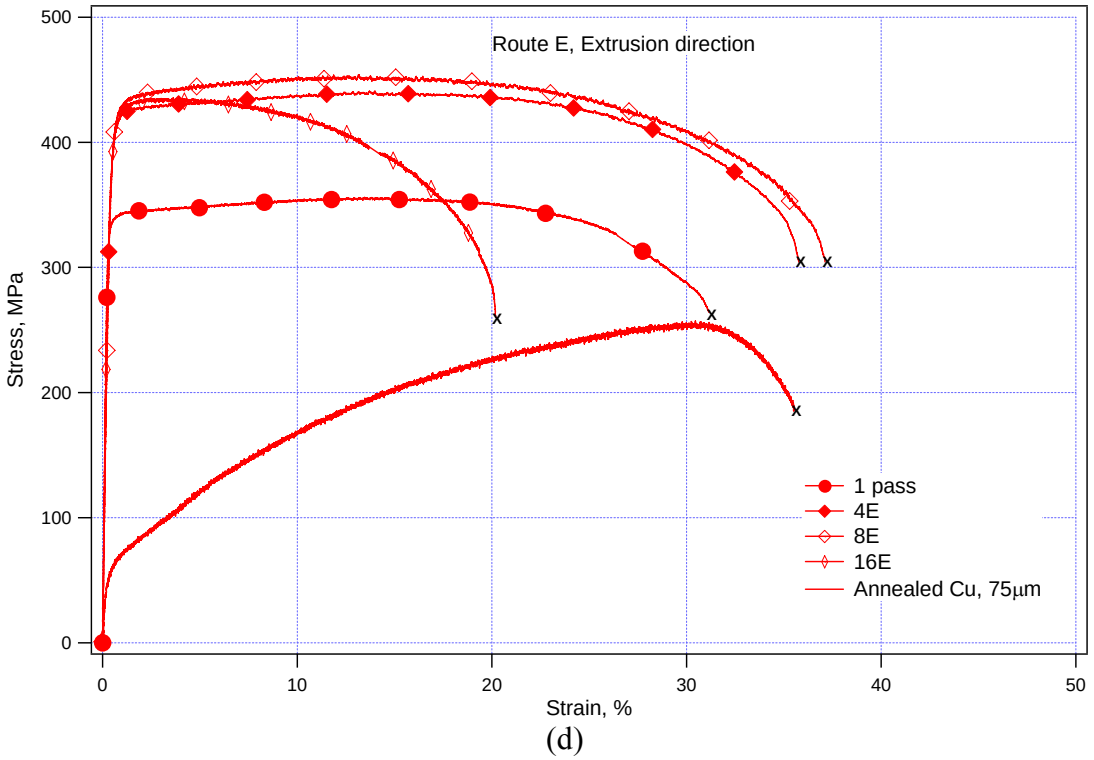

(d)

Figure 4.9 Continued.

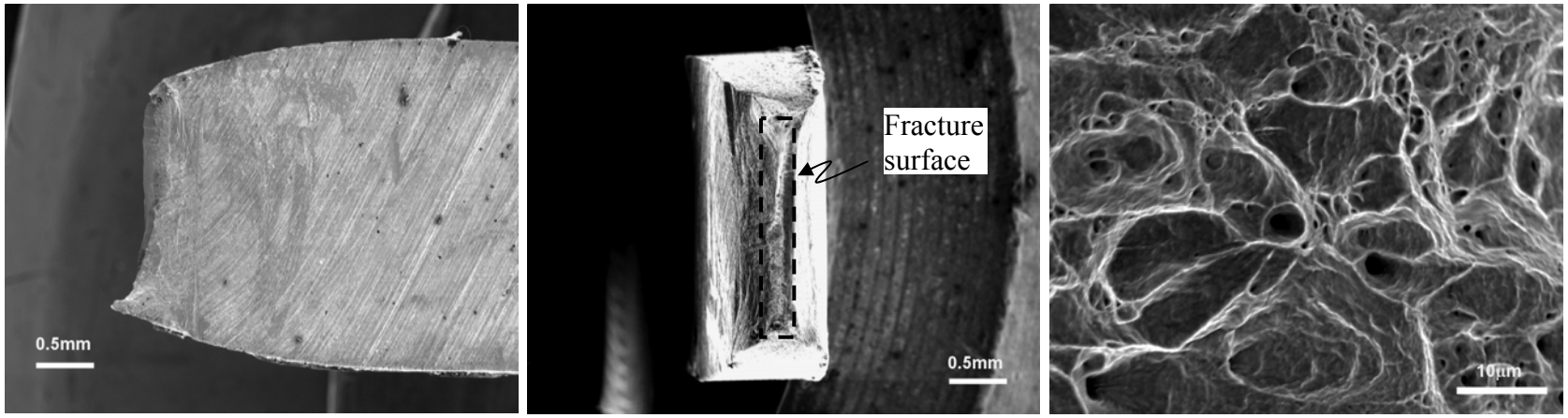

(a) (b) (c)

Figure 4.10: Fracture surface of tension specimen from route 2C tested along the extrusion direction.

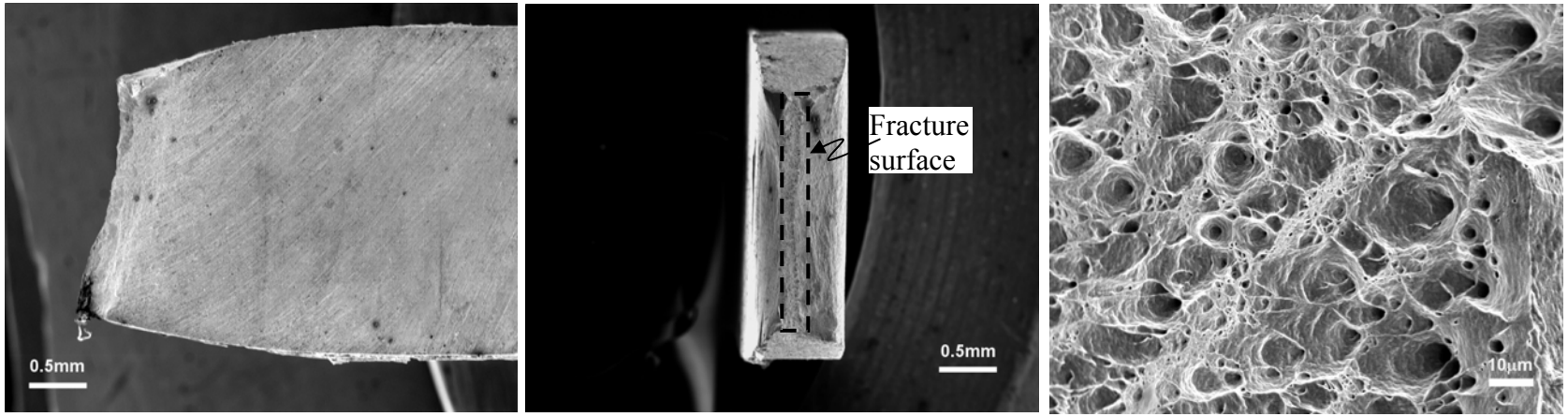

(a) (b) (c)

Figure 4.11: Fracture surface of tension specimen from route 4C tested along the extrusion direction.

4.2.2. The effect of Strain path on the yield anisotropy

The mechanical anisotropy exhibited by plastically deformed materials is controlled by three scales: a macroscopic level of texture, a mesoscopic level of size and morphology of grains, and a microscopic level of slip system activity and their interaction with other microstructural features such as grain boundaries. In recent years, severe plastic deformation (SPD) processes such as ECAE have been studied to further the concept of grain boundary engineering in which the grain boundaries are tailored to specific applications [87]. After one ECAE pass, the microstructure consists of elongated grains with low angles of misorientation which evolve with subsequent passes to ultrafine grains separated by high angle boundaries [88-89]. The control of grain boundaries would permit the control of the strength of the material with fine grains through the distribution of high angle boundaries (HAB), and low angle boundaries (LAB) [90-91] through an independent contribution of each type:

$$\sigma_0 = \sigma_{LAB} + \sigma_{HAB} \qquad (4.7)$$

where σ_0 is the friction stress. This variation of Hall Petch relation accounts for the additional strengthening effect of grain boundaries. Cell boundaries and subgrain boundaries are not completely impenetrable by dislocations and therefore an ECAE processing route which produces an array of high angle boundary grains would yield a priori higher yield strength. This rationale is contradicted by yield strength values for the longitudinal direction. The reversal strain for route C at the second pass creates a microstructure with a high ratio of low angle boundaries [92] and yet the yield strength experiences an increase between the 1st and 2nd pass while it drops for routes A and B in which the microstructure consists of more grains with high angle boundaries. Therefore,

factors other than grain boundaries seem to have more influence on the yielding anisotropy in ECAE processed Cu.

Routes A and C have the same major texture components [46], but the mechanical behavior for both cases is quite different as the yield strength drops continuously with number of passes for the longitudinal direction in route A (Figure 4.6.a). The texture effect can be quantified by considering the resolved shear stress instead of yield or ultimate strength values. Using the previously measured texture for routes A, B, C and E at four passes, Taylor factors are calculated to normalize the strength values and account for the texture effect. The prediction and measurements of texture in ECAE processed fcc materials [46,93-94] show that for a specific route, predominant texture components are kept the same with number of passes while the intensity changes slightly. Consequently, it is safe to consider the same 4A, 4C, and 4B textures for corresponding cases with less number of passes (1A and 2A, 2C, and 2B). Texture of ECAE processed Cu is not strong and yields small differences in Taylor factors for different directions (Table 4.5) which cannot explain the anisotropy in yield strengths as the resolved shear stress values are not similar for different directions (Table 4.6).

Table 4.5 Taylor factor values calculated from the measured texture in the 4^{th} pass for different routes and directions.

ECAE route	Longitudinal direction	Extrusion direction	Flow direction
A	2.778	2.772	2.927
B	2.722	2.732	2.816
C	2.779	2.762	2.863
E	2.774	2.777	2.835

Table 4.6 Yield and resolved shear stresses for routes A, B, and C for three different directions.

		Yield Stress σ_y (MPa)			Resolved Shear Stress τ (MPa)		
Route	# of passes	L Dir	E Dir	F Dir	L Dir	E Dir	F Dir
A	1	312±9	337±1	355±5	112±3	122±0	121±1
	2	286±5	369±3	450±3	103±2	133±1	154±1
	4	276±0	375±1	445±5	99±0	135±0	152±2
	8	-	377±2	-	-	136±1	-
B	2	292±5	390±8	410±2	107±2	143±3	147±1
	4	278±5	403±4	379±1	102±2	148±1	135±0
C	2	353±3	384±9	374±4	127±1	139±3	130±1
	4	302±1	396±4	435±0	109±0	143±1	152±0
C’	4	295±1	406±5	391±1	-	-	-
E	4	303±7	402±5	406±4	109±2	145±2	143±1
	8	-	405±2	-	-	146±1	-
	16	-	387	-	-	140	-

Grain morphology plays then a major role in the anisotropy of ECAE processed Cu. The morphology and size of grains as well as their orientations with respect to specimen orientations need to be considered while assessing the anisotropy of ECAE processed Cu for different routes. One would expect a rapid grain refinement for the initial number of passes (up to the 4^{th} pass) to reach eventually a stable final grain size in the higher number of passes. That would be translated into an increase of yield strength regardless of the nature of route for the initial passes to reach eventually a certain strength plateau. Considering each direction independently, the evolution of yield strength as a function of the number of passes as shown in Figure 4.6 obeys the previous statement for higher number of passes in cases where the higher number of passes were conducted (route A up to 8 pass and E up to 16 pass). The slight yield strength drop for the 16^{th} pass in route E can be attributed to dynamic recovery triggered by the high stored deformation energy resulting from the high strain levels applied.

It is interesting to note that the steady increase in yield strength which is more pronounced for less number of passes (up to the 4th pass) is not always observed. With the exception of route C (and consequently, route E for the second pass), yield strength values along the longitudinal direction decrease with the number of passes. For routes B and C' where the billet is subjected to 90º rotation after each pass, σ_y values decrease even between the 2nd and 4th pass along the flow direction. The decrease in yield strength with the number of passes for route A along the L direction is an eloquent example of the grain morphology effect. Figure 4.2 shows a schematic of the grain orientation and morphology for the first and second passes for route A subjected to tension in the L direction. The figure also shows the most favorable {111} slip planes corresponding to the measured major texture component, [313], along the L direction in route A.

According to this schematic, the dislocation mean free path defined as the length of the intersection segment between the slip and flow planes and bounded by the grain boundaries increases with number of passes. This configuration favors an easier movement of dislocations with higher number of passes as they can move for a longer distance before reaching a grain boundary in their path and being stopped or annihilated. The change of inclination angle φ_n is higher between the first and second passes, consequently the increase of dislocation mean free path is more important which explains the significant decrease of σ_y. Between the second and fourth pass, the decrease of σ_y is less pronounced as the change in grain inclination is smaller and also because the dislocation mean free path increase is compensated by the grain refinement.

For route B, the same decrease in σ_y is observed for the L direction and can be rationalized similarly by the change in the dislocation mean free path, even though the

billet is rotated ±90° after each pass. The projection of grains in the flow plane which constitutes the flat surface of the specimen cut with respect to the L direction is stretched further after each pass and the inclination φ_n with respect to extrusion direction is lowered (Figures 4.1.d and f) increasing therefore the mean free path of dislocations. For route C', Figure 4.1.a suggests that after 4 passes the material should retain the same morphology of grains but in reality, refinement and creation of an equiaxed microstructure occurs at the 4th pass as an irreversible splitting is unavoidable after the evolution of a microstructure dominated by low angle boundaries to near equilibrium equiaxed microstructure [89]. The drop of yield strength for route C' between the 1st and 4th pass is insignificant and lies almost within the error interval. For this route, there is a competition between grain refinement and arguably a "memory" effects from the previous passes. Indeed, a material may prefer to deform along previously established shear planes due to the interaction of old walls with new dislocation directions during strain path change [95]. This "memory" effect is more important with increasing number of passes. Indeed, for route C where the strain is reversed in the 2nd pass the reduction of grain size overcomes the processing history effect of the material and causes an increase in σ_y up to the 2nd pass and then drops again in the 4th pass due apparently to the retained memory of the material microstructure during the odd passes.

Consideration of grain morphology evolution can also shed some light into the differences in σ_y along different directions for specific route and number of passes. For all cases, regardless of the route and number of passes, flow stresses for the flow and extrusion directions are higher than those for the L direction. The reason behind this constant trend is the fact that tension specimens for the L direction were cut from the

flow plane where the sheared grains are favorably oriented to deform in tension as shown in Figures 4.1 and 4.2.

For the E and F directions, there is an increase of the yield strength between the 1st and 2nd passes regardless of the route which can be explained by the reduction in grain size. Between the 2nd and 4th passes, the strength values do not change significantly for route A. It is also worth mentioning that the order of directions in terms of flow stresses does not change with the number of passes for this route, i.e. the F direction is the strongest while the L direction experiences the earliest yield. This trend is intimately related to the fact that the orientation of the billet is kept the same after each pass for route A. The higher σ_y values along the flow direction as compared to that along the E direction can be explained by the morphology effect. Tension specimens for both E and F directions were cut from the longitudinal plane. The difference is that, for the E direction, the thickness plane of the specimen is the flow plane where the grains are stretched in the extrusion direction and are favorable to deformation for the same reasons mentioned above, whereas for the F direction, the thickness plane is the transverse plane where sheared grains are oriented perpendicular to the tension direction.

For route B, the situation is more complex. First, we can observe that between the 1st and 2nd passes, the increase in strength for the F direction is less pronounced than that for route A. In fact, the slope increase in σ_y along the F and E directions is the same and the difference between the two directions can be attributed solely to texture as the resolved shear stresses are the same for both directions (Table 4.6). However, the yield strength for the E direction exceeds that along the F direction in the 4th pass. Unlike route A, the longitudinal plane for route B (Figure 4.1.d, and f) is formed essentially of

elongated grains with an inclination with respect to the extrusion direction decreasing with the number of passes. That creates a condition where the sheared grains are favorably oriented to deform when tested along the flow direction. The evolution of yield strength values for route C' are similar to route B. Although one would expect a different outcome because of the uniform microstructure expected in this route in the 4th pass, the response of the material is controlled mainly by the competing effects of processing history of the material in the previous passes and grain refinement.

4.2.3. Tension-compression asymmetry and Bauschinger effect

The Stress differential (SD) values confirm the tension-compression (TC) asymmetry encountered in UFG materials. This asymmetry has been found in UFG Aluminum and iron alloys [54-55]. Iron alloys were stronger in compression and the asymmetry was attributed to a hydrostatic pressure effect on yielding in ultrafine grained materials. This explanation was motivated by the similarities between UFG materials and amorphous materials which are sensitive to hydrostatic pressure. Table 4.4 shows that the stress differential ratio is not always positive and interestingly the tension specimen is always stronger when cut in the extrusion direction. Therefore an additional factor must be affecting the asymmetry as the stronger tensile response cannot be explained considering the hydrostatic pressure. At least for fcc materials, we can rule out the effect of texture on T/C asymmetry which is a function of the route to explain the consistent negative values of the SD ratios.

It is worth noting that, the absolute values of the SD ratios increase along the extrusion direction with the number of passes in route A. This increase seems to be directly related to grain morphology. During plastic deformation, the developed

microstructure plays an important role in the mechanical behavior. For the ECAE processed Cu, the grains are stretched along the extrusion direction. The aspect ratio of the grain increases with number of passes. Cell block boundaries with high angle of misorientation form in the material parallel to the most active slip plane providing a good barrier to dislocation mobility [96-97]. The ECAE process subjects the material to heavy shearing and consequently to the multiplication of dislocations which migrate along the slip lines and stop at the grain boundaries as shown in the schematic of Figure 4.2 (A different slip lines family is activated when the material is sheared along the extrusion direction, but in order to avoid encumbering the schematic only one slip line family is depicted as the concept of dislocation mobility towards the grain boundaries is intended for description and it is not hampered by the choice of the slip lines). Dislocations possess a mechanical sign associated with the burgers vector, an excess of mobile dislocations of one sign is blocked at one side of the grain boundary, and the opposite sign at the other side of the grain boundary creating a polarity [98] as shown in Figure 4.2. A reversal strain of compression in the same direction as the one which created the accumulation of these dislocations, i.e. the extrusion direction, will relieve the asymmetry of slip resistance caused by the dislocation polarity and the flow stress needed to yield the material will be therefore smaller.

This mechanism is similar to the Bauschinger effect and is translated here to a tension-compression asymmetry in virgin specimens without any prior prestrain because of the heavy processing incumbent to the ECAE process. To corroborate this explanation, supplementary specimens were tested which were cut parallel to the shear plane for the 4A case (at 7.1°from the longitudinal plane). This plane possesses the highest grain

aspect ratio and as a result, experienced the smallest SD value (Δ=-33.5% for $\sigma_y^c = 283MPa$ and $\sigma_y^t = 397MPa$). This value is even smaller than the 8A case for the extrusion direction (Δ=-29.1%). The reason behind observing soft compression for only the extrusion direction is closely connected to the morphology of the grains exhibiting an elongated shape along the extrusion direction grain which provides a longer boundary for stopping dislocation during processing, and to a lesser extent to the processing history of the routes for which the final microstructure is more equiaxed.

A softer compressive response was also observed for route C along the longitudinal direction when the billet was subjected to two passes. The rotation of the billet at the second pass creates a corrugated microstructure. The grains are elongated at the first extrusion pass, and upon the reversal strain in the second pass following route C, some of the grains are reoriented back to the initial position while keeping the irreversible elongation suffered at the first pass. The second pass results consequently in "tilting" some grains to the longitudinal direction as shown in the TEM micrograph of Figures 4.12.a, b, and c. The same micrograph shows the accumulation of dislocations at the grain boundaries oriented along the longitudinal direction. The same argument of polarization of grain boundaries can be then advanced to explain the T/C asymmetry in favor of compression.

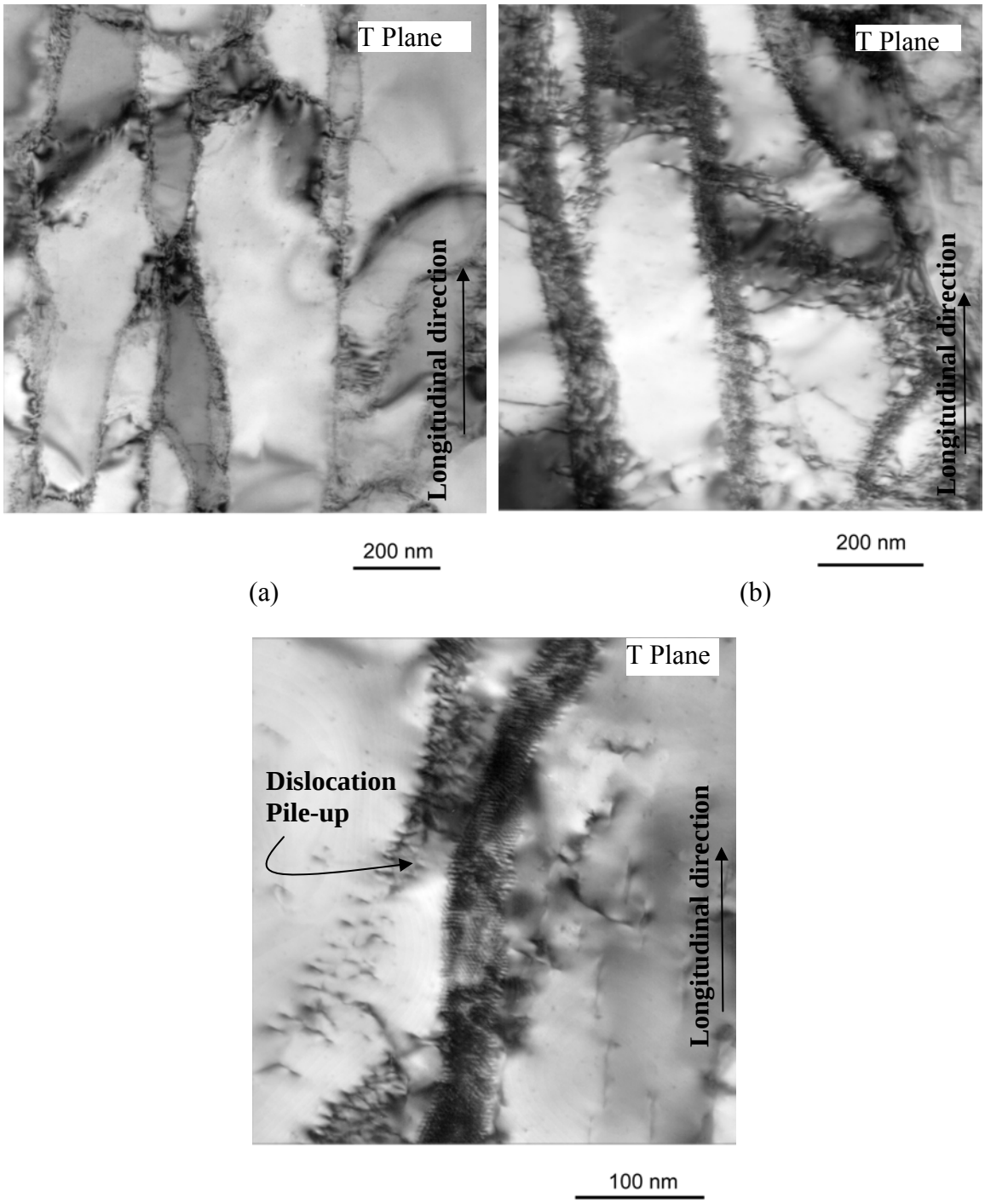

Figure 4.12 TEM micrographs in the transverse plane of ECAE processed Cu via route 2C. (a) elongation of the grains along the longitudinal direction and (b) accumulation of dislocations along the vertical boundaries. (c): pile-up of dislocation blocked by the vertical grain boundary oriented along the longitudinal direction.

Figure 4.8 shows that the BP is kept relatively constant along the extrusion direction regardless of the number of passes or the nature of the route. The value of BP around 0.5 implies that $\sigma_{rev} \approx \sigma_0$. This is a direct result of the T/C asymmetry with higher values of strength in tension when a specimen is tested in the extrusion direction. As mentioned earlier, the dislocation polarity created at the adjacent grain boundaries during heavy processing is relieved during a reverse strain as in compression causing the dislocations to annihilate at the interior of the cell blocks. An additional increase in reverse strain in compression will permit an inverse in the polarity, but seemingly a compression prestrain of 1% is enough only to eliminate the existing polarity leading the material to keep the same yield strength at the following tensile test because of lack of back stress. Again, route A shows a steady evolution of another comparative parameter as BP decreases steadily for the L and F directions with the number of passes.

Pedersen *et al* [99] showed that the flow stress in a composite model is entirely due to the resistance of dislocation motion in the tangles of forest dislocation rather than to the assistance of pile up dislocation developed in the forward loading. In their composite model, dislocation tangles act as hard but deformable barriers in a relatively soft matrix. This finding is supported by our experimental results for route 2C along the flow direction which experiences the highest Bauschinger effect (BP= 4.5) as the microstructure for route 2C has a high ratio of subgrain boundaries and a high density of internal dislocations. Therefore, it is important to note that BP can be used as an indicator of the nature of the microstructure and the ratio of low angle to high angle misorientation grain boundaries. The steady decrease of BP for route A for all routes confirms that the microstructure tends to reach an equilibrium by an increase of high angle misorientation

grain boundaries. The same thing can be observed for routes B, C, and C' at the fourth pass while a high density of dislocations and the fraction of low angle misorientation grain boundaries should still exist for route E at the fourth pass because of the increase of BP for flow direction. This delay of reaching an equilibrium in route E can be explained by the hybrid nature of the route where both 180º and 90º are involved.

CHAPTER V

MICROSTRUCTURE EVOLUTION AND MECHANICAL BEHAVIOR OF COPPER OBTAINED BY CONSOLIDATION OF MICRO AND NANO POWDERS USING EQUAL CHANNEL ANGULAR EXTRUSION

The consolidation of micro and nano copper particles (325 mesh, 130 nm, and 100 nm) was performed using room temperature equal channel angular extrusion (ECAE). The effects of extrusion route, number of passes and extrusion rate on consolidation performance were evaluated. The evolution of the microstructure and the mechanical behavior of the consolidates were investigated and related to the processing route. Possible deformation mechanisms are proposed and compared to those in ECAE processed bulk Cu. Combined high ultimate tensile stress (470 MPa) and ductility (~20% tensile fracture strain) with near elasto-plastic behavior was observed in consolidated 325 mesh Cu powder. Near-perfect elastoplasticity in consolidated 325 mesh Cu powder is explained by a combined effect of strain hardening accommodated by large grains in the bimodal structure and softening caused by recovery mechanisms. Tensile strengths as high as 790 MPa and fracture strain of 7.3 % were achieved for consolidated 130nm copper powder. Compressive strengths as high as 760 MPa were achieved in consolidated 130 nm copper powder. The present study shows that ECAE consolidation of nanoparticles opens a new possibility for the study of mechanical behavior of bulk nanocrystalline materials as well as offering a new class of bulk materials for practical engineering applications.

5.1. Experimental results

5.1.1. Stage I: powder compaction by manual tapping

5.1.1.1. Initial powder and initial processing runs

The copper powders were characterized prior to processing to determine their size and morphology. Figure 5.1.a shows that the size of microcrystalline Cu powder ranges from approximately 1 to 10 μm. Figure 5.1.b is an SEM micrograph of the 130 nm powder agglomerates. The irregularity (Figure 5.1.c) of the agglomerate surface shows that they are composed of clusters of fine particles driven together to minimize surface energy. TEM images (Figure 5.1.d) indeed show the actual morphology and size of the powder: most particles are about 100-130 nm and they have spherical morphology. By comparison, X-ray analyses yielded values of 4.2 μm and 130 nm as grain sizes for the 325 mesh and 130 nm powders.

The first set of the Ni and AISI 1018 steel cans was filled (cases 1 to 8 in Table 3.4) with 100 nm Cu powder in air. The extrusion runs of this powder were used to modify the processing parameters in order to find a suitable extrusion route that would later permit full densification of cleaner powder. A 50 mm long powder chamber with a diameter of 13 mm in nickel cans did not yield enough material for mechanical characterization due to the high level of compaction after the first ECAE pass. AISI 1018 steel and nickel cans, with a larger powder space (20 mm in diameter, 100 mm powder chamber length), were then used for the remaining extrusions. The 1018 steel cans were less ductile and difficult to extrude. The presence of cracks in the can after the first pass lessened the possibility of successful subsequent extrusions. The final density of specimens from steel cans was therefore low in some cases (Table 5.1) (the definition of

case # was reported previously in chapter III in Table 3.4). Vickers hardness measurements are also reported in Table 5.1 from these extrusion runs. A higher extrusion speed (25 mm/sec, case 6) led to poor consolidation as the final density was 71% of the full density. However, the density values for a lower extrusion speed (2.5 mm/sec) were similar to or better than those reported in previous works [18,24,100]. These preliminary experiments showed the importance of the choice of the canning material and geometrical dimensions of the internal chamber, and the effect of extrusion rate needed for an acceptable consolidation. Nickel was chosen to be the best canning material for the consolidation of nano copper powders.

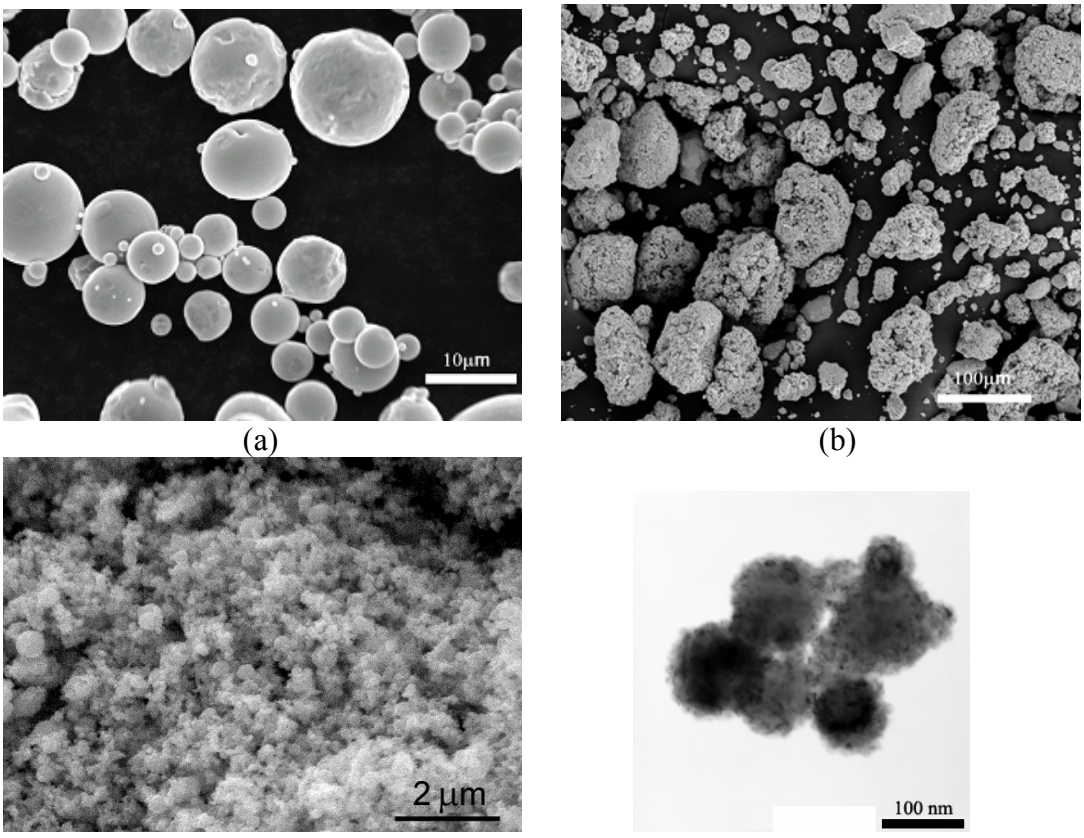

(a) (b)

(c) (d)

Figure 5.1 SEM images of (a) 325 mesh Cu powder, (b) agglomerates 130 nm Cu particles, (c) the close up of an agglomerate in (b) and (d) a bright field TEM image of the 130 nm Cu powder.

Table 5.1 Summary of the experimental conditions used for the consolidation of micron and nanometer size copper particles and severe deformation of coarse grained copper using ECAE. For details on the nomenclature used in ECAE processing see [17,37-38,40].

A: ECAE processed bulk Cu via route 4C.
B: ECAE processed Cu via route 2C annealed at 600C, with an average grain size of 75μm.

Case #	Average			Stdev			density (g/cm3)	(%)
	L (GPa)	T (GPa)	F (GPa)	L (%)	T (%)	F (%)		
1	1.78	1.84	1.79	4.9	3.2	8.4	8.81	98.7
2	1.96	2	1.95	6.7	6.2	5.6	8.85	99.1
3	1.87	2.03	2	6.5	1.4	3.3	7.96	89.2
4	NA	NA	NA	NA	NA	NA	8.54	95.6
5	_	2.03	_	_	5.1	_	8.33	93.3
6	NA	NA	NA	NA	NA	NA	6.34	71.0
7	1.75	1.9	1.81	8.1	4.5	7.2	8.16	91.4
8	2.03	1.96	2.01	10.5	10.0	13.1	8.82	98.7
A	_	_	1.20	_	_	3.09	8.93	100.0
B	0.5			1.7			8.93	100.0

5.1.1.2. Optical microscopy

A cross section of consolidated 130 nm Cu powder following route 4E was cut parallel to the transverse plane (perpendicular to the extrusion direction) and prepared for a metallographic investigation. Figure 5.2 shows the scanned cross section. We can distinguish some different flow lines separating regions reflecting different level of hue which seemingly correspond to areas having dissimilar microstructures. One can assume a priori that these regions are formed with “grains” of different sizes, shapes and orientations. Optical micrographs have been taken from different areas of this section to build a qualitative understanding of the powder behavior during the extrusion process.

Figure 5.2 Scanned cross section parallel to the transverse plane of consolidated 130 nm Cu powder following route 4E. This section was previously polished and etched.

Figure 5.3 shows a low magnification micrograph of the consolidate. Figure 5.3.a illustrates the elongation along some flow lines of the agglomerates under which nanocrystalline powders cluster. These flow lines do not seem to follow a specific direction but rather organize into blocks of uniform structure. These blocks seem to flow with respect to each other during the extrusion and can be separated by a fine separation line or interface as shown in Figure 5.3.a or by a thicker transition zone as illustrated in Figure 5.3.b. These areas are generally continuous, but in some instances can be preferable site of discontinuity where porosity emerges as indicated with the arrow in Figure 5.3.b. Other optical micrographs at higher magnification are added into the appendix to show these transition zones where non uniformity of flow exists. Figure 5.3.a and b show a separation between two regions with similar characteristics, but there are

some cases where we can observe three regions or more forming a triple zone at their intersection (Figure 5.3.c). The intersection area is often a strong candidate for the existence of remnant porosity.

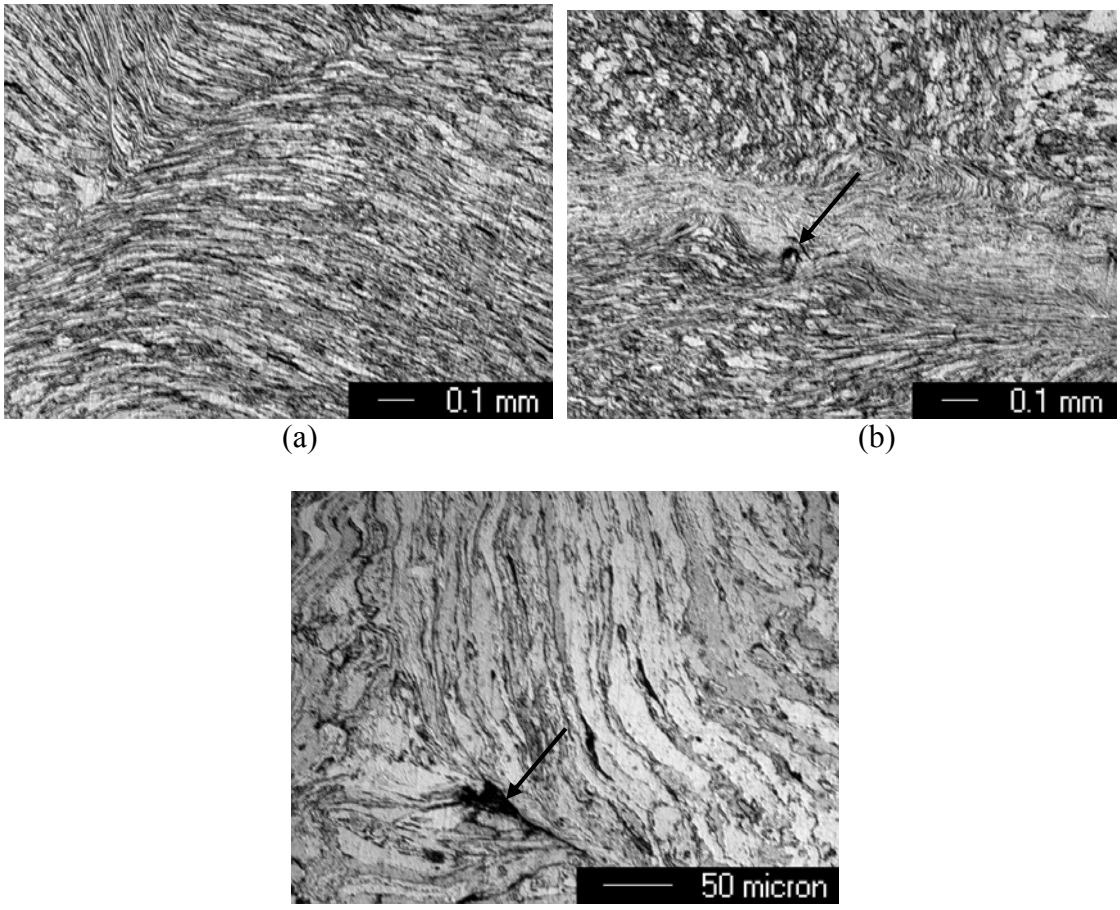

(a) (b)

(c)

Figure 5.3 Low magnification optical micrographs of consolidated 130 nm Cu powder illustrating the flow lines formed by the elongation of powder agglomerates during extrusion.

Higher magnification micrographs show that debonding may even occur between agglomerates oriented in the same direction (Figure 5.4.a). It can be assumed that route E contributes to opening the gap between distinct agglomerate during the 180º rotation at the second pass. These agglomerates disintegrate to a certain extent as illustrated by the

small “grains” in Figure 5.4.b, but a considerable proportion is reticent to a break down even after subjecting the can to four passes. Figures 5.4.c and d show a fairly large agglomerate conveniently etched and revealing the very fine structure corresponding to the nanocrystalline particles.

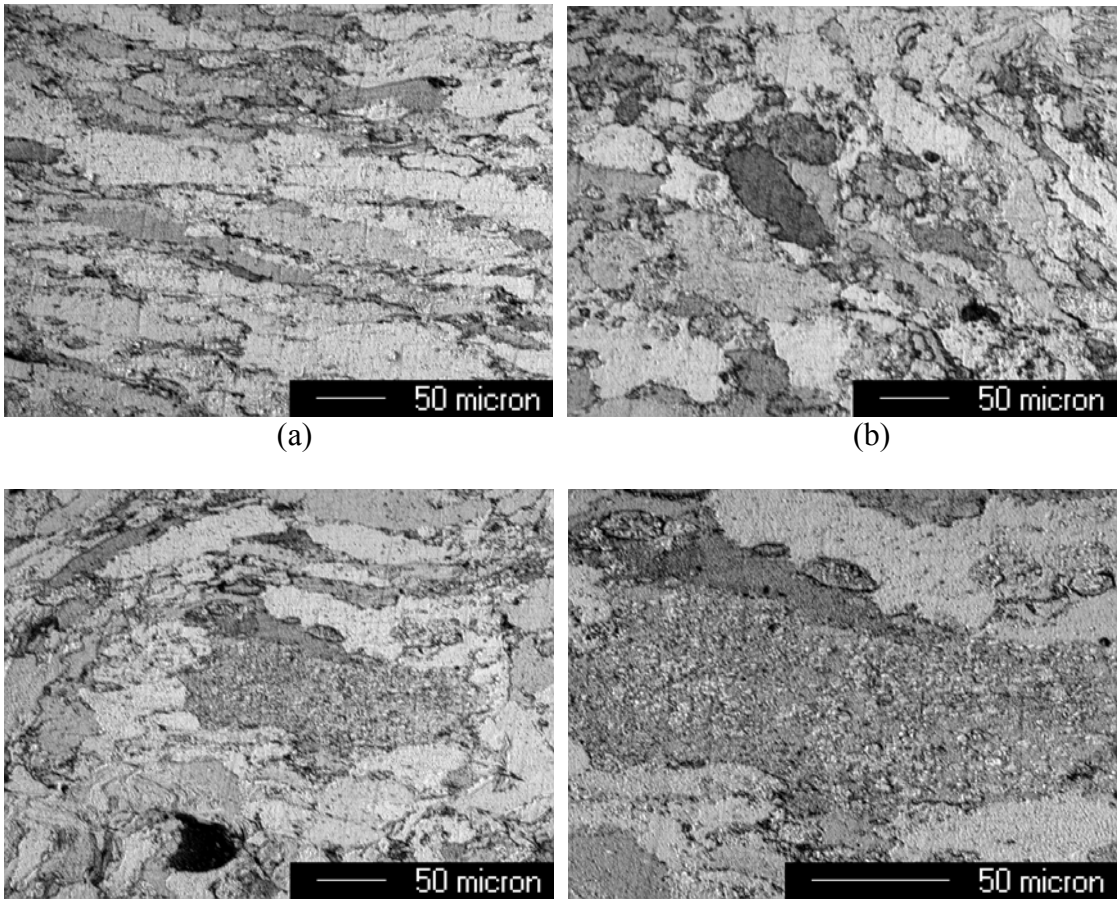

(a) (b)

(c) (d)

Figure 5.4 Presence of openings between deformed agglomerates. A very fine microstructure exists in the agglomerates.

5.1.1.3. Microstructural evolution and monotonic stress-strain response of bulk copper consolidates from micropowders

Figure 5.5 presents the tension and compression true stress - true strain response of consolidated 325 mesh Cu powder. As can be seen in the Figure, one ECAE pass was

not sufficient for full consolidation and both tension and compression specimens fractured prematurely. The best tensile response was observed in the sample consolidated using route 2B, which exhibited significant true tensile strain at fracture (19.2%) for an ultimate true tensile strength of 470 MPa. ECAE 2A and 2C samples showed a small strain at fracture while the ECAE 4C sample exhibited a final true strain of 9.4% at fracture as summarized in Table 5.2. Near elasto-plastic tensile response of the 2B and 4C samples is interesting to note as it contradicts the criteria for the onset of plastic instability ($d\sigma/d\varepsilon = \sigma$) [23]. For a true elasto-plastic behavior, necking should start right after the onset of yielding. However, no significant necking was observed in the fractured tension samples. Compression specimens exhibited a high ultimate strength level of 480 MPa and good ductility (except the sample from Route 1A). All compression experiments were stopped at a strain of 10% because of considerable shape change.

Figure 5.6 shows the microstructure of consolidated 325 mesh Cu powders obtained via different ECAE routes. The TEM foil normals were perpendicular to the longitudinal plane shown in Figure 2.2. The 2A and 2B ECAE consolidates show large areas with low dislocation density. The grains are well developed and are free from dislocations in some cases. The microstructure in the 2C sample is more homogeneous but contains high dislocation density regions without clear subgrain formation. Sample 4C exhibits well developed subgrains with relatively thick subgrain boundaries with a high dislocation density. Most of the grain boundaries are visible indicating substantial misorientation between grains. Note that some of them are poorly defined.

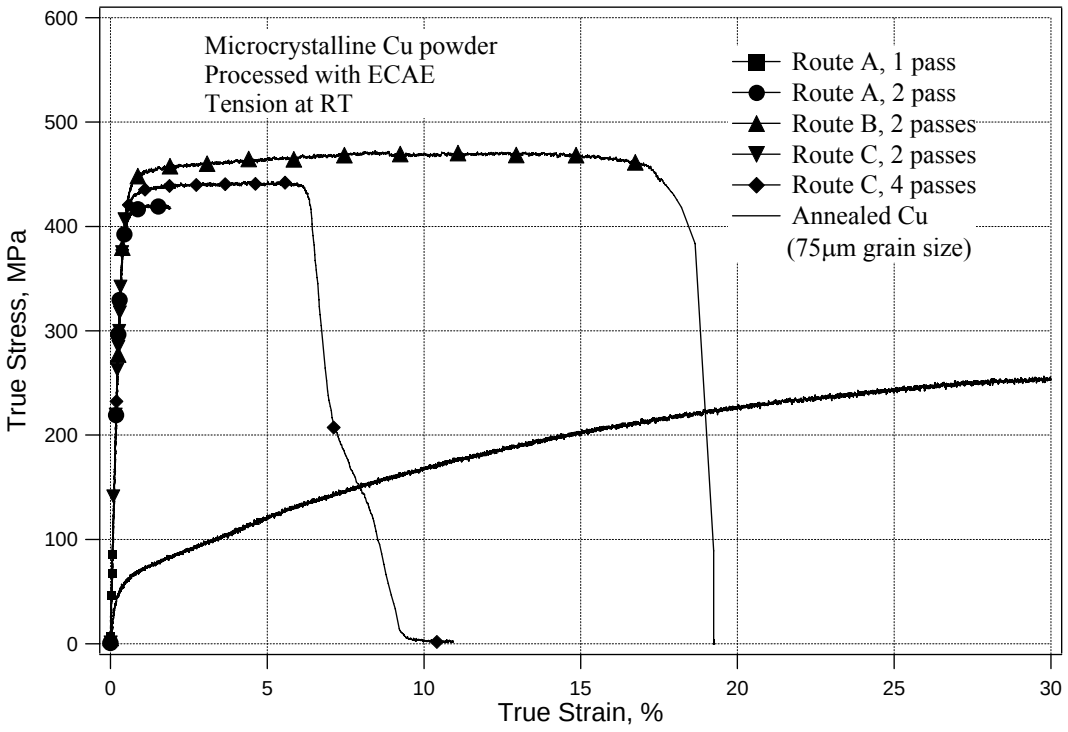

(a)

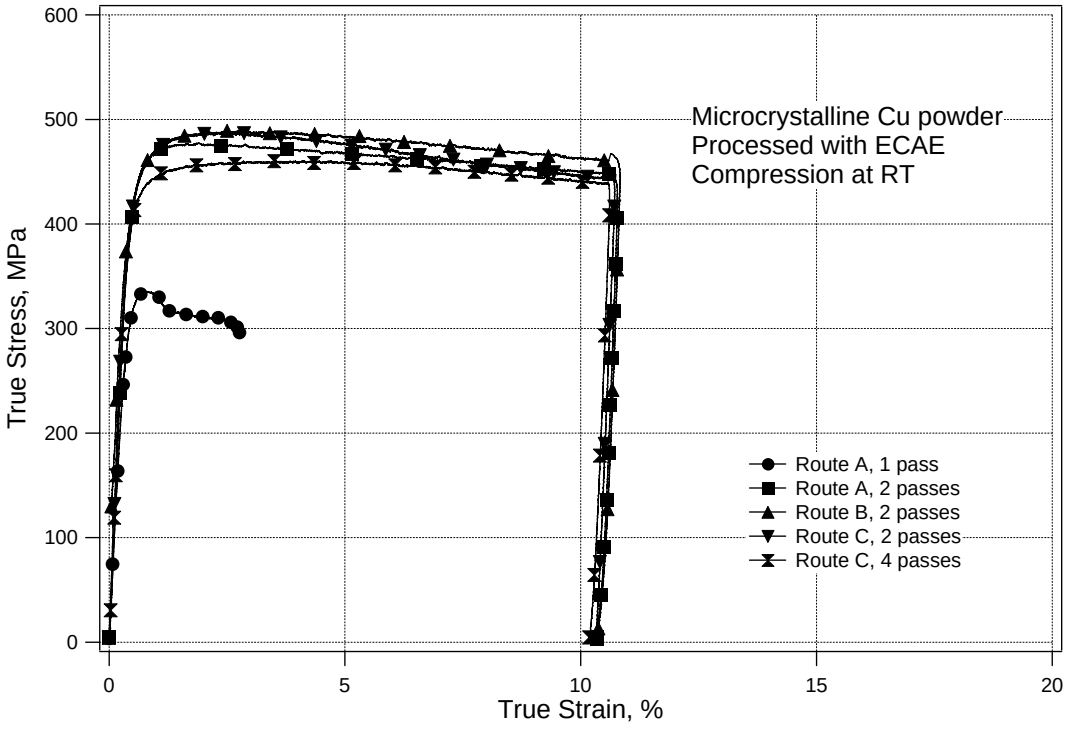

(b)

Figure 5.5 Room temperature tension (a) and compression (b) true stress – true strain response of consolidated microcrystalline Cu powder. The tension axis is parallel to the extrusion direction and the compression axis is perpendicular to the flow plane (see Figure 2.2).

Table 5.2 Summary of the experimental results: density, grain size, tension and compression mechanical properties of consolidated Cu powders and bulk extruded Cu. ED: Loading along the extrusion direction, FD: Loading perpendicular to the flow plane shown in Figure 2.2.

ECAE Route	Powder Size	Percentage Density (%)	Grain Size		Tension (Extrusion Direction)				Compression		
			X-Ray	TEM	E (GPa)	σ_y (0.2%) (MPa)	σ_{UTS} (MPa)	ε_f (%)	E (GPa)	σ_y (0.2%) (MPa)	σ_{UTS} (MPa)
1A	- 325 mesh (4.2 μm from X-Ray)	97.4	-	-	109	-	-	-	81	330 (FD)	335 (FD)
2A		98.3	315 nm	200 – 300 nm (some grains >500 nm)	115	406	420	1.9	110	437 (FD)	477(FD)
2B		99	300 nm	200 – 300 nm (some grains < 100 nm)	108	433	470	19.2	93	428 (FD)	488 (FD)
2C		98.8	250 nm	200 - 300 nm	114	-	409	0.5	106	440 (FD)	489 (FD)
4C		98.3	260 nm	250 nm	115	418	443	9.4	111	418 (FD)	460 (FD)
2B	130 nm (from X-Ray, about 100 nm from TEM)	95.6	110 nm	70 - 100 nm	104	690	728	1.20	101	399 (ED)	694 (ED)
2C		95.8	140 nm	~200 nm and 50 - 80 nm	-	-	-	-	92	560 (ED)	760 (ED)
4E		97	-	~250 nm and 40 – 80 nm	92	516	546	0.87	90	473 (ED)	628 (ED)

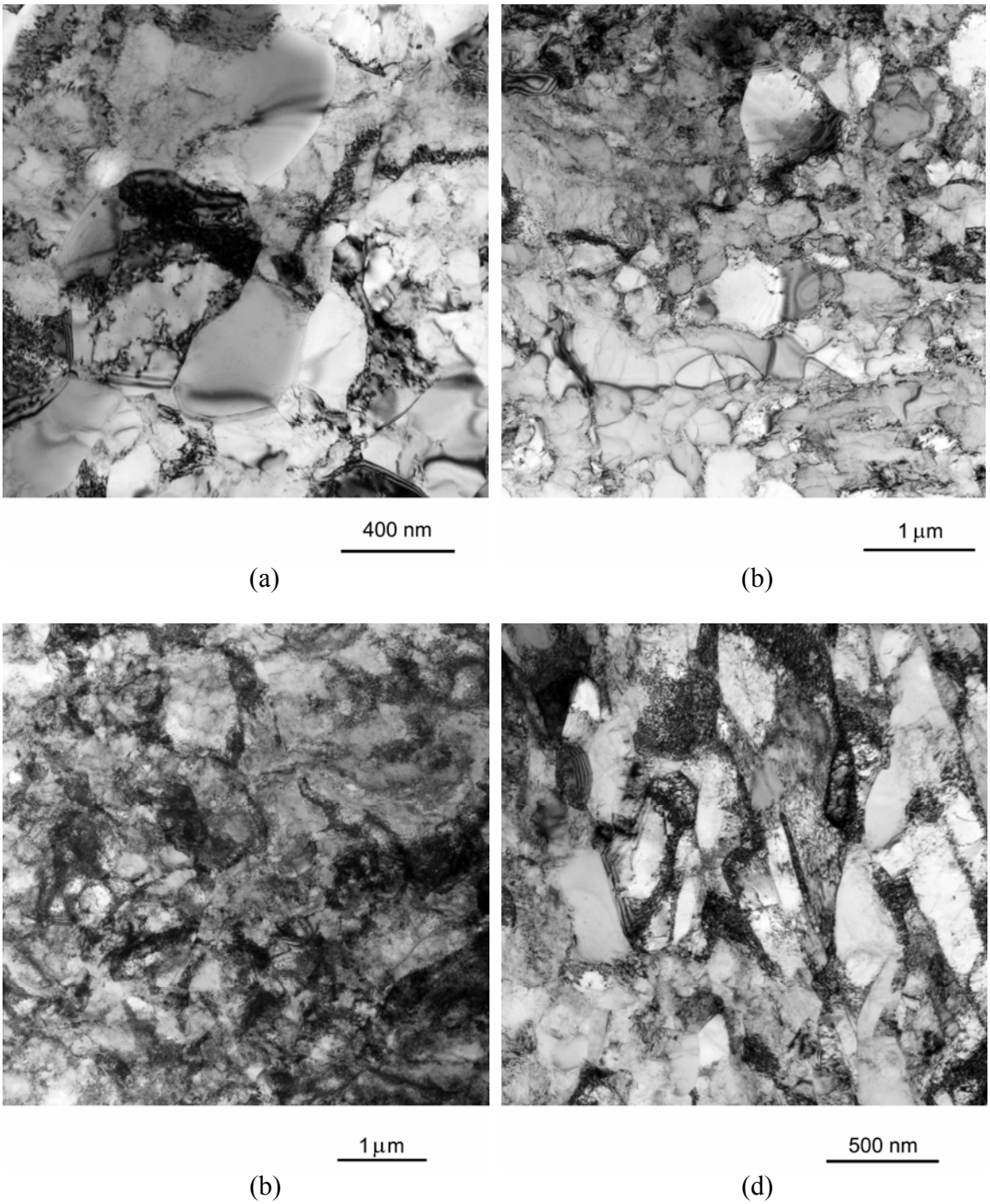

Figure 5.6 Bright field TEM micrographs of ECAE processed 325 mesh Cu powder following the routes: (a) 2A, (b) 2B, (c) 2C, and (d) 4C. The foil normal is perpendicular to the longitudinal plane shown in Figure 2.2.

5.1.1.4. *Microstructural evolution and monotonic stress-strain response of 130 nm Cu powder consolidates*

The tension and compressive response of consolidated 130 nm Cu powder are presented in Figure 5.7. Tension specimens were cut along the extrusion direction from the 2B and 4E consolidates. These specimens exhibit very high fracture strength (728 MPa for 2B and 546 MPa for 4E), but display no significant ductility. The strains at fracture are 1.20% for 2B and 0.87% for 4E. Compression specimens were also cut along the extrusion direction. These materials exhibit high ultimate strengths reaching 760 MPa in the case of 2C material. The ultimate strength is 694 MPa for 2B and 628 MPa for 4E. Strain before failure is relatively large in 2B (15.5%) while the 4E compression specimen experienced large plastic deformation and a drastic shape change without ultimate fracture. Table 5.2 summarizes these results.

TEM micrographs of consolidated 130 nm Cu powder following route B (Figure 5.8.a) indicate the presence of very fine subgrains (about 100 nm). The large light gray area in Fig. 5.8.a with a small change of contrast indicates a low misorientation between small subgrains. Figure 5.8.b shows a low magnification of consolidated 130 nm Cu powder following route C. The microstructure is relatively uniform with some large grains in the submicron range. The grains are mostly equiaxed and separated by high-angle boundaries. A higher magnification TEM image (Figure 5.8.d) of the region shown in Figure 5.8.b demonstrates a uniform distribution of the grains less than 80 nm with a fairly narrow grain size distribution. This shows that this sample essentially has a bimodal grain size distribution. Indeed, this was also the case for 2B and 4E samples. In the 4E sample (Figure 5.8.c), most of the grains were less than 100 nm (70 – 100 nm) in

size. Some grains, which were on the order of 200-300 nm, consisted of agglomerates of subgrains less than 100 nm. These subgrains were separated by low-angle grain boundaries. Some of the grain interiors appeared to be devoid of dislocations.

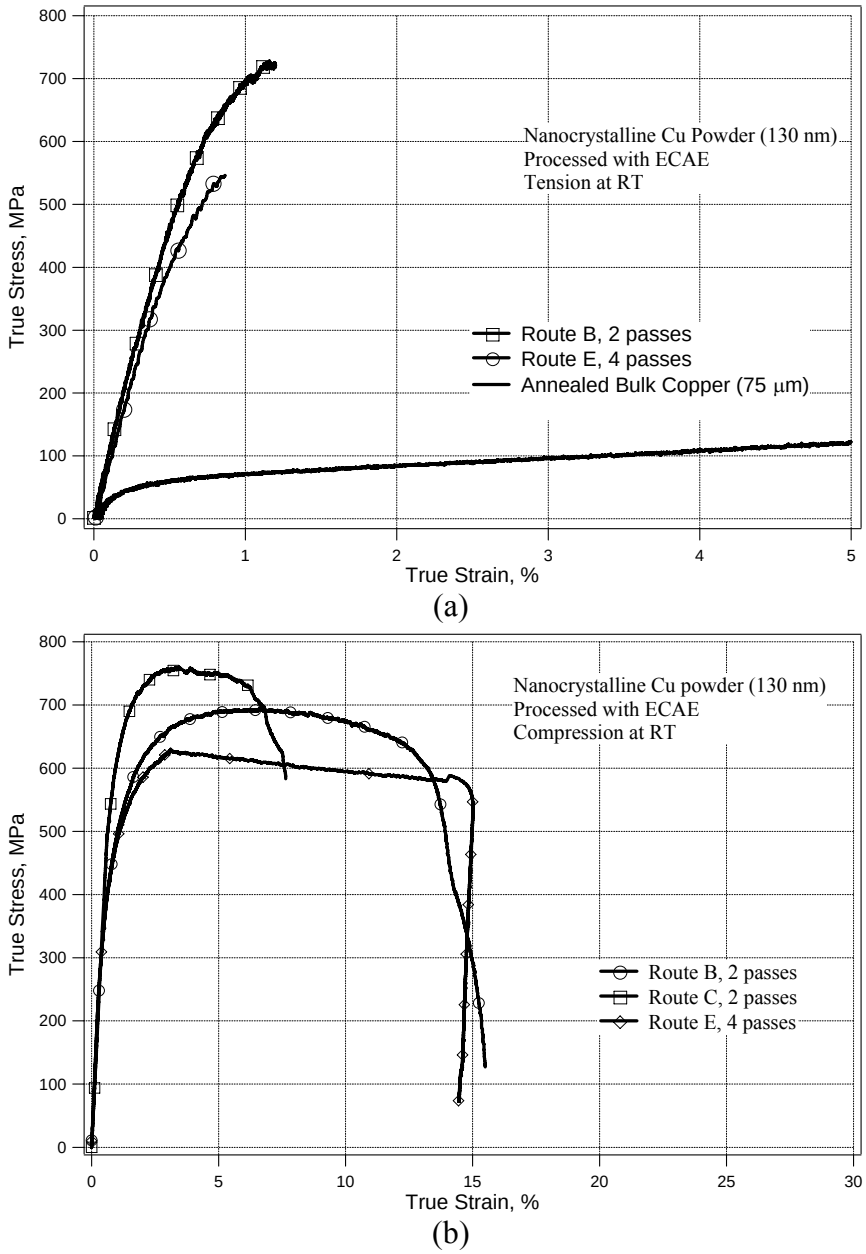

Figure 5.7 Room temperature tension (a) and compression (b) true stress – true strain response of consolidated 130 nm Cu powder. Both the tensile and compressive loading axes are parallel to the extrusion direction.

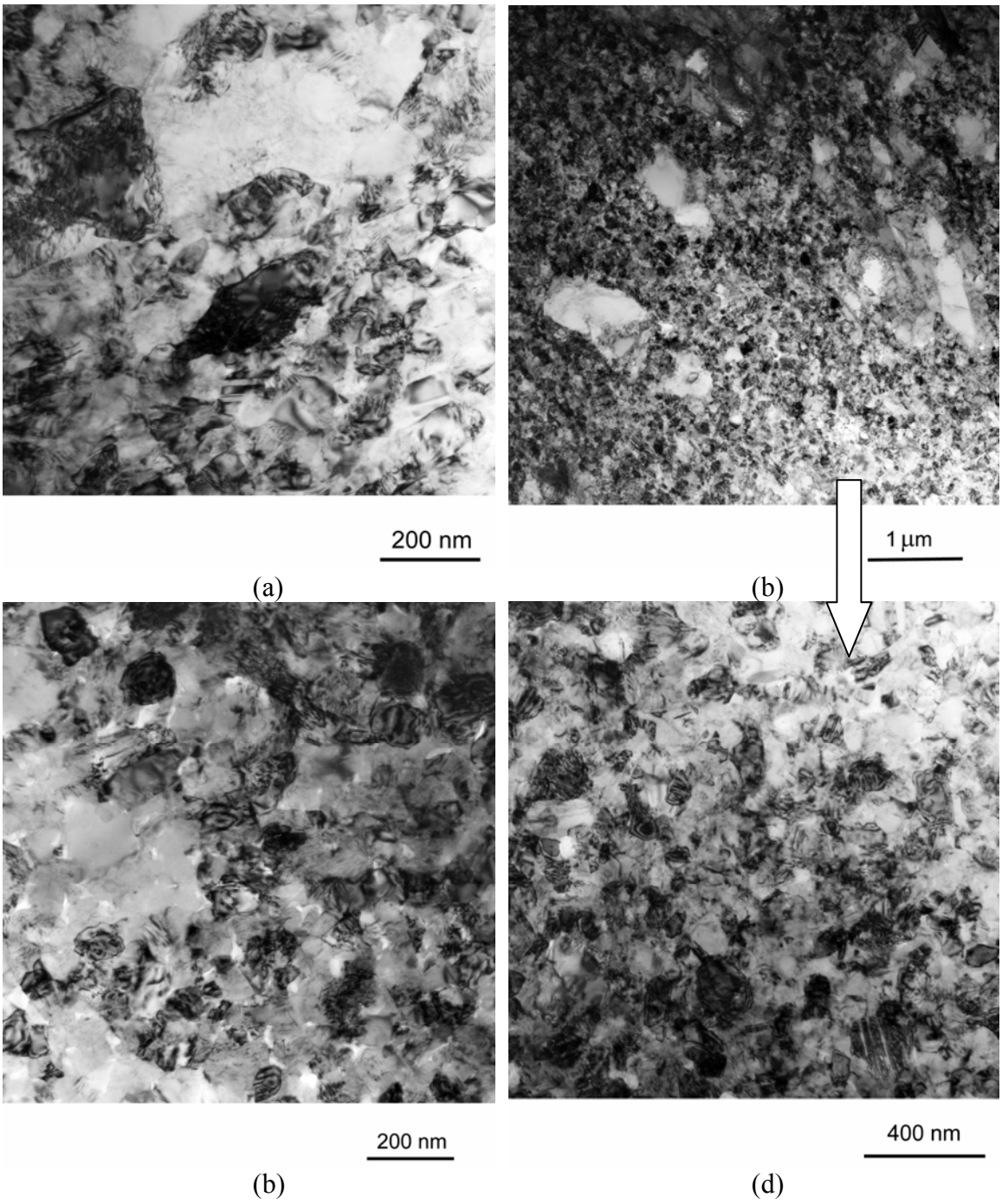

Figure 5.8 Bright field TEM micrographs (the foil normal is perpendicular to the longitudinal plane) of ECAE processed 130 nm Cu powder following different extrusion routes, (a) 2B, (b) and (d) 2C, and (c) 4E. The foil normal is perpendicular to the longitudinal plane in Figure 2.2.

Average grain sizes were determined for all the preceding cases using X-ray diffraction analyses. The values are reported and compared to grain sizes obtained from several representative TEM micrographs in Table 5.2. In finding these grain sizes from TEM images, there has not been a clear distinction between grains and subgrains. Relative densities achieved during consolidation of both 325 mesh and nano powders are also listed in Table 5.2.

5.1.2. Stage II and III: Powder compaction by hand press and cold isostatic press

The initial mechanical testing on Cu consolidates showed promising results. Consolidated Cu powders exhibited an exceptionally high strength (of about 760 MPa in tension) but limited ductility. To remedy the problem of low strains at fracture, two different fronts were explored:

- Premature fracture is thought to be due mainly to the debonding between agglomerates of Nanocrystalline particles. The arrows in Figure 5.9.b show potential sites for such debonding which appear to be prior agglomerate boundaries because of their size. Since the initial powder agglomerates, the porosity distribution is bimodal once the powder is initially compacted: very fine porosity between 130 nm powders and large porosity in between agglomerates. The porosity between the agglomerates should be minimized prior to consolidation. In order to solve this problem, we tried to compact the powder inside the can prior to extrusion using a hand press in a vacuum glove box. This method would also permit larger consolidates since it increases initial compact density. But this method created compact layers with well defined boundaries where shear can occur preferentially during extrusion leading to a non uniform consolidation. The application of high hydrostatic pressures through Cold

Isostatic Pressing (CIP) would assure not only high densification of extruded compacts but also will contribute to the break down of the agglomerates. Subsequent appropriate processing schedules involving routes with early orthogonal rotation (route B) should be effective for further disintegration of the agglomerates.

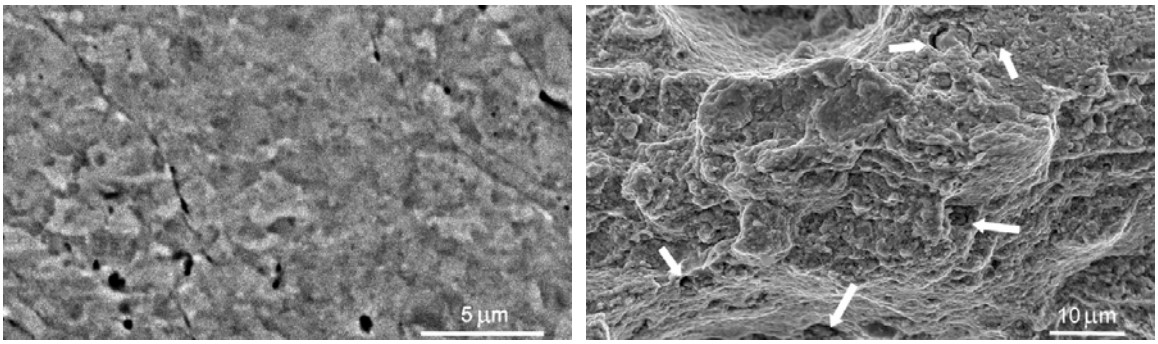

(a) (b)

Figure 5.9 (a) BSE micrograph of consolidated 325 mesh Cu powder consolidate (2B) showing some residual porosity. (b) Fracture surface of a tensile sample from the 130 nm copper powder consolidate (4E). The arrows show potential sites for interparticle debonding.

- Similar to extruded bulk Cu, an increase of ductility is expected through the formation of a bimodal distribution of grain size (Figure 5.8.b). The bottom up approach provides a considerable advantage by permitting a better control of the final microstructure. Indeed, a powder blend of 75 % of 100 nm and 25 % of -325 Cu powders was considered to achieve a systematic bimodal distribution of grain size in the consolidates.

Table 3.2 summarizes the supplementary extrusion runs in stages 2 and 3 of the study. The choice of the routes and number of passes was determined progressively from the

results yielded from each case. It was determined that route 4B permits the best consolidation and therefore was adopted solely in the case where the powders were CIPed.

ECAE processing of cans containing 50 nm Cu powders through different routes and number of passes did not permit a good consolidation. Therefore no mechanical tests were done for cases 19-21. The consolidation of 50 nm Cu powders was not feasible despite the careful preparation of the cans in a vacuum environment to avoid chemical contamination, and the degassing of the powder for 3 hours under a temperature of 130C to eliminate any entrapped moisture. Because of the very small size of the powder, minor oxidation at any step of can preparation, or else even after the fabrication of the powder itself during the electro-explosion process, will not be negligible and the oxide layer formed at the surface of the particles, though very thin, would affect the chemical composition of the powder and its chemical, physical properties in relation to the bonding, hindering the possibility of good consolidation.

On the other hand, the use of a hand press to compact the nanocrystalline powder was not very conclusive. For cases involving only two passes, the consolidation was not successful for route A (case#22) as the material crumbled during the extraction step. For route B (case#23), it was possible to extract the consolidate from the can but the tested tension specimens did not yield a significant strain at fracture (0.78%) which is slightly lower from the results achieved when the powder was compacted manually (1.20%). Four passes using route C' did not improve the results as three extrusions were run following this route, only one of these permitted a usable consolidate for mechanical testing with a maximum of strain at fracture of (0.71%). The hand pressing proved to yield non

reproducible and inconsistent results as it is a function of the manual operation of pressing which introduces layers between different steps of compaction. In order to decrease the effect of these layers, a route with orthogonal rotation in different directions between passes namely route B was tested. Also, in order to reduce the effect of shear banding in the response of the specimen in tension, tension samples were EDM cut with the flat surface parallel to the shear plane as shown in Figure 3.11. This later scheme permitted an extraordinary increase of the fracture strain to 6.48% for an ultimate strength of around 700 MPa. Route B given 4 passes was adopted consequently for the remaining extrusion of cans filled with CIPed powders.

The material yield for stage 3 was important due to the high compaction achieved during powder CIPing. Figure 5.10 shows pictures of the extracted consolidated Cu powders where tension profiles were cut. The height of the consolidates is approximately 15 to 20 mm. The hand pressing or CIPing of microcrystalline powder did not cause any change of the results already obtained by the manual tapping of the powder. The spherical shape and size of this powder allows a maximum packing by a simple tapping without having to resort to any additional compaction. Table 5.3 summarizes the mechanical results for the consolidated nanocrystalline Cu powders in stages 2 and 3, and Figure 5.11 reports some selected results where the strain fracture is maximum for the three different stages.

(a)

(b)

(c)

Figure 5.10 Consolidate extracts of extruded CIPed powders through 4B for (a): 100 nm, (b): -325 Mesh, (c): Blend of 25% -325 Mesh and 75% 100nm Cu powders.

Table 5.3 Mechanical results for the consolidated nanocrystalline Cu powders in stages 2 and 3.

Case #	Route	Powder size, Compaction	Tension (Extrusion direction)			
			E (GPa)	$\sigma_{y(0.2\%)}$(MPa)	σ_{UTS}MPa)	ε_f(%)
22	2A	130nm, HP*	-	-	-	-
23 (1)	2B	130nm, HP	89	-	414	0.64
23 (2)	2B	130nm, HP	85	457	468	0.78
24 (1)	4B	130nm, HP	99	545	662	1.99
24 (2)	4B	130nm, HP	104	591	747	3.26
24 (3)	4B	130nm, HP	106	578	751	5.53
24 (4)	4B	130nm, HP	95	533	694	6.48
25 (1)	4C'	130nm, HP	-	-	-	-
25 (2)	4C'	130nm, HP	-	-	-	-
25 (3)	4C'	130nm, HP	85	-	467	0.71
29 (1)	4B	100nm, CIPed	117	604	725	4.54
29 (2)	4B	100nm, CIPed	117	609	759	5.10
29 (3)	4B	100nm, CIPed	101	603	790	6.36
29 (4)	4B	100nm, CIPed	99	562	735	7.27
30 (1)	4B	CIPed Blend**	107	513	636	2.19
30 (2)	4B	CIPed Blend**	105	495	634	2.70

*HP: Hand Pressed.
**CIPed Blend: 25% of -325 Mesh and 75% of 100nm Cu powders.

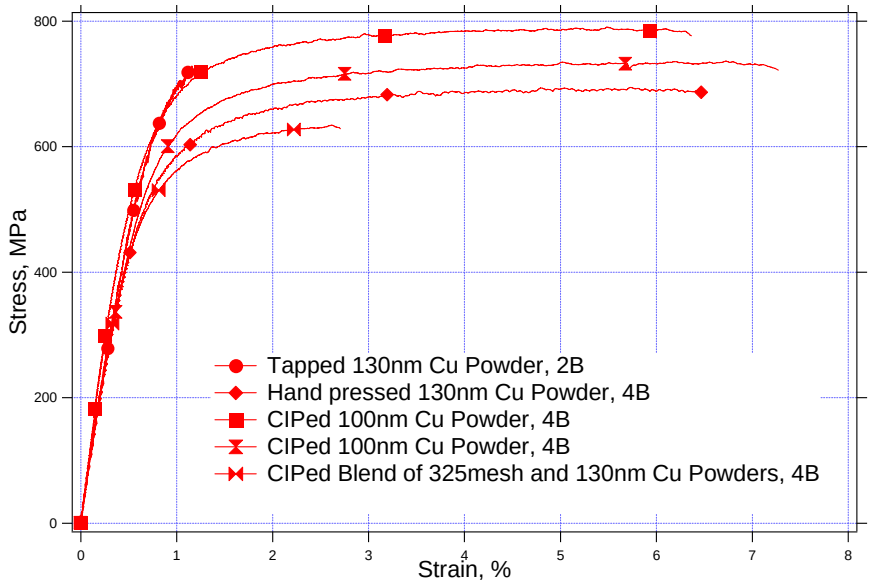

Figure 5.11 Selected stress-strain results for consolidated nanocrystalline Cu powders.

5.2. Discussion of the results

The motivation of this study was to achieve consolidation of micro and nano copper particles and obtain consolidates with significant dimensions in order to conduct mechanical and structural characterizations. The consolidated of micron range particles resulted in a smaller dislocation density in certain ECAE routes than from ECAE processed wrought copper. As opposed to bulk ECAEd samples, the consolidated copper powder did not undergo macroscopic plastic instability and did not show significant necking. Thus, the mechanical response of the consolidated copper was unique in the sense that it showed near elasto-plastic response. This finding has also some implications for improving the fatigue life of severely deformed consolidated copper. Although it is difficult to achieve grain sizes less than 100 nm with ECAE of bulk Cu, the consolidation of copper nanoparticles was successful in achieving grain sizes between 50 and 100 nm. Nanoparticle consolidates also consist of some uniformly dispersed grains in the range of 200 nm grain size with internal subgrains. However, it was concluded that this bimodal grain distribution was useful in achieving very high strength and relatively high ductility in compression. The compressive strength levels achieved in pure copper with grain sizes above 50 nm in this study are the highest reported so far. Note that Wang *et al* [71] recently reported a similar tensile strength value for nanocrystalline copper with 30 nm grain size but their specimen thickness was only 15 μm. The large scatter in the dependence of yield strength as a function of grain size is likely because of the bimodal grain size distribution and processing induced flaws, instead of the competition between dislocation controlled and grain boundary controlled (grain boundary sliding and Coble Creep) mechanisms as discussed below.

The early tensile fracture in the ECAE processed 325 mesh Cu powder after one pass can be attributed to the presence of porosity. This is asserted by the fact that Young's Modulus (Table 5.2) under both tension and compression is lower for this sample compared to the samples consolidated using more passes. There is also a slight difference in the Young's moduli of the samples from different ECAE routes as well as in the tension and compression samples of a given ECAE route. It has been shown in a previous study [46] that different ECAE routes lead to different final textures for pure Cu. Therefore, both the former and latter differences in Young's moduli could be attributed to texture. For the latter, as the tensile specimens were cut along the extrusion direction and the compression specimens along the flow plane normal, the loading direction is different for both type of samples.

The texture of a 130 nm 4E consolidate is shown in Figure 5.12. The inverse pole figure of the transverse plane (Figure 5.12) shows a preferred orientation about two major components: <100> and <111>. The measured texture for 4E ECAE bulk Cu [46] shows similar results, i.e. ECAE of bulk copper and powder will essentially lead to the same texture. Texture components found in the transverse plane for 4A, 4B, 4C for bulk Cu are respectively composed of the following major components: <133>(65%) + <100>(35%), <122>(63%) + <100>(37%) , and <111>(54%) + <100>(46%), respectively. The percentages correspond to an estimation of the importance of each component and were determined using the strength log scale of the measurement. The Young's modulus can be determined from these components using the equation (5.1):

$$\frac{1}{E_d} = \frac{1}{E[100]} + f \times \left(\frac{1}{E[111]} - \frac{1}{E[100]} \right) \qquad (5.1)$$

with $\frac{E[111]}{E[100]} = 2.91$ and $E[100] = \frac{1}{s_{11}} (s_{11} = 15.25\ TPa^{-1})$ for pure Cu, and $f = \alpha^2\beta^2 + \beta^2\gamma^2 + \alpha^2\gamma^2$ where α, β, and γ are the direction cosines. Hence, E[100] = 65 GPa, E[111] = 191 GPa, E[122] = 158 GPa, E[313] = 143 GPa, and E[110] =130 GPa. A rough estimate of Young's modulus of samples for each route can be determined using these values weighted by the percentage of each component. Therefore, E (4A) = 115 GPa, E (4B) = 124 GPa, E (4C) = 133 GPa, and E (4E) = 116 GPa along the extrusion direction. These calculated values are reasonably close to the experimental values reported in Table 5.2.

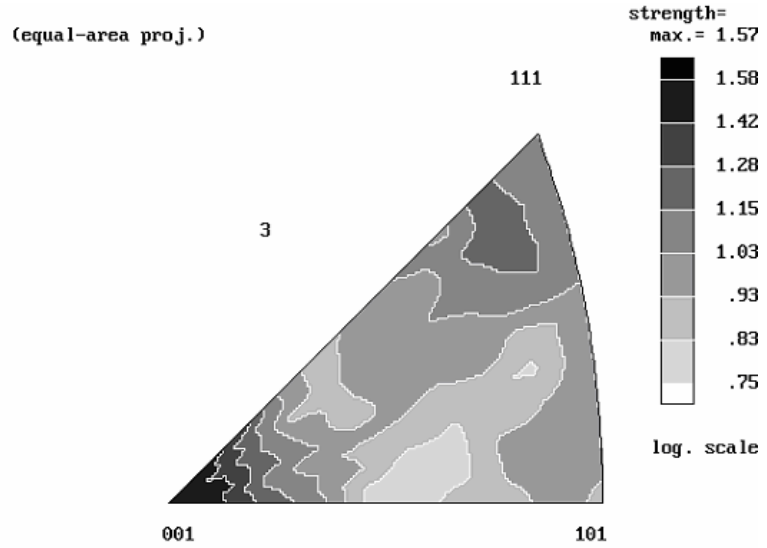

Figure 5.12 Inverse pole figure for transverse plane (see Figure 2.2) of consolidated 130 nm Cu powder via ECAE using route 4E. The inverse pole figures were calculated using popLA software [102].

Table 5.2 reports the yield stresses determined from tensile and compression stress-strain responses at a strain offset of 0.2%. For 325 mesh consolidates, a difference in yield strength can be noticed between compression and tension responses of the 2A

and 2B routes. A similar tension – compression asymmetry was observed by Valiev (Figures 3 and 4 of [103]) in ECAEd coarse grained bulk copper, however, there was not any explanation on the possible causes. We have previously shown [46] that the direction normal to the flow plane (FD in Table 5.2) has <110> and <111> texture components in 2A extruded samples and <133> and <110> components for 2B and 4C extruded samples, respectively. Similarly, the extrusion direction (ED in Table 5.2) has the <133>, <122>, and <100> components for 2A, 2B and 4C extruded samples, respectively. These components are assumed to yield plastically first because of their high Schmid factors. As the critical resolved shear stress should be the same regardless of the direction of the loading, one can write the following relation;

$$\sigma_{comp}^{yield} = \sigma_{tens}^{yield} \frac{m_{tens}}{m_{comp}} \qquad (5.2)$$

where σ^{yield} is the yield strength and m is the Schmid's factor. Since <100> and <110> have the same Schmid's factor, 4C consolidated sample should have the same tensile and compressive yield strength, as indeed observed experimentally (Table 5.2). For 2A and 2B consolidated samples, equation (5.2) is in agreement with the experimental values as σ_{comp} (2A) > σ_{tens} (2A) (because m_{tens} (2A) > m_{comp} (2A)), and σ_{tens} (2B) > σ_{comp} (2B) (because m_{tens} (2B) < m_{comp} (2B)).

It is interesting to note that the 2C tension sample failed without any plastic deformation (Figure 5.9.a). The 180° rotation between passes in Route C may lead to debonding along prior powder boundaries or opens the gaps between powders along the

shear plane, and fracture initiates during tensile loading along the ECAE shear plane. Clearly, route B is a much more promising route as the strain at fracture is approximately 20% with an ultimate strength of 470 MPa. Although the backscattered electron micrograph of polished 2B ECAE processed 325 mesh Cu powder (Figure 5.9.a) shows some residual porosity, the elongation at fracture of this material is similar to those of the ECAE processed bulk copper.

Similarly, the premature fracture of tension specimens observed in the consolidated 130 nm manually tapped Cu powder (Figure 5.7.a) can be attributed to the remnant porosity (Figure 5.9.b) and to premature debonding between agglomerates. The fracture surface in Figure 5.9.b suggests that the fracture may initiate due to interparticle debonding. The arrows in Figure 5.9.b show potential sites for such debonding which are thought to be prior agglomerate boundaries because of their size. Since the initial powder agglomerates, the porosity distribution is bimodal once the powder is initially compacted: very fine porosity between 130 nm powders and large porosity in between agglomerates. It is likely that once ECAE consolidation starts, the small pores are closed with the help of compression, shear deformation and deformation heating. Before the remaining relatively large pores are eliminated through consolidation, it is possible that grain growth in the fully dense prior agglomerates could occur. Indeed, the relatively large grains seen in Figure 5.8.b in the 130 nm consolidates may be the result of this grain growth driven by deformation heating. These grains could also be created because of large initial particles. However, the former explanation is believed to be the governing mechanism as many TEM images demonstrated that the powder size was quite uniform.

A potential advantage of this composite microstructure in Figure 5.8.b is the increase in tensile ductility.

Much of the plasticity exhibited by compression specimens is due to the existence of submicron size grains (100 – 500 nm) embedded in the very fine structure. It has been argued that the very fine matrix gives strength to the material while large grains accommodate strain hardening [61]. The enhancement of ductility requires then an appropriate extrusion schedule to decrease the porosity and to form simultaneously a bimodal distribution of grains where submicron size grains inside a nanocrystalline matrix can produce pronounced strain hardening during plastic deformation to assure large uniform deformation and to retard fracture. In order to obtain an even more uniform nanocrystalline bulk copper, we suggest that low shear strain levels (lower ECAE corner angle) should be applied initially to disintegrate the agglomerates. Then ECAE consolidation could result in a uniform microstructure.

On the other hand, in the consolidated micro Cu powders, there is not a clear softening due to plastic instability. The tension samples did not have any significant necking behavior as opposed to the bulk extruded samples. This near-perfect elastoplasticity behavior was also shown in a recent study by Champion *et al.* [23] in consolidated nanosized Cu particles (50 nm). The resulting average grain size was reported to be 80 nm [23] although their TEM images mostly showed subgrains with about 80 nm size. The authors suggested [23] that the mechanical instability criteria for nanocrystalline materials should be revisited since the observed near-perfect elastoplastic behavior is in contradiction with instability criteria, for example with the Considere Criterion. The present results support these findings [23]; however, our average grain size

is considerably larger than 80 nm (Figure 5.6 and Table 5.2). It can be argued that near-perfect elastoplasticity is partly due to the combined effect of the bimodal microstructure and the residual porosity. Larger grains in the bimodal structure lead to strain hardening but softening caused by residual porosity compensates the hardening. Similarly, strain hardening can also be balanced by a recovery mechanism such as absorption of dislocations by grain boundaries since the structure is heavily deformed. Before necking starts due to the deformation in larger grains, residual porosity may cause fracture. However, the compression stress-strain response (Figure 5.5.b), in which residual porosity should not cause softening as much as in tension, shows some softening behavior too. Therefore, the existence of a simultaneous recovery mechanism is a more plausible explanation.

The slight difference in strain hardening coefficients between tension and compression and small work softening under compression in Figures 5.5 and 5.7 is a common feature in ultrafine and nanocrystalline materials as reported in few recent publications [54-55,104]. This slight asymmetry in strain hardening coefficients and softening under compression has been attributed to the fine shear banding under compression. The ultrafine nature of the structures obtained by consolidation of particles or by other severe plastic deformation techniques may inherently have a sufficient defect population such that shear banding may occur before extended uniform deformation regime. Carsley *et al.* [104] have reported on deformation of a nanostructured bulk iron alloy that the stress necessary to initiate shear bands in compression was approximately 30% lower than the stress necessary to initiate shear bands in tension. That also might be

the reason why shear banding or necking in tension was not pronounced in the present study.

TEM micrographs of consolidated 130 nm Cu powder of other cases (Fig 5.13 for case# 18 in Table 3.4 where the can was processed via route 4C') indicate also the presence of a bimodal distribution of grain size. Fig.5.14.a shows an example of dislocation moderated deformation of large grains by means of dislocation pile ups. This TEM micrograph was taken from a foil prepared from specimen of consolidated 130 nm Cu powder through route 4E and tested in compression. Some of the large grain interiors appeared to be devoid of dislocations. This is an indicator that the material can sustain more plastic deformation if there is no catastrophic fracture. Figure 5.13 shows also a non uniform chemical etching of the TEM foil as a potential debonding line separating large grains is more aggressively etched which corroborates the idea of fracture initiation along intra agglomerates interfaces. The very fine matrix gives strength to the material. The accumulation of dislocations is impossible in these fine grains as they are emitted from one grain-boundary segment and disappear at the adjacent one, leaving no dislocations inside the grain interior. Transmission microscopy showed the existence of deformation twinning in the small grains (Fig. 5.14.b). The presence of twins may arguably be a proof of partial dislocation emission in nanostructured Cu which in coarse grained state does not deform by twinning at normal strain rates.

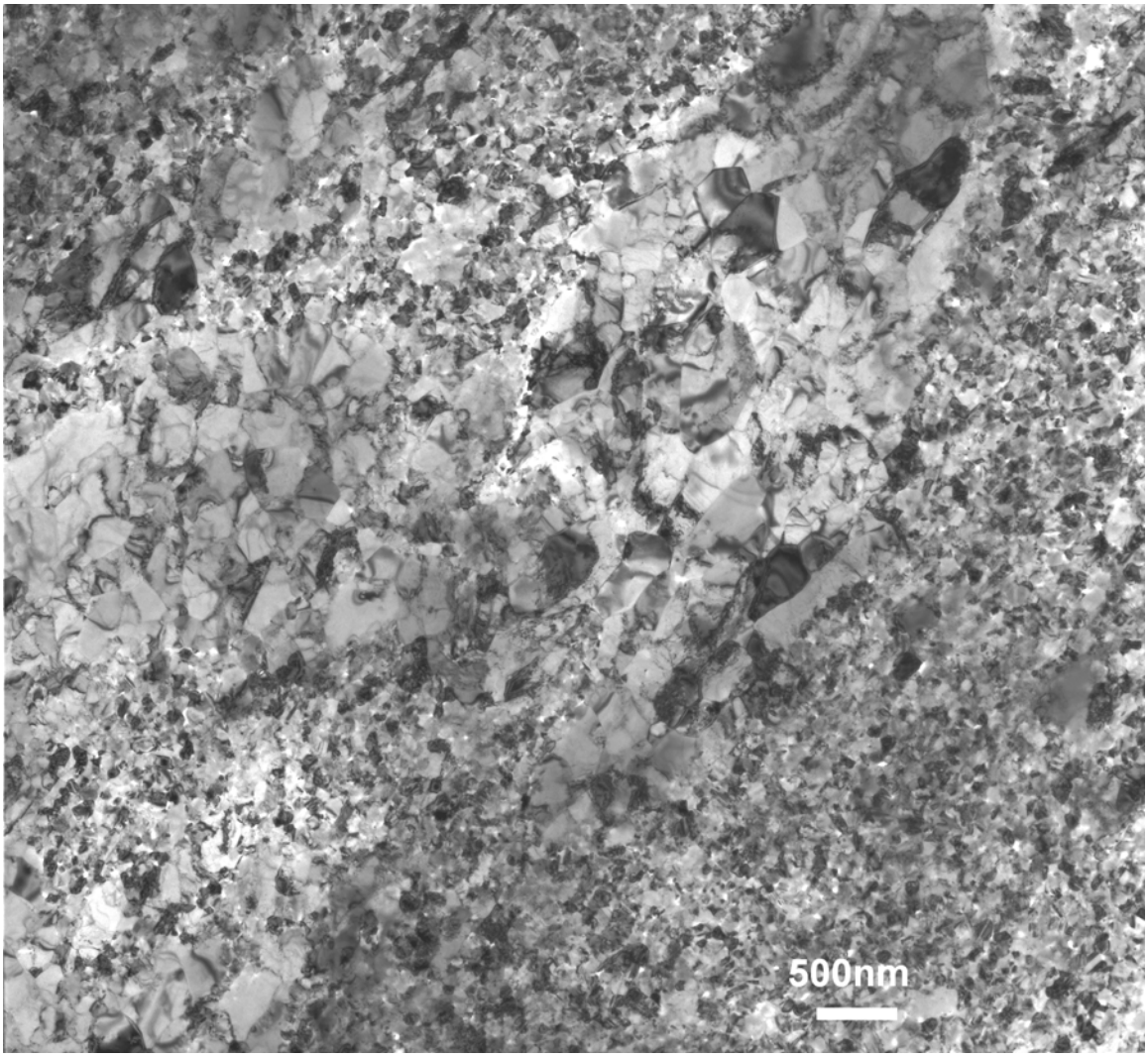

Figure 5.13 Bimodal distribution of grain size in consolidated 130 nm Cu powder following route 4C'. The picture shows also a preferential line of etching corresponding to a potential debonding site.

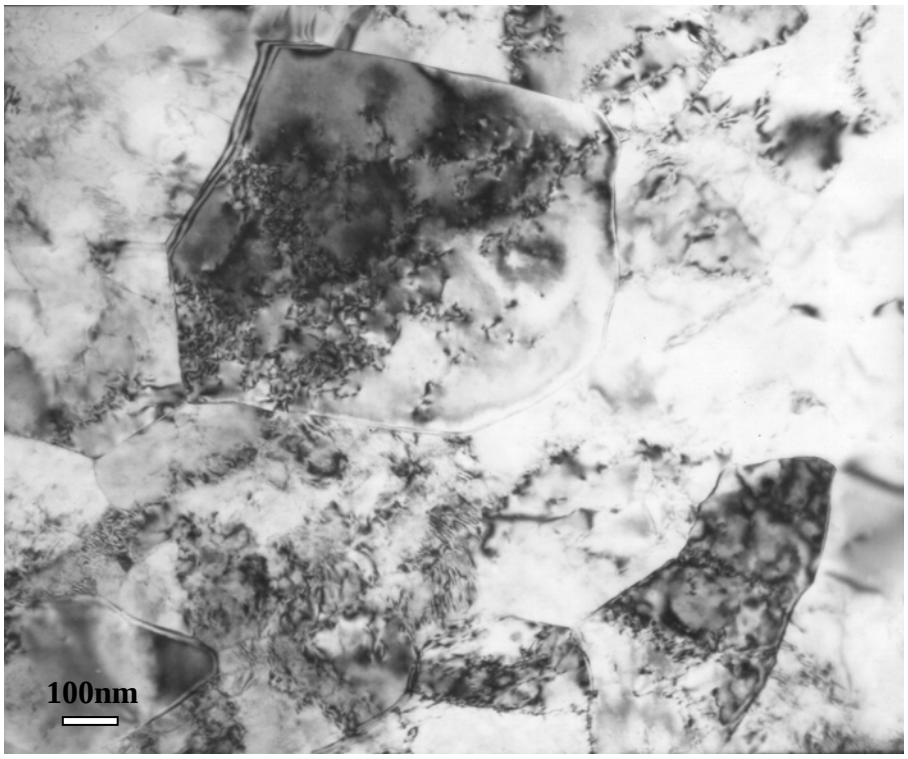

(a)

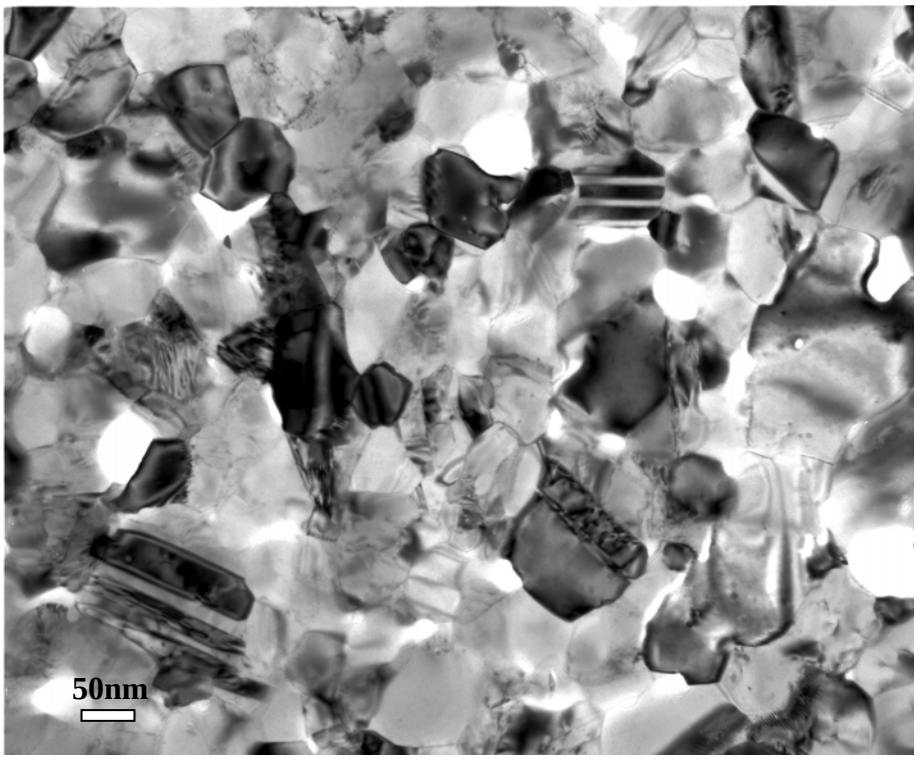

(b)

Figure 5.14 Deformation moderated by dislocations mobility in large grains (a), and presence of deformation twins in some small grains.

The deformation of some small grains by twinning seems to not have a detrimental effect at the macroscopic level. Only a few grains were observed in the TEM micrographs to deform by twinning, and most importantly, measurement of texture for consolidated Cu powders does not show an important evolution of texture components when compared to those measured for ECAEd bulk Cu. Figures 5.15-17 show a comparison of pole figures and inverse pole figures of consolidated Cu powders and ECAE processed bulk Cu. Figure 5.15 which reports pole and inverse pole figures of consolidated 130 nm Cu powder via route 4E are strikingly similar to the bulk Cu counterpart. The same similitude in texture features is observed in case 4B when consolidated 130nm (Figure 5.16.a,b), -325Mesh (Figure 5.17.a,b) and the blend of nanocrystalline and microcrystalline Cu powders (Figure 5.17.c,d) are compared to ECAE processed bulk Cu (Figure 5.16.c,d). There are however some differences in 4B case between the consolidates and bulk Cu which can be summarized in a certain global rotation of the texture, but there is no relative change between the main texture components. The slight difference encountered in 4B is due mainly to a possible rotation of the consolidate during extrusion which is possible because of the cylindrical chamber containing the powder. The rotation of the consolidate will be more important for routes involving rotation of the billet, hence the difference in textures was observed for route B and not route E.

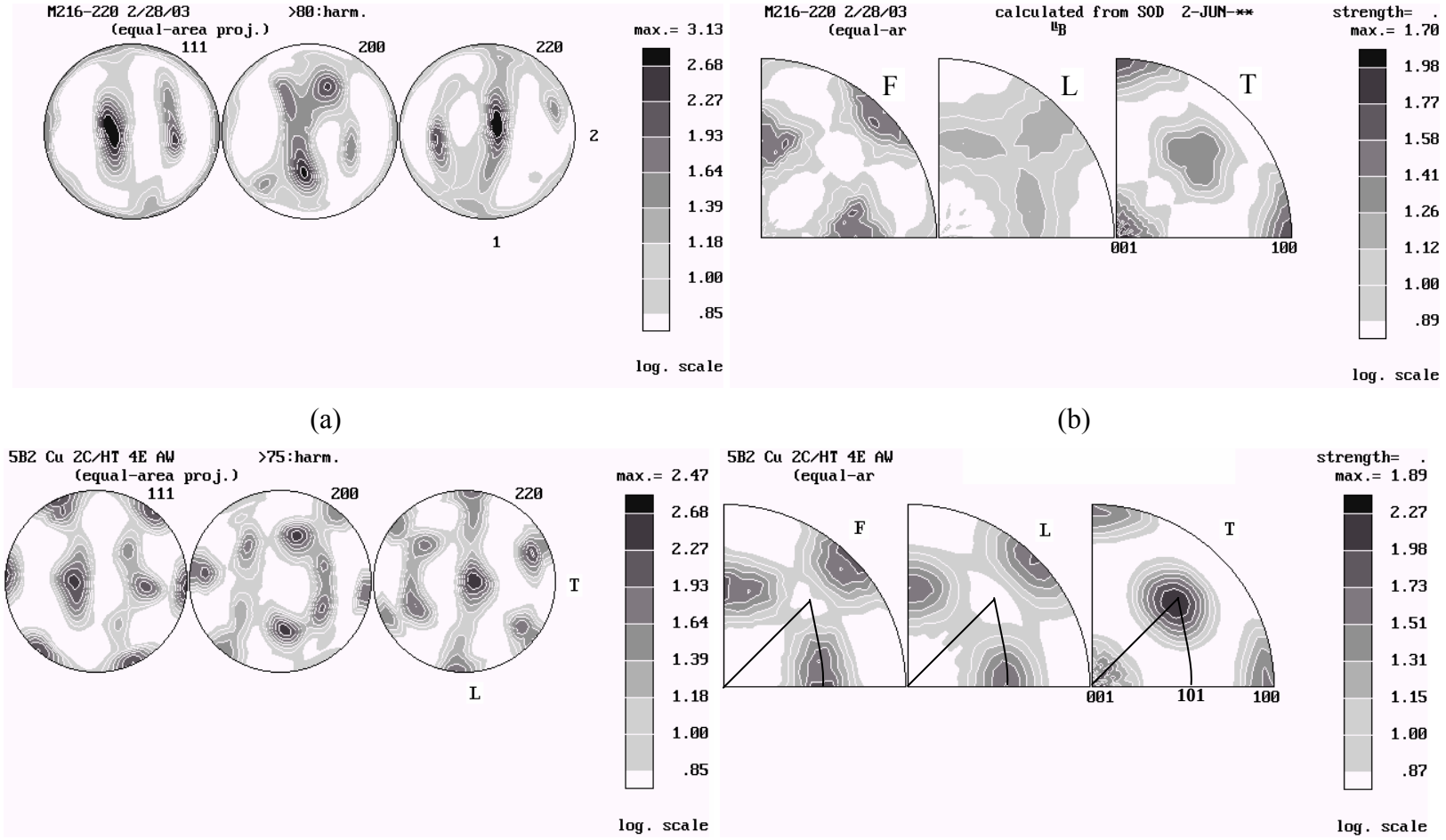

Figure 5.15 Comparison of pole and inverse pole figures of (a,b) of consolidated 130nm Cu powder and (c,d) of bulk Cu following route 4E

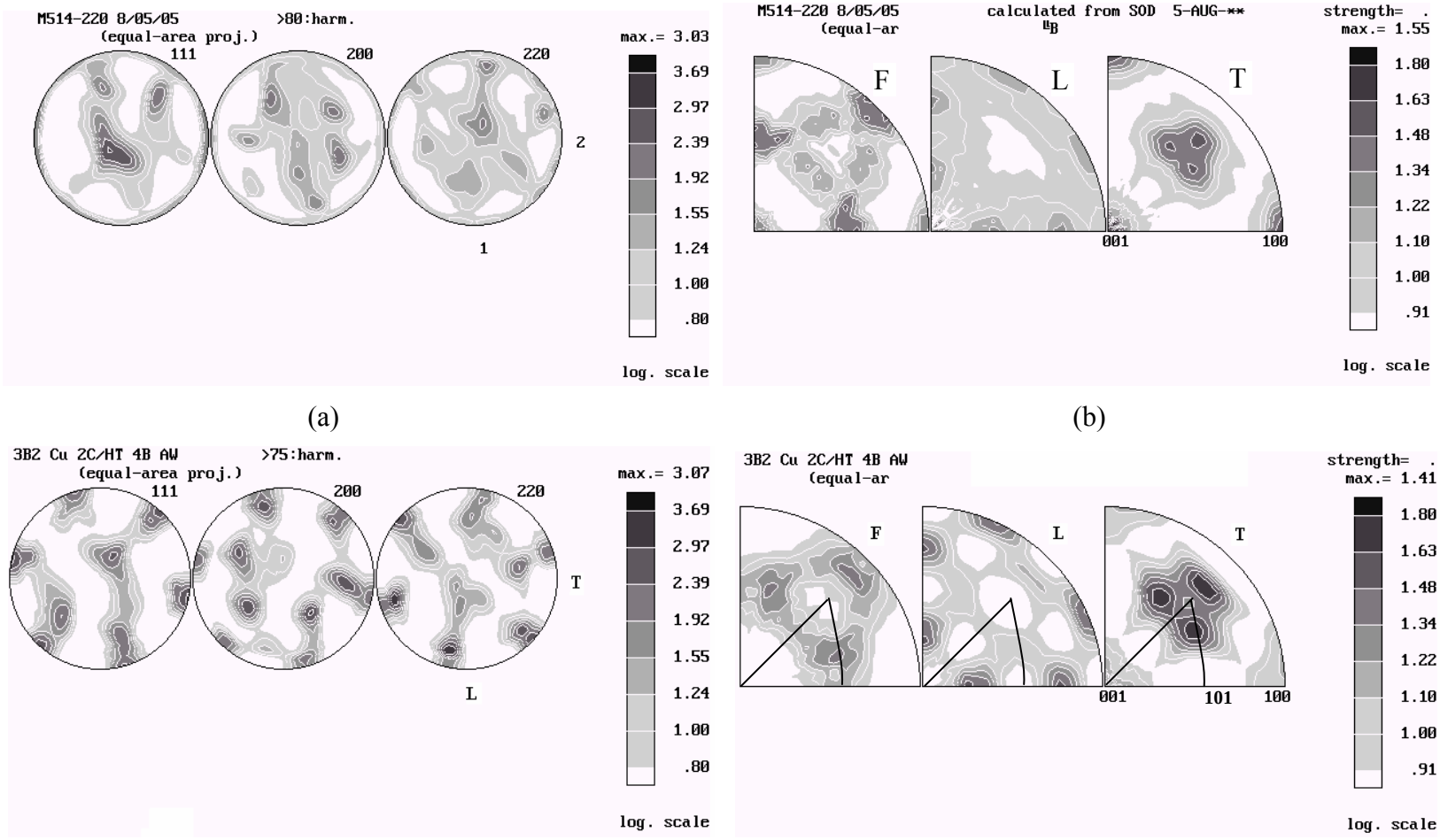

Figure 5.16 Comparison of pole and inverse pole figures of (a,b) consolidated 130nm Cu powder and of (c,d) bulk Cu following route 4B.

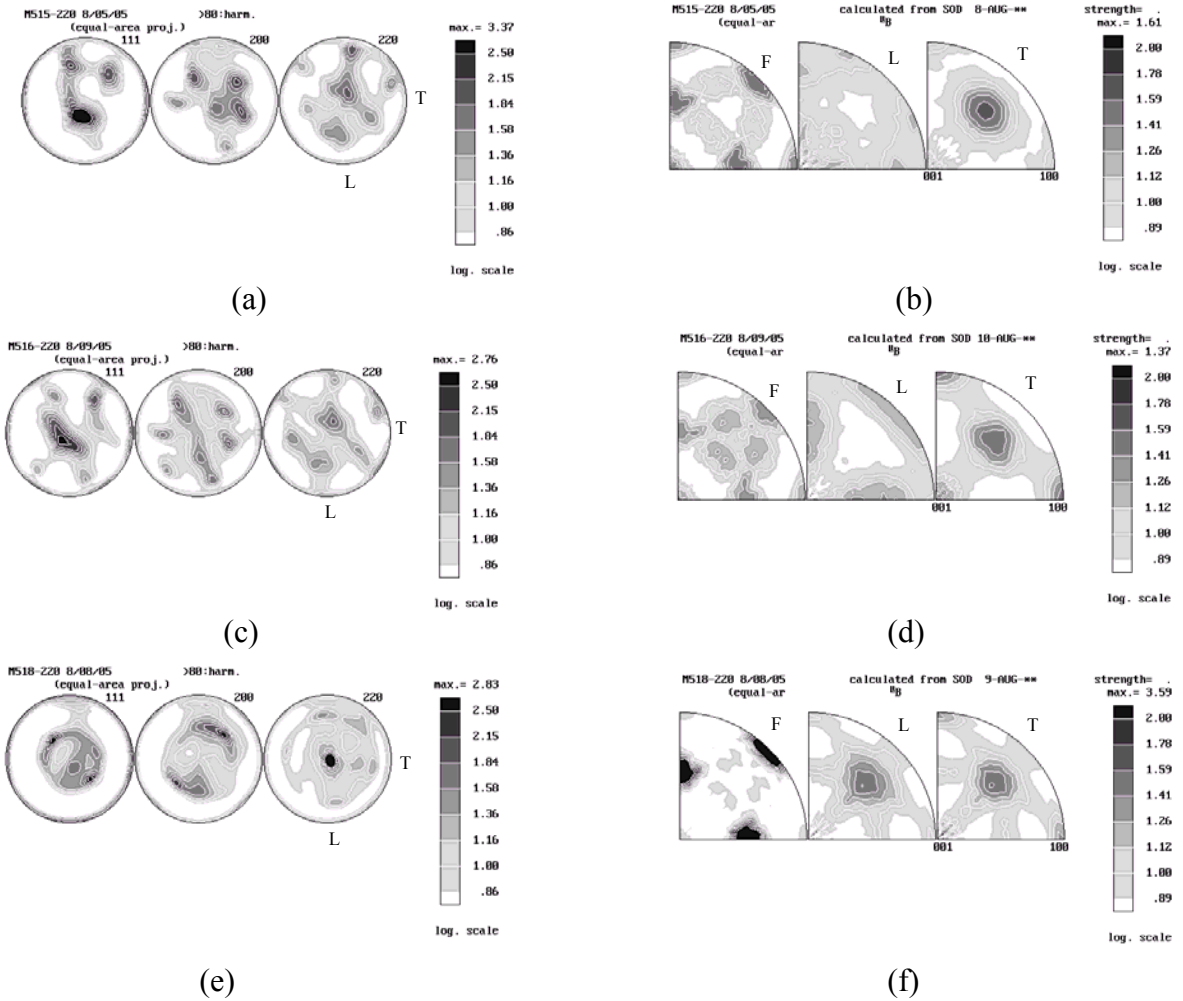

Figure 5.17 Comparison of pole and inverse pole figures of (a,b) of consolidated -325 Mesh Cu powder, (c,d) of a blend containing 75 % of 130 nm and 25% of -325 Mesh Cu powders, and (e,f) a companion sample of the blend case following route 4B.

Texture results assert also the conclusion advanced earlier about the possible deformation mechanisms in consolidated Cu powders. Figures 5.15-17 show that there is no substantial difference in texture between consolidated 130nm and -325 mesh Cu powders and most importantly with ECAE processed wrought Cu. An important role of twinning in the deformation of nanocrystalline material would have been translated by the apparition of new orientation components. A previous study [105] showed for example that for electrodeposited nanocrystalline Cu, a more important presence of twinning was translated by the appearance of new texture components ({151} <110> and {115} <141>). On the other hand, an important contribution of grain boundaries in deformation mechanisms in nanocrystalline materials through grain boundary sliding and Coble Creep will affect the final texture by diffusing the strength of the orientations encountered in ECAE processed bulk Cu and evolve it towards a weaker and more random texture.

The extrusion of a blend of powders of different sizes was motivated by obtaining a bimodal distribution of grain size. The mechanical results were not promising as the maximum strain at fracture was 2.7%. The reason behind this lower value of strain at fracture is the inter-agglomerate debonding which is more pronounced because of the difference in powder size and morphology existing between the spherical microcrystalline powder and the cluster agglomerates of nanocrystalline powder. ECAE process did not succeed in achieving a good consolidation of the blend through a good mixing of these different powders. Texture results corroborate this explanation as a measurement in a companion sample (Figure 5.17.e,f) yielded a different texture. The

disparity in shape and size between the two powders impeded bonding and permitted the rotation of these particles during the extrusion process.

Recently, a Hall-Petch plot (Figure 5.18) summarizing the effect of grain size on the flow stress of Cu was prepared by Conrad *et al* [106]. Our results are included in this plot using average grain sizes determined by X-ray. They fit remarkably well to the Hall-Petch curve. Interestingly, all other consolidation data points are below the H-P line probably because of the porosity. The authors believe that some of the data that shows negative H-P behavior can also be because of residual porosity during consolidation. But this still remains to be proven. One can also argue that since the present microstructure is heavily deformed with grains not being free of dislocations, work hardening as well as grain size hardening should be considered. However, it is likely that the bimodal grain size distribution and residual porosity are the reasons for the lower yield strength levels compared to what would be expected if the strain hardening contribution would also be considered.

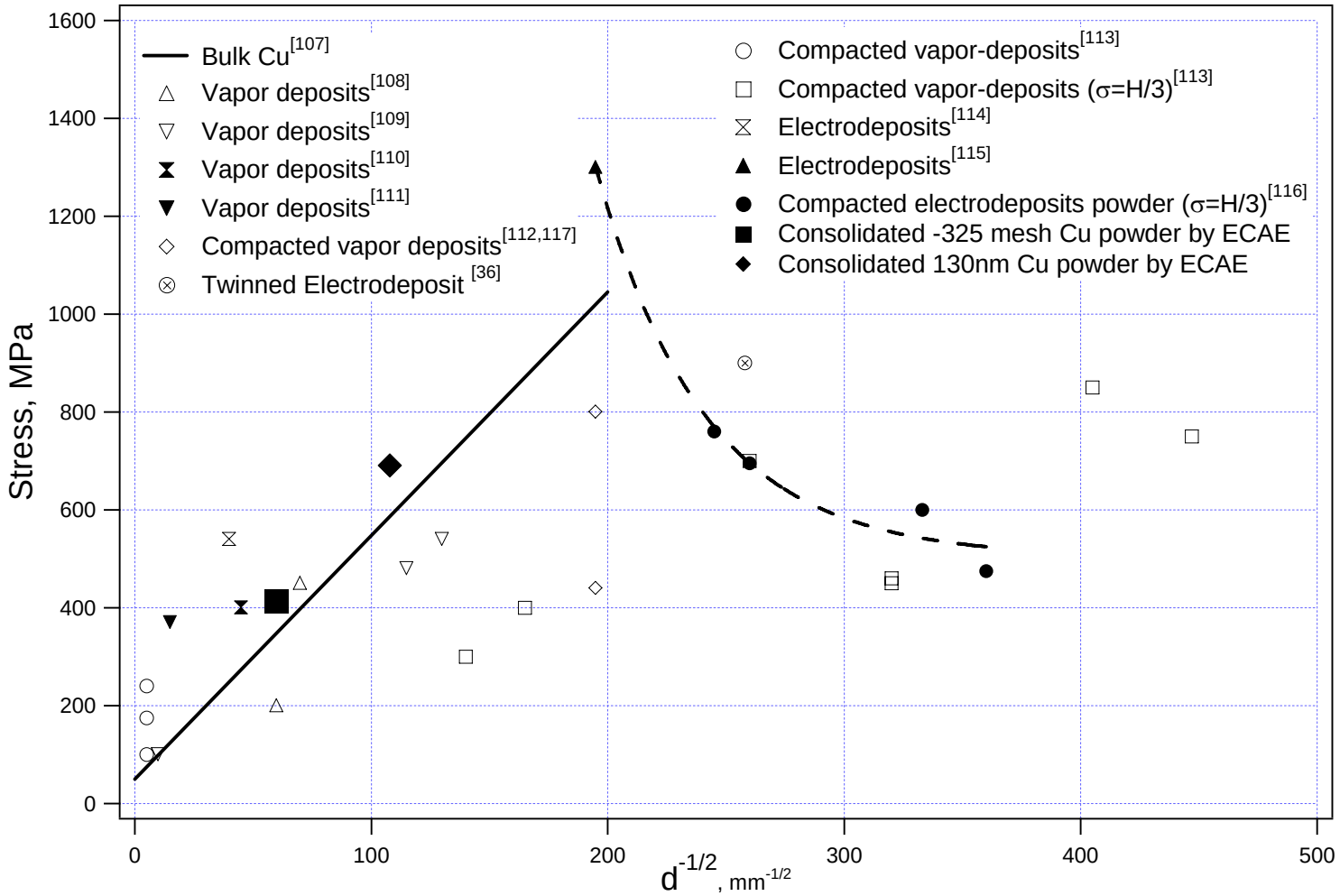

Figure 5.18 A Hall-Petch plot summarizing the effect of grain size on the flow stress of Cu at 300 K [106]. The present results are included.

CHAPTER VI
MAIN CONCLUSIONS

Ultra fine grained Cu was fabricated using severe plastic deformation via the ECAE process. The effect of resulting microstructural features obtained through different strain routes and strain levels on the mechanical anisotropy, tension compression asymmetry and Baushinger effect was assessed. It has been found that texture alone cannot explain the yielding anisotropy exhibited by ECAE processed Cu and that the grain morphology has a significant role in controlling the mechanical behavior through the yield strength. On the other hand, three initial powder sizes (325 mesh, 130 nm, and 100 nm) of Cu were consolidated using ECAE. The mechanical and microstructural evolution of the consolidates were investigated and related to the processing route. Possible deformation mechanisms were discussed and compared with the ones in the extruded wrought Cu. The specific findings are summarized as follows.

1- A simultaneous increase in strength and ductility in extruded bulk Cu is observed for a microstructure with an average grain size of 300-500 nm. The possibility of grain boundary moderated deformation is thought to be inconsistent with this grain size range. Instead, we speculate that the increase of ductility can be attributed to dynamic recovery and local recrystallization forming a bimodal microstructure and to the trapping effect of non-equilibrium grain boundaries.
2- The morphology of grains seems to have a stronger effect on the mechanical response than texture. Routes A and C which have relatively similar textures but different grain morphology yield significantly different mechanical responses.

3- Grain morphology factors compete with grain refinement and cause a drop of yield strength with the number of passes. The effect of grain morphology is more pronounced for the longitudinal direction for which the yield strength drops steadily even between the first passes where the effect of grain refinement is stronger.

4- The anisotropy exhibited by ECAE processed wrought Cu is attributed mainly to the morphology of grains. Indeed, unlike other routes, route A for which the orientation of the billet is kept constant sees a steady evolution of strength values with the number of passes regardless of the test direction.

5- Tension-compression (T/C) asymmetry is observed in UFG Cu. This asymmetry is not always in favor of compression and is affected by grain morphology through the interaction of dislocations with grain boundaries. Regardless of the route, specimens cut in the extrusion direction show higher tensile strength. The (T/C) asymmetry is due to the interaction between mobile dislocations and obstacles they encounter in their path rather to any microstructural evolution. In the case of the ECAE process, the definite grain morphology due to the high angle misorientation between grains is very effective in controlling and affecting dislocation mobility.

6- Dislocation tangles are confirmed to be most detrimental to develop internal stresses assisting the deformation during the reverse straining as route 2C experienced the highest Bauschinger effect for the flow direction.

7- The extrusion parameters for the consolidation of nanoparticles using ECAE have an important effect on the final product. The best can material to consolidate

copper nanoparticles was found to be nickel. A minimum of two passes is necessary for good consolidation. A moderate extrusion rate should not be exceeded to minimize deformation heating.

8- The tensile and compression tests of consolidated 325 mesh and 130 nm Cu powder resulted in a significant increase in yield strength compared to coarse grained annealed Cu. ECAE processed 325 Cu powder via route 2B exhibited an elongation at fracture of about 20 % coupled with an ultimate strength of σ_{UTS} = 470 MPa. Consolidated 130 nm Cu powder yielded an even higher σ_{UTS} (790 MPa for 4B) and a strain fracture of 7.3 % under tension. The lack of tensile ductility is attributed to remnant porosity and premature debonding between pre-consolidated powder agglomerates.

9- The difference in elastic modulus and strength levels between compression and tension responses of the consolidate for a specific route, or between two routes for a given monotonic loading (tension or compression) is attributed to texture.

10- Near-perfect elastoplasticity is observed in consolidated 325 mesh Cu powder. This effect is explained by a combined effect of strain hardening and softening caused by a recovery mechanism such as absorption of dislocations by grain boundaries.

11- The deformation in NC Cu fabricated by consolidation of nanocrystalline powder seems to be controlled essentially by dislocations. Some fine grains on the order of 50 nm deform by twinning when the material is subjected to a compressive deformation, but this mechanism is not very significant as it does not affect the final texture of the material.

12- Blending powders with the objective of creating a bimodal distribution of grain sizes does not seem to improve the strain at fracture. For this case, inter-agglomerate debonding appears to be more pronounced.

13- ECAE was shown to be a viable method to fabricate relatively large nanocrystalline consolidates with excellent mechanical properties. Further improvements are expected to result from appropriate processing schedules that lead to a microstructure where large grains, which can accommodate plastic strain, are embedded in a fine structure giving enhanced strength and ductility to the material.

CHAPTER VII
SUGGESTIONS FOR FUTURE WORK

1- ECAE has shown to be a viable process for consolidation of nanocrystralline Cu powders. The consolidation should be extended to other potential materials such as stainless steel and titanium powders.

2- More investigation should be undertaken with the objective of increasing the ductility of the consolidates. The size of Cu agglomerates should be reduced prior to filling in order to reduce the impact of inter agglomerate debonding. Ultrasonic vibration can be used to disintegrate the agglomerate. A post mechanical processing after ECAE such us conventional extrusion can be used to reduce further any potential debonding site. The ECAE processed can should be milled down to a cylindrical shape having the maximum diameter possible, in order to benefit from the hydrostatic pressure from the can during the conventional extrusion. The extrusion should be performed following a schedule of small successive steps.

3- The idea of blending powders should be studied more. I suggest using a blend with lower volume percentage of microcrystalline powder (5 to 10%). TEM micrographs showed the existence of large grains in consolidated nanocrystalline powder devoid of dislocations, which mean that the material can still undergo plastic deformation with the existing large grains. Thus, it is not necessary to add a high percentage of microcrystalline powder. The mixing of the two powders is important and should be performed carefully.

4- Once the optimum conditions for a good consolidation are determined (hopefully 15 to 20% strain at fracture), consolidation of 50 nm Cu powder should be attempted. This is important to determine the limits of ECAE process in consolidation of nanocrystalline powders. Also it will provide an additional data for the Hall-Petch relationship in order to check the validity of this assumption of softening beyond a certain grain size.

5- The response of the consolidates to fatigue cycling should be performed and compared to wrought Cu.

6- The results obtained in the anisotropy study of ECAE processed wrought copper can be used to determine the effect of strain level and strain path in ECAE process on the plasticity response. An additional specimen having its flat surface parallel to the longitudinal plane and oriented 45^{o} with respect to extrusion and flow directions should be tested in tension. These results, along with the existing tension results for yield stresses along the extrusion and flow directions can be used to plot a yield surface for each ECAE schedule using the Hill criterion. Such study will permit to determine the nature of hardening (kinematic or isotropic) associated with each ECAE schedule.

7- A more systematic Bauschinger study should be carried out where different prestrains (1%, 2%, and 5%) in both compression and tension should be investigated. The obtained results along with the existing information would give a better insight into the fatigue behavior and how it is affected by the anisotropy in ECAE processed wrought copper.

REFERENCES

[1] Segal VM. Mat Sci Eng 1995;A197:157.

[2] Ferrasse S, Segal VM, Hartwig KT, Goforth RE. Metall Mater Trans1997;28A:1047.

[3] Valiev RZ, Islamgaliev RK, Alexandrov IV. Prog Mater Sci 2000;45:103.

[4] Matsuki K, Aida T, Takeuchi T, Kusui TJ, Yokoe K. Acta Mater 2000;48:2625.

[5] Hansen N. Met Trans 2001;A32:2917.

[6] Jensen DJ, Hansen N. In: Proceeding. ICSMA 9, Brandon DG, Chaim R, Rosen A editors. Freund, London; 1991. p.179.

[7] Hansen N, Jensen DJ. Phil Trans R Soc London A 1999;357:1447.

[8] Wert JA, Liu Q, Hansen N. Acta Mater 1997;45:2565.

[9] Liu Q, Maurice C, Driver J, Hansen N. Metall Mater Trans 1998;29A:2333.

[10] Vinogradov A, Ishida T, Kitagawa K, Kopylov VI. Acta Mater 2005;53:2181.

[11] Gleiter H: Deformation of Polycrystals, Mechanisms and Microstructures, editors. N. Hansen et al., Roskile, Denmark, Riso National Laboratory, 1981, 15.

[12] McFadden SX, Mishra RS, Valiev RZ, Zhilyaev AP, and Mukherjee AK. Nature, 1999;398:684.

[13] Alexandrov IV, Zhu YT, Lowe TC, Islamgaliev RK, and Valiev RZ. Nanostr. Mater 1998;10:45.

[14] Valiev RZ, Alexandrov IV, Zhu YT, and Lowe TC. J. Mater. Res 2002;17:5.

[15] Höppel HW, Valiev RZ, Z. Metallkd 2002 ;93:641.

[16] Valiev RZ, Kozlov EV, Ivanov YF, Lian J, Nazarov AA, Baudelet B. Acta Metall Mater 1994;42:2467.

[17] Valiev RZ, Islamgaliev RK, Alexandrov IV. Prog. Mater. Sci 2000;45:103.

[18] Alexandrov IV, Zhu YT, Lowe TC, Islamgaliev RK, Valiev RZ. Metall. Mater. Trans 1998;29A:2253.

[19] Horita Z, Fujinami T, Langdon TG. Mater. Sci. Eng 2001;A318:34.

[20] Matsuki K, Aida T, Takeuchi T, Kusui J. Mat. Sci. Forum 2000;331:1215.

[21] Raab GI, Krasilnikov NA, Thiele E, Klemm R. Ultrafine Grained Materials II, editors. Zhu YT et al., TMS Annual Meeting 2002:245.

[22] Champion Y, Guérin-Mailly S, Bonnentien JL, Langlois P. Scripta Mater 2001;44:1609.

[23] Champion Y, Langlois C, Guérin-Mailly S, Langlois P, Bonnentien JL, Hÿtch MJ. Science 2003;300:310.

[24] Surynarayanan Iyer R, Frey CA, Sastry SM, Waller BE, Buhro WE. Mater. Sci. Eng 1999;A264:210.

[25] Sanders PG, Eastman JA, Weertman JR. Acta Mater 1997;45:4019.

[26] Legros M, Elliott BR, Rittner MN, Weertman JR and Hemker KJ. Phil. Mag 2000;A80:1017.

[27] Tellkamp VL, Melmed A, Lavernia EJ. Metall. Mater. Trans 2001;32:2335.

[28] Rawers J, Slavens G, Govier D, Dogan C, Doan R. Metall. Mater. Trans 1998;29A:2261.

[29] Inoue A. Prog. Mater. Sci 1999;43:365.

[30] Ebrahimi F, Zhai Q, and Kong D, Scripta Mater 1998;39:315.

[31] Kumar KS, Suresh S, Chisholm MF, Horton JA, Wang P. Acta Mater 2003;51:387.

[32] Jia D, Ramesh KT, Ma E, Lu L, Lu K. Scripta Mater 2001;45:613.

[33] Andrievskii RA, Glezer AM. Phys. Met. Metall 2000;89:83.

[34] Youssef KM, Scattergood RO, Murty KL, Koch CC. Applied Physics Letters 2004;85:929.

[35] Youssef KM, Scattergood RO, Murty KL, Horton JA, Koch CC. Applied Physics Letters 2005;87:091904.

[36] Shen YF, Lu L, Lu QH, Jin ZH, Lu K. Scripta Mater 2005;52:989.

[37] Zapata H: Application of Equal Channel Angular Extrusion to Consolidate Aluminum 6061 Powder, M.S. Thesis, Texas A&M University, 1998.

[38] Parasiris A, Hartwig KT, Srinivasan MN. Scripta Mater 2000;42:875.

[39] Robertson J, Im JT, Karaman I, Hartwig KT, Anderson IE. J. of Non-Crystalline Solids 2003;317:144.

[40] Parasiris A, Hartwig KT. Int. J. Refract. Metals. Hard. Mater 2000;18:23.

[41] Furukawa M, Iwahashi Y, Horita Z, Nemoto M, Langdon TG. Mater. Sci. Eng. A 1998;A257:328.

[42] Harris C, Prangnell PB and Duan X. Proceedings of the 6th International Conference on Aluminum Alloys, Japan 1998;ICAA-6: 583.

[43] Humphreys FJ, Prangnell PB, Bowen JR, Gholinia A, Harris C. Phil. Trans. R. Soc. Lond 1999;A **357:**1663.

[44] Komura S, Horita Z, and Nemoto M. J. Mater. Res 1999;14:4044.

[45] Agnew SR, Kocks UF, Hartwig KT and Weertman JR. Proceedings of the 19th Risø International Symposium of Material Science, Roskilde Denmark 1998:201.

[46] Haouaoui M, Hartwig KT, Payzant EA. Acta Mater 2005;53:801.

[47] Gibbs MA, Hartwig KT, Cornwell LR, Goforth RE, Payzant EA. Scripta Mater 1998;39:1699.

[48] Barrett CS, and Levenson LH. A.I.M.E. Trans 1941;145:283.

[49] Barrett CS, and Massalski TB, Structure of Metals. Oxford, UK, Pergamon Press, 1980.

[50] Gibbs MA: Texture development of BCC metals processed by equal channel angular extrusion, Ph.D dissertation, Texas A&M University, 2000.

[51] Langdon TG, Furukawa M, Nemoto M, Horita Z. JOM 2000;52:30.

[52] Stolyarov VV, Zhu YT, Alexandrov IV, Lowe, Valiev RZ. Mat Sci Eng 2001; A299:59.

[53] Haouaoui M, Karaman I, Maier H, Hartwig KT. Met Trans 2004;A35:2935.

[54] Carsley JE, Fisher A, Milligan WW, Aifantis EC. Metall Mater Trans A 1998;29A:2261.

[55] Hayes RW, Rodriguez R, Lavernia EJ. Acta Mater 2001;49:4055.

[56] Tabachnikova ED, Bengus VZ, Stolyarov VV, Raab GI, Valiev RZ, CsachK et al. Mater Sci Eng 2001;A309-310:524.

[57] Cheng S, Spencer JA, Milligan WW. Acta Mater 2003;51:4505.

[58] Hall EO. Proc. Phys. Soc 1951;B64:747.

[59] Petch NJ. J. Iron Steel 1953;174:25.

[60] Kumar KS, Van Swygenhoven H, Suresh S. Acta Mater 2003;51:5743.

[61] Wang Y, Chen M, Zhou F, Ma E. Nature 2002;419:912.

[62] Zhang X, Wang H, Scattergood RO, Narayan J, Koch CC, Sergueeva AV, Mukherjee AK. Acta Mater 2002;50:4823.

[63] Wang YM, Ma E, and Chen MW. App. Phys. Lett 2002;80:2395.

[64] Youngdahl CJ, Sanders PG, Eastman JA, Weertman JR. Scripta Mater 1997;37:809.

[65] Agnew SR, Elliott BR, Youngdahl CJ, Hemker KJ, Weertman JR. Mater. Sci. Eng 2000;A285:391.

[66] Youngdahl CJ, Weertman JR, Hugo RC, Kung HH. Scripta Mater 2001;44:1475.

[67] Swygenhoven HV, Derlet PM, Hasnaoui A. Phys. Rev 2002;B66:024101-8.

[68] Swygenhoven HV, Derlet PM. Phys. Rev 2001;B64:224105.

[69] Gleiter H. Prog. Mater. Sci 1989;33:223.

[70] Masumura RA, Hazzledine PM, Pande CS. Acta Mater 1998;46:4527.

[71] Wang YM, Wang K, Pan D, Lu K, Hemker KJ, Ma E. Scripta Mater 2003;48:1581.

[72] Segal V, Goforth RE, Hartwig KT, Texas A&M University, U.S. Patent No. 5,400,633 (1995).

[73] Segal V, U.S. Patent No. 5,513,512 (1996).

[74] Segal V and Segal L, U.S. Patent No. 5,600,989 (1996).

[75] Lowe TC, Valiev RZ. JOM 2000;52:27.

[76] Liepert S: The influence of equal channel angular extrusion on texture evolutionin pure tantalum, M.S. Thesis, Texas A&M University, 1999.

[77] Barber RE, Dudo T, Yasskin PB, Hartwig KT. Scripta Mater 2004;51:373.

[78] Kocks UF, Kallend JS, Wenk HR, Rollet AD, Wright SI, POPLA, Los Alamos National Laboratory, NM (1994).

[79] Smallman RE, and Westmacott KH. Phil. Mag 1957;2:669.

[80] Warren BE: X-ray Diffraction, New York, NY, Dover, Chap. 13.

[81] ASTM Standard C20-92, ASTM, Philadelphia, PA,1996;5.01:5.

[82] Dieter GE: Mechanical Metallurgy, New York, NY, McGraw Hill, 2nd edition, 1976, Chap 3:75.

[83] Drucker D. Metall Trans 1973;4:667.

[84] Karaman I, Sehitoglu H, Chumlyakov YI, Maier HJ, Kireeva IV. Met Trans 2001;32A:695.

[85] Pardoen T, Brechet Y. Phil Mag 2004;84:269.

[86] Izotov VI, Rusanenko VV, Kopylov VI, Pozdnyakov VA, Edneral AF, Kozlov AG. Phys Met Metallogr 1996;82:289.

[87] Furukawa M, Horita Z, Langdon TG. J Mater Sci 2005;40:909.

[88] Iwahashi Y, Horita Z, Nemoto M, Langdon TG. Acta Mater 1997;45:4733.

[89] Dalla Torre F, Lapovok R, Sandlin J, Thomson PF, Davies CHJ, Pereloma EV. Acta Mater 2004;52:4819.

[90] Hugues DA, Hansen N, Metall Trans 1993;24:2021.

[91] Hugues DA, Hansen N, Acta Metall 2000;48:2985.

[92] Gholinia A, Prangnell PB, Markushev MV. Acta Mater 2000;48:1115.

[93] Beyerlein IJ, Lebensohn RA, Tome CN. Mat Sci Eng 2003;A345:122.

[94] Ferrasse S, Segal VM, Kalidindi SR, Alford F. Mat Sci Eng 2004;A368:28.

[95] Mahesh S, Tome CN, McCabe RJ, Kaschner GC, Beyerlein IJ, Misra A. Met Trans 2004;35A:3763.

[96] Peeters B, Seefeldt M, Teodosiu C, Kalidindi SR, Van Houtte P, Aernoudt E. Acta Mater. 2001,49:1607.

[97] Peeters B, Bacroix B, Teodosiu C, Van Houtte P, Aernoudt E. Acta Mater. 2001,49:1621.

[98] Kocks UF, Hasegawa T, Scattergood RO. Scrip Metall. 1980,14:449.

[99] Pedersen OB, Brown LM, Stobbs WM. Acta Metall 1981;29:1843.

[100] T.S. Srivatsan, B.G. Ravi, A.S. Naruka, M. Petraroli, R. Kalyanaraman, and T.S. Sudarshan. Materials and Design 2002;23:291.

[101] Hosford WF: The Mechanics of Crystals and Textured Polycrystals, New York, NY, Oxford University Press, Oxford, 1993, Chapter 1, p 19.

[102] Kallend JS, Kocks UF, Rollett AD, Wenk RH. Mater. Sci. Eng 1991;A132:1.

[103] Valiev RZ. Mater. Sci. Eng 1997;234:59.

[104] Carsley JE, Milligan WW, Zhu XH, Aifantis EC. Scripta Mater 1997;36:727-32.

[105] Lee HJ, Kim DI, Ahn JH, Lee DN. Thin Solid Films 2005;474:250.

[106] Conrad H. Mater. Sci. Eng 2003; A341:216.

[107] Hansen N, Ralph B. Acta Metall 1982;30:411.

[108] Henning C, Boswell F, Corbett J. Acta Metall 1975;23:177.

[109] Merz M, Dahlgren SJ. J. Appl. Phys 1975;46:3235.

[110] Embury JD, Lahaie DJ. In Natasi M *et al.* Mechanical Properties and Deformation Behavior of Materials Having Ultrafine Microstructure, Dordrecht, The Netherlands, Kluwer Academic Publisher, 1993:287.

[111] Huang H, Spaepen F. Acta Mater 2000;48:3261.

[112] Sanders PG, Eastman JA, Weertman JR. In Suryanarayana C, Singh J, Froes FH. Processing and Properties of Nanocrystalline Materials, Warrendale, PA, TMS, 1996: 379.

[113] Nieman GW, Weertman JR, Siegel RW. J. Mater. Res 1991;6:1012.

[114] Conrad H, Di Y. Journal of Electronic Materials 2002;31:304.

[115] Cai B, Kong Q, Lu L, Lu K. Scripta Mater 1999;41:755.

[116] Chokshi H, Rosen A, Karch J, Gleiter H. Scripta Metal 1989;23:1679.

[117] Sanders PG, Youngdahl CJ, Weertman JR. Mater. Sci. Eng 1997;A234-236:77.

APPENDIX

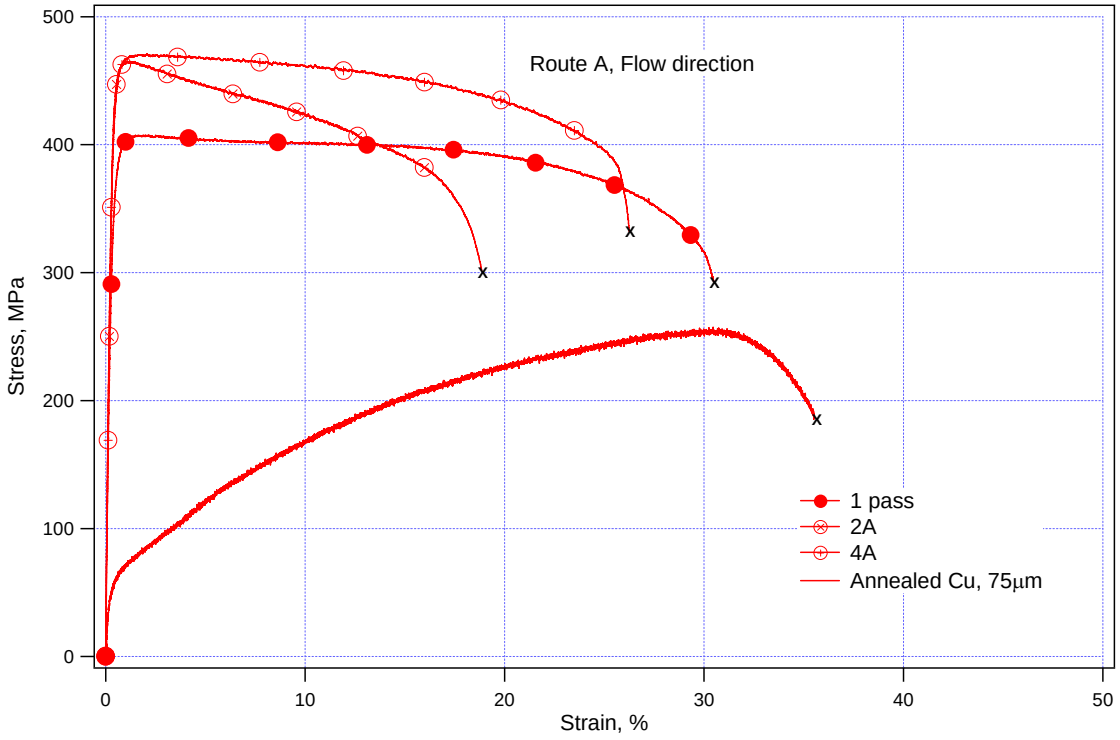

(a)

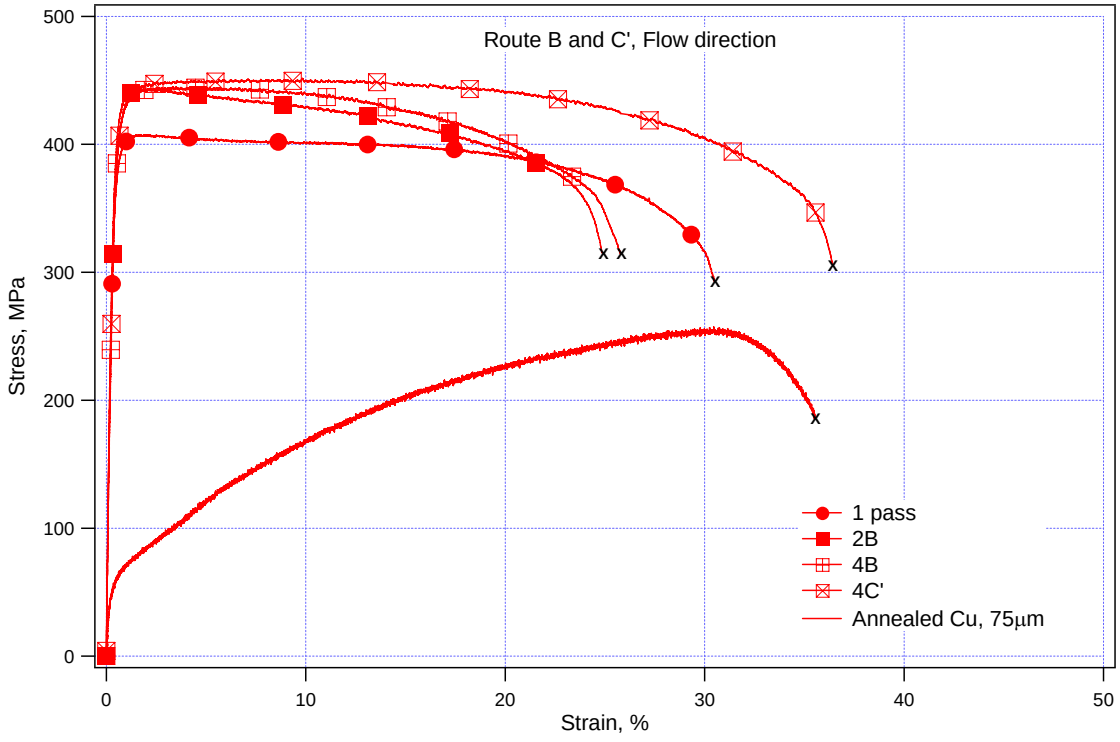

(b)

Figure A.1 Mechanical response in tension of ECAE processed bulk Cu specimens cut along the flow direction for, (a): Route A, (b): Routes B and C', (c): Routes C and E.

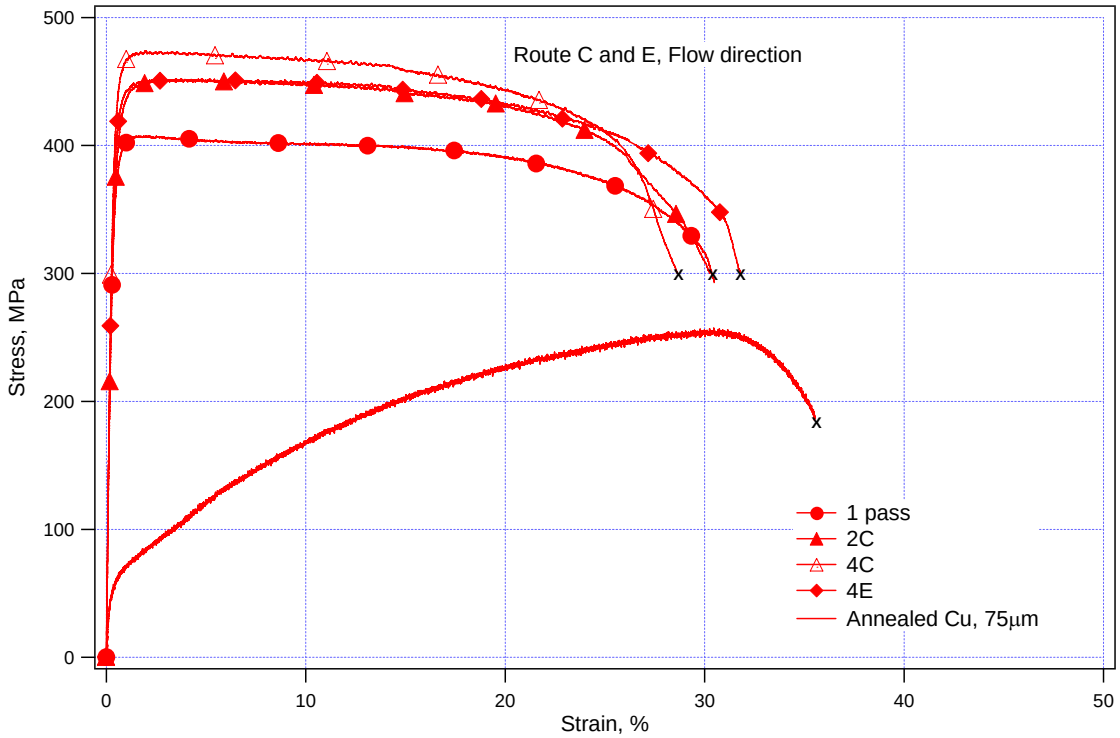

(c)

Figure A.1 Continued.

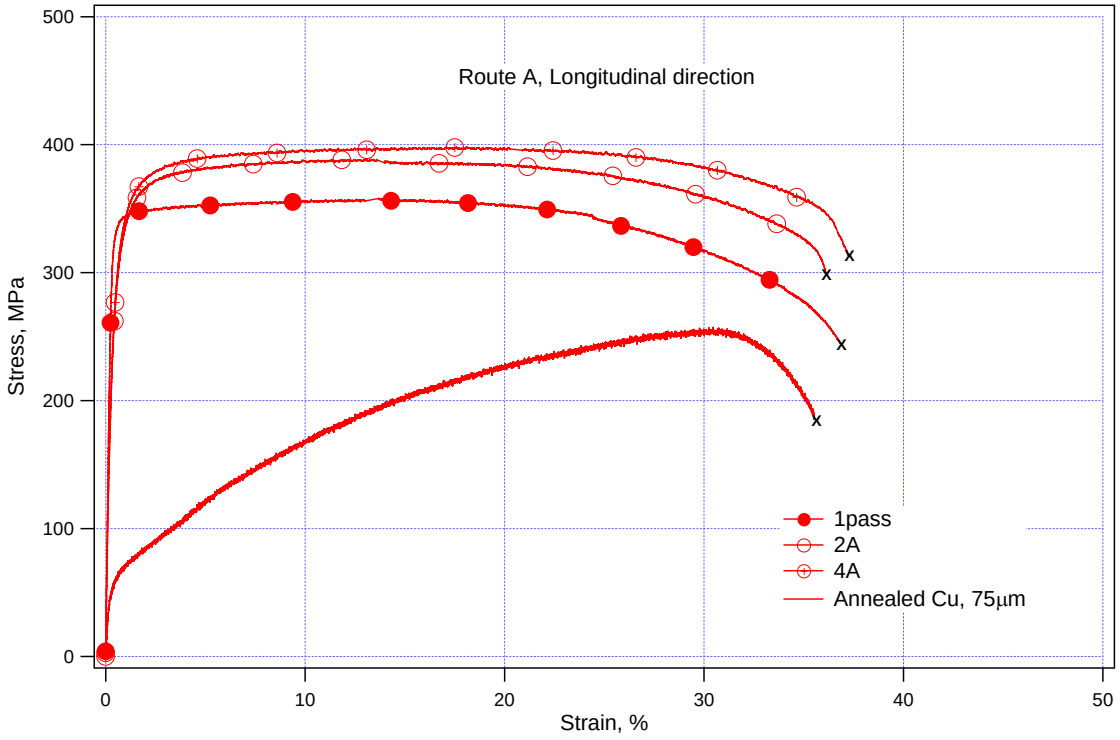

(a)

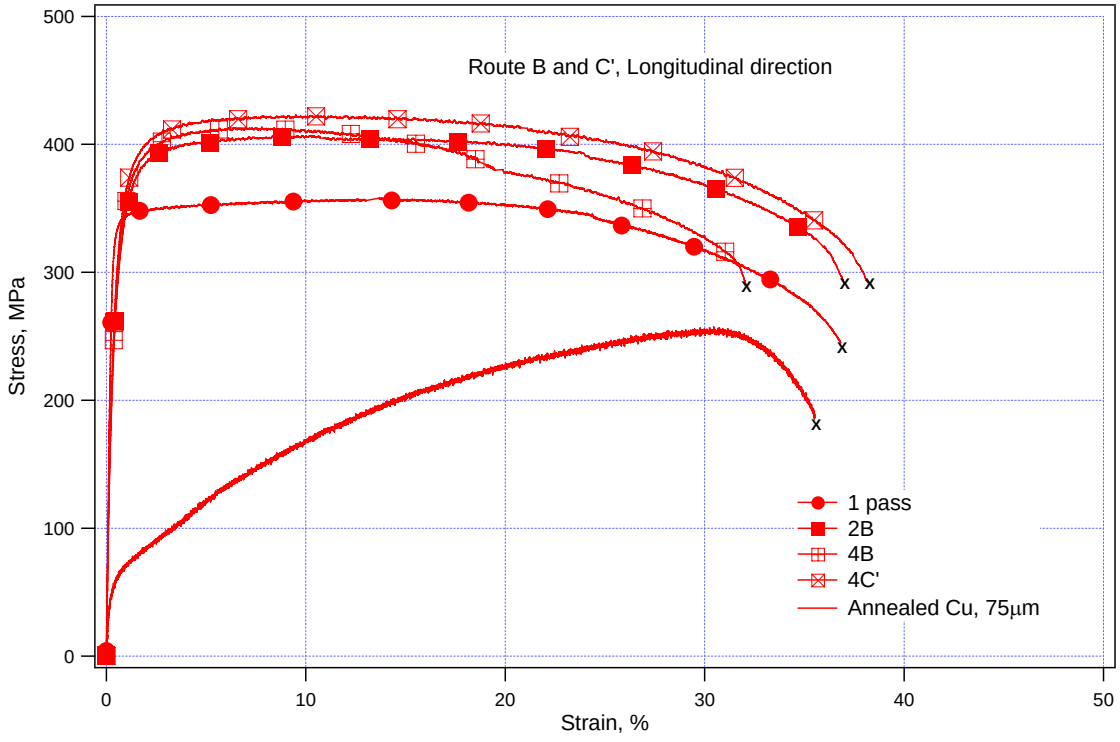

(b)

Figure A.2 Mechanical response in tension of ECAE processed bulk Cu specimens cut along the longitudinal direction for, (a): Route A, (b): Routes B and C', (c): Routes C and E.

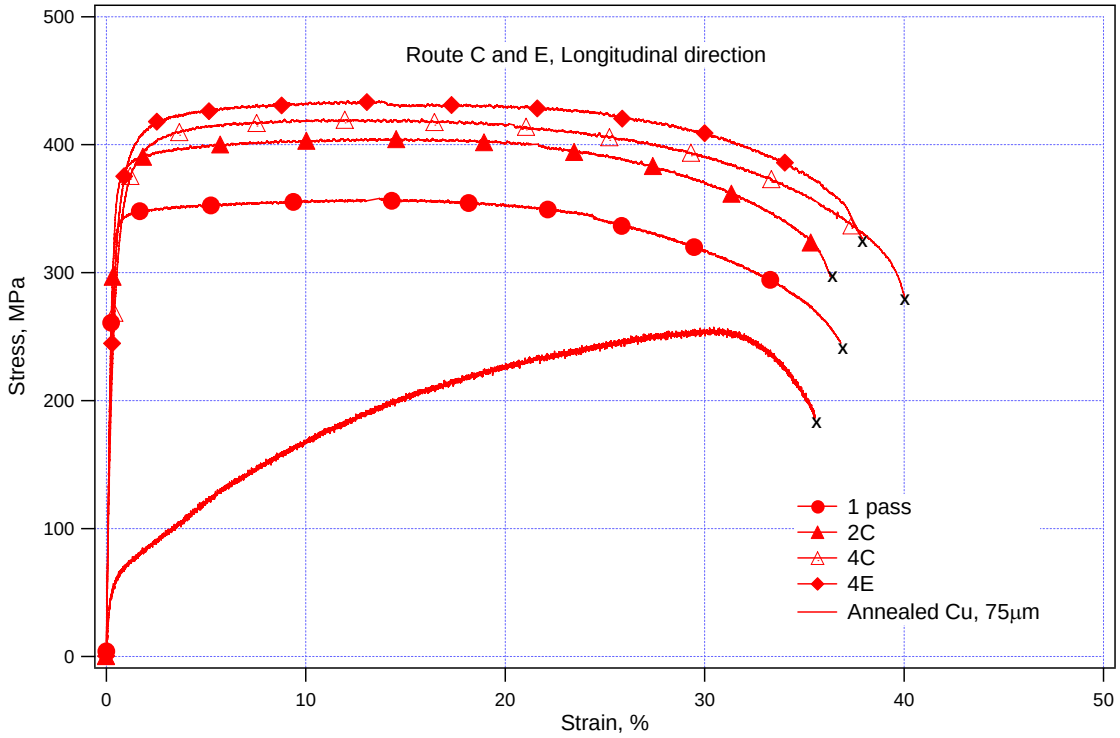

(c)

Figure A.2 Continued.

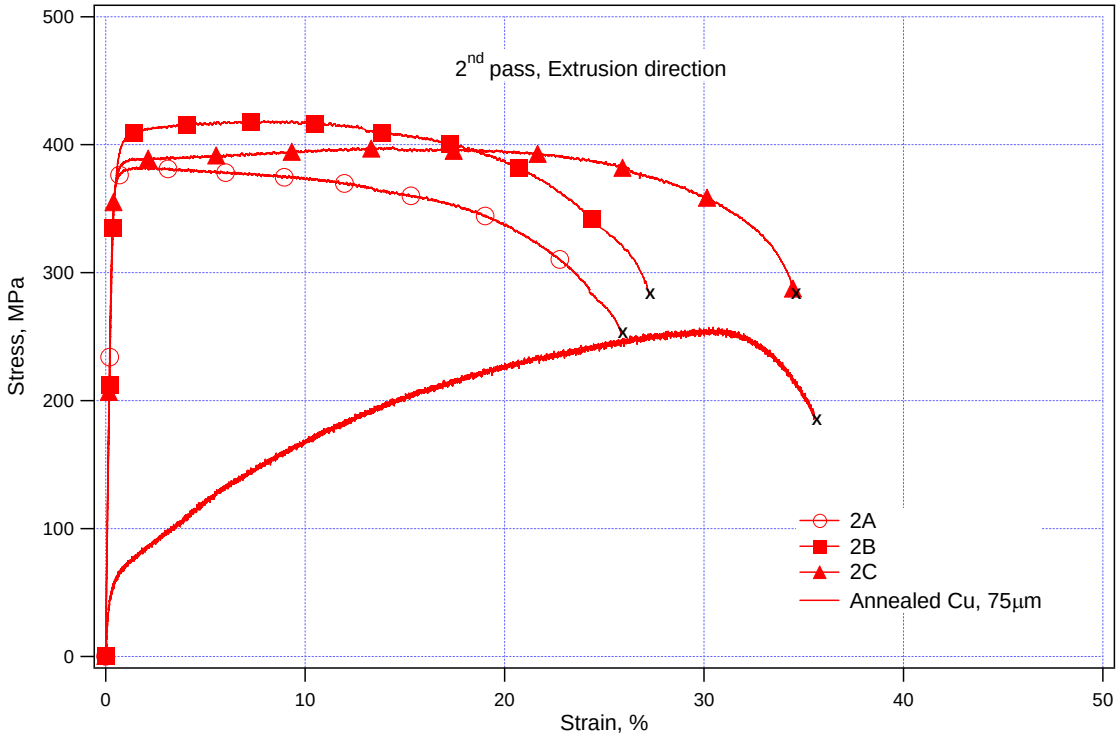

(a)

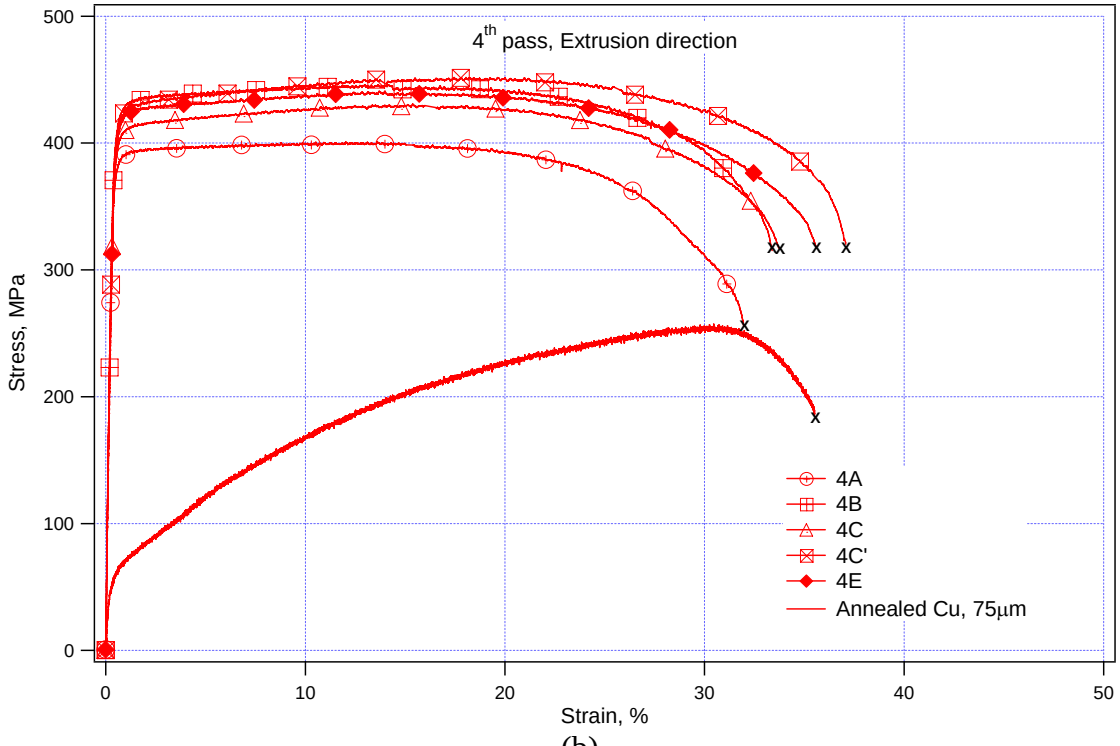

(b)

Figure A.3 Mechanical response in tension of ECAE processed bulk Cu specimens cut along the extrusion direction for, (a): 2nd pass, (b): 4th pass, (c): 8th pass.

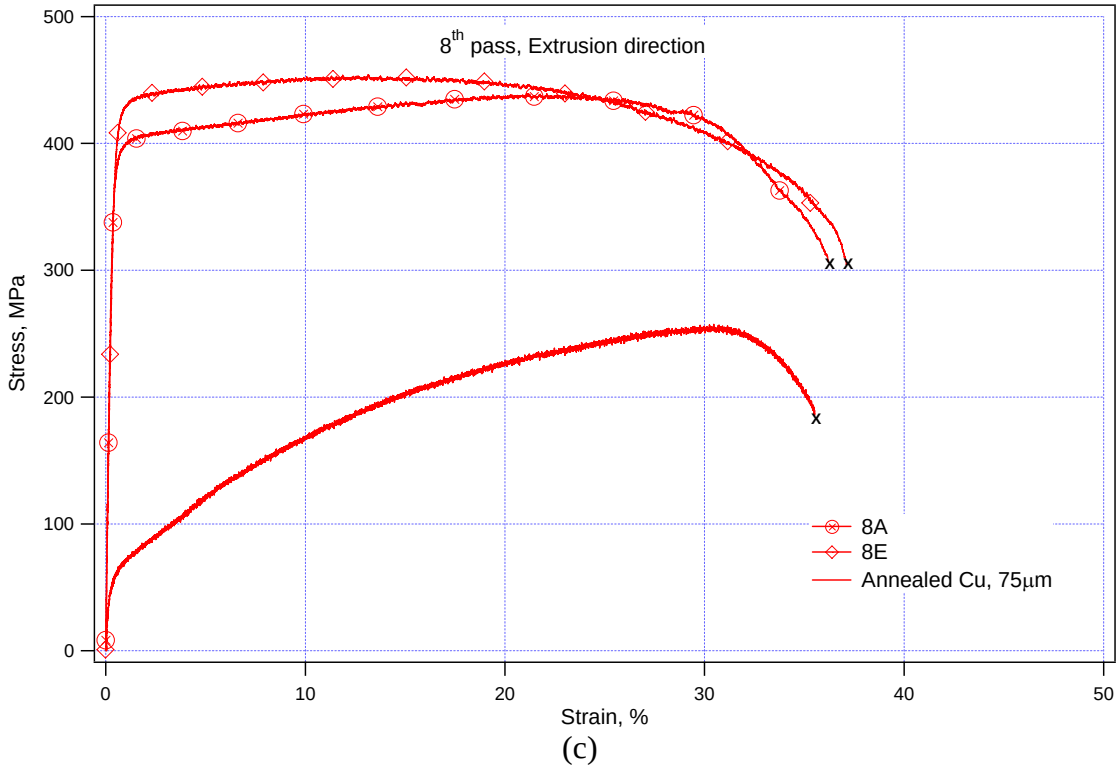

(c)

Figure A.3 Continued.

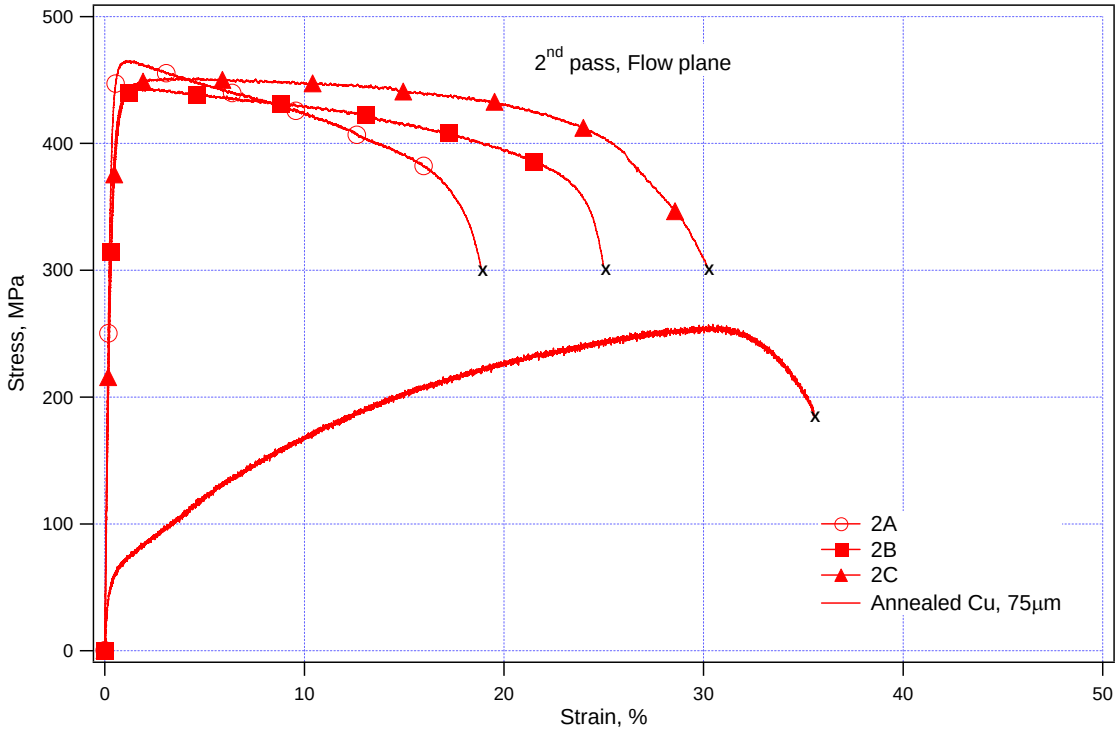

(a)

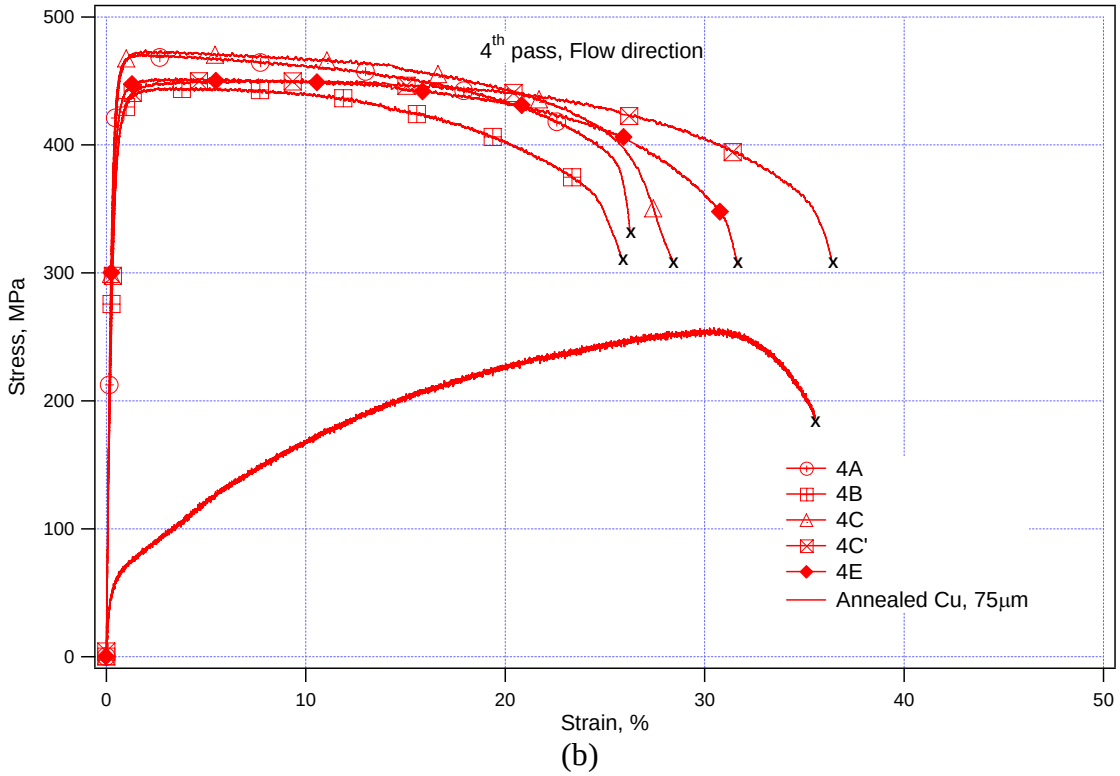

(b)

Figure A.4 Mechanical response in tension of ECAE processed bulk Cu specimens cut along the flow direction for, (a): 2nd pass, (b): 4th pass.

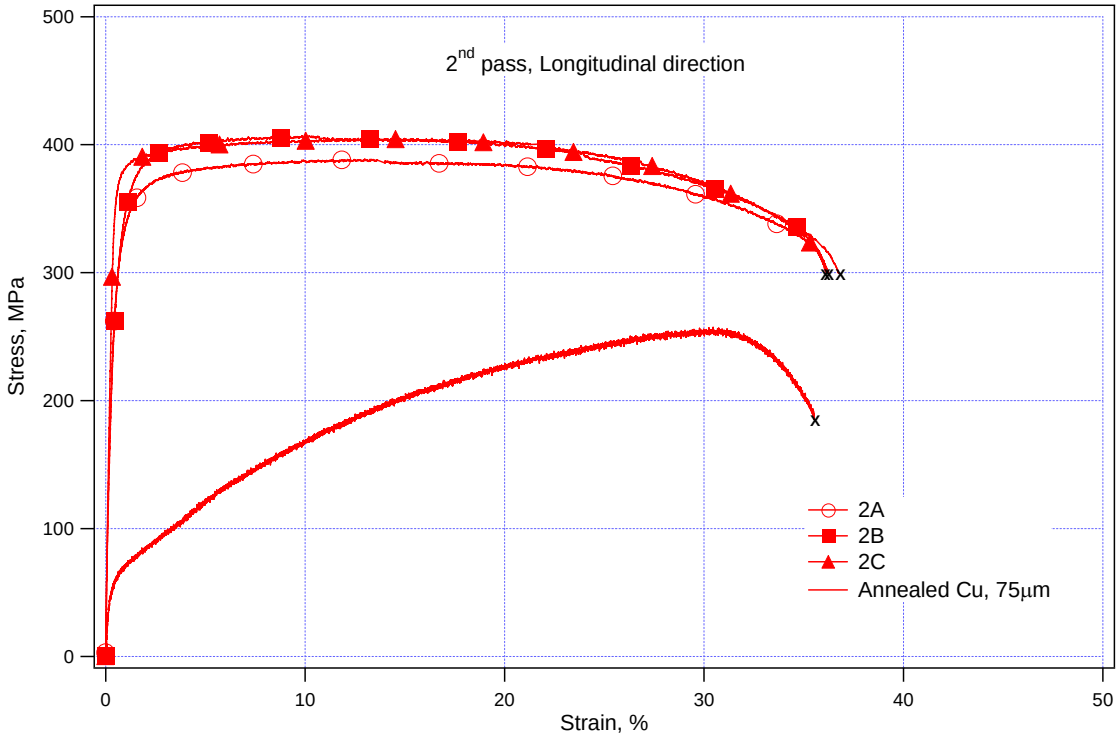

(a)

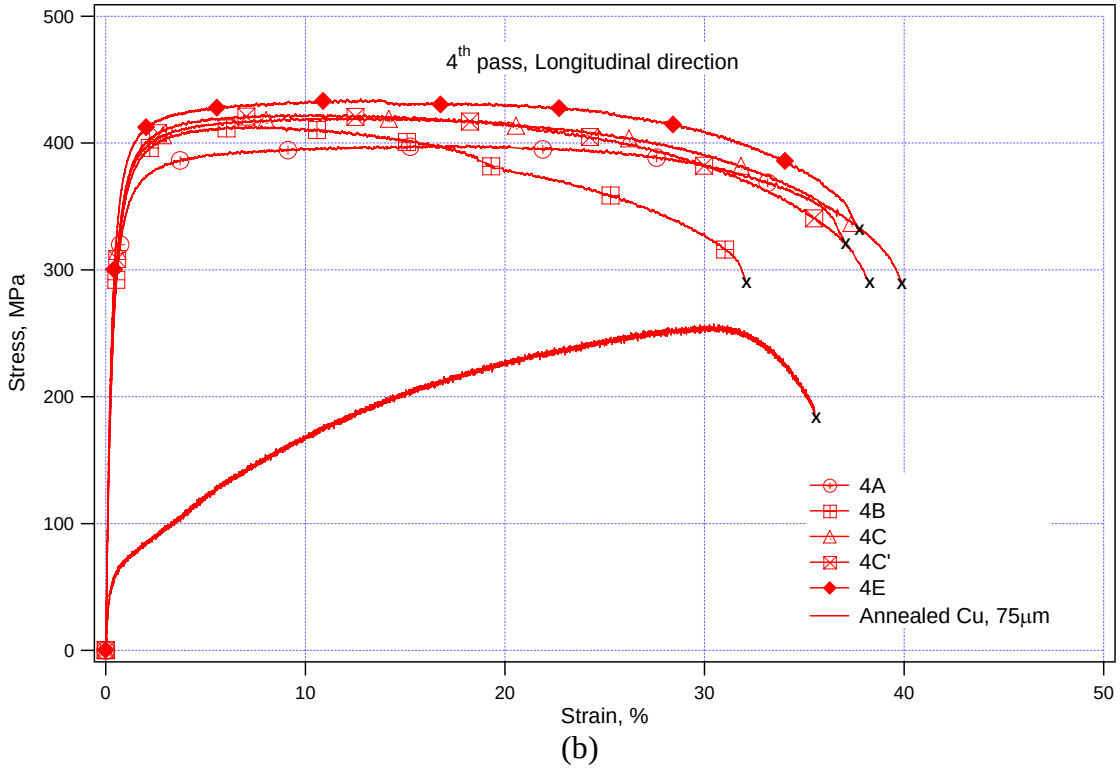

(b)

Figure A.5 Mechanical response in tension of ECAE processed bulk Cu specimens cut along the longitudinal direction for, (a): 2nd pass, (b): 4th pass.

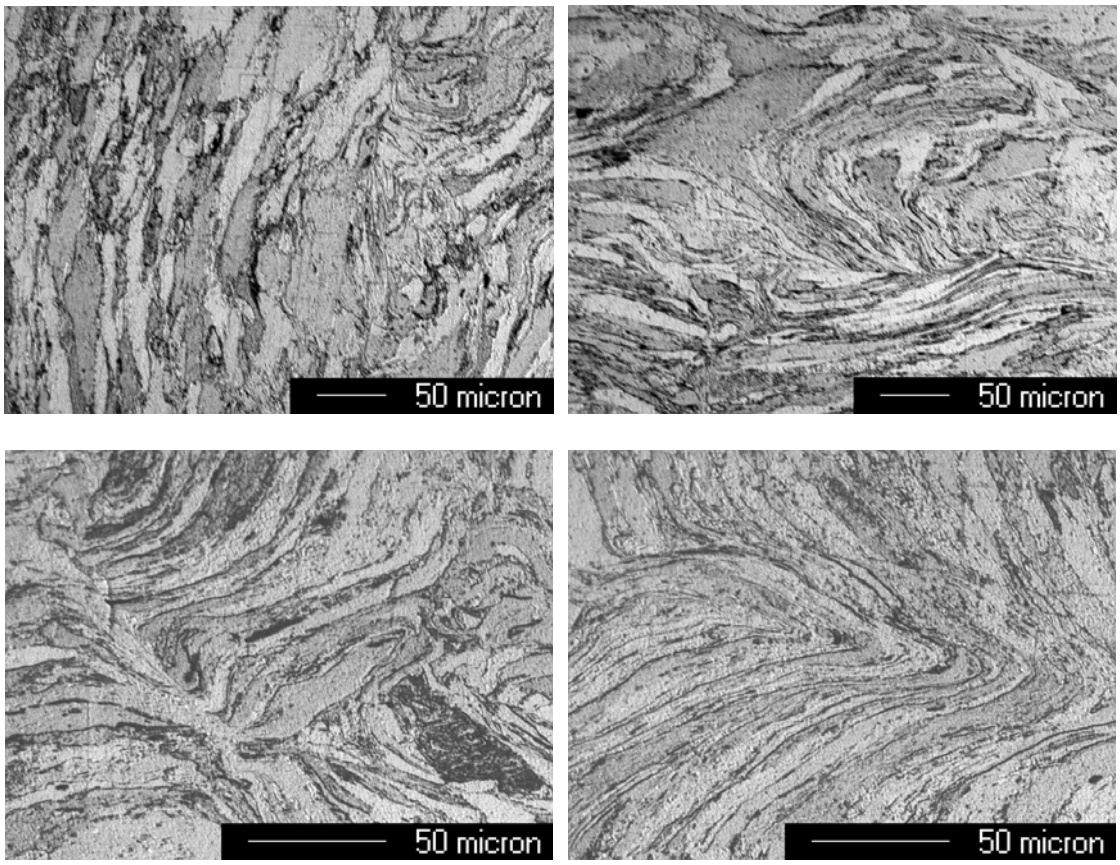

Figure A.6 Optical micrographs illustrating the non uniformity of flow lines formed by the elongated agglomerates in some areas of consolidated nanocrystalline Cu powders.

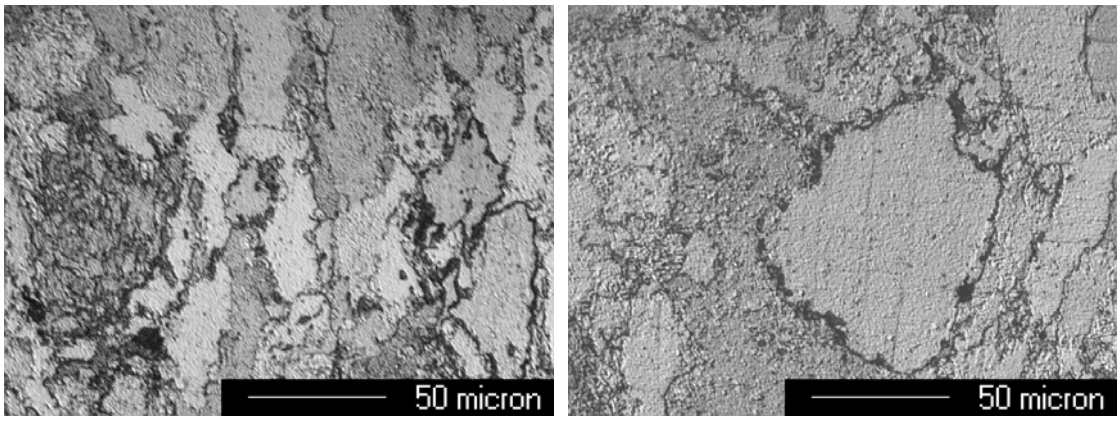

Figure A.7 Presence of cavities responsible of debonding between agglomerates in consolidated nanocrystalline Cu powders.

VITA

Mohammed Haouaoui was born on May 11, 1974 in Tangier, Morocco to Farida Rachidi and Ahmed Haouaoui. He is the eldest in a family of two brothers and three sisters. He is married to Chehrazade Aboukinane and a father of two children Adam and Layan. He attended elementary and high school in Tangier. After two years of intensive mathematics and physics at Lycee Monge, Chambéry, France, he pursued a degree of engineering in Ecole des Mines de Saint Etienne, Saint Etienne, France. He obtained a degree of engineering in Material Science from Ecole des Mines in 1997. During his studies in this school, he attended to different internships in Merlin Gerin (Grenoble, France), Griset (Villers St Paul, France), and CEZUS (Ugine, France). In the summer of 1997, he enrolled at Texas A&M University, College Station, TX, as an exchange student under the supervision of Dr Hartwig. In order to pursue a Master of Science degree, he enrolled at Texas A&M University, College Station, TX, in the fall of 1999. He earned his Master of Science degree in mechanical engineering in December 2001, specializing in the area of material science. Mohammed pursued a Ph.D degree in the same university under the supervision of Dr Karaman. During his graduate career, he continuously held a research assistantship. Mohammed had also the opportunity to serve as teaching assistant in material science lab class (MEEN 360) and mechanical behavior of materials (MEEN 467). During his graduate study at Texas A&M University, he has been an author of 3 published, 2 submitted journal papers and 7 conference presentations. He currently resides at 13021 Legendary Dr, Apt #1618 Austin, TX 78727.